

University of New Hampshire

## University of New Hampshire Scholars' Repository

---

Doctoral Dissertations

Student Scholarship

---

Spring 2018

# STRUCTURE AND MECHANICAL AND TRIBOLOGICAL PROPERTIES OF MAGNETRON SPUTTER DEPOSITION OF STAINLES-STEEL NITRIDE AND CARBIDE THIN FILMS WITH TRANSITION METAL ADDITIVES

Faisal Alresheedi

*University of New Hampshire, Durham*

Follow this and additional works at: <https://scholars.unh.edu/dissertation>

---

### Recommended Citation

Alresheedi, Faisal, "STRUCTURE AND MECHANICAL AND TRIBOLOGICAL PROPERTIES OF MAGNETRON SPUTTER DEPOSITION OF STAINLES-STEEL NITRIDE AND CARBIDE THIN FILMS WITH TRANSITION METAL ADDITIVES" (2018). *Doctoral Dissertations*. 2393.

<https://scholars.unh.edu/dissertation/2393>

This Thesis is brought to you for free and open access by the Student Scholarship at University of New Hampshire Scholars' Repository. It has been accepted for inclusion in Doctoral Dissertations by an authorized administrator of University of New Hampshire Scholars' Repository. For more information, please contact [Scholarly.Communication@unh.edu](mailto:Scholarly.Communication@unh.edu).

STRUCTURE AND MECHANICAL AND TRIBOLOGICAL PROPERTIES OF MAGNETRON  
SPUTTER DEPOSITION OF STAINLES-STEEL NITRIDE AND CARBIDE THIN FILMS  
WITH TRANSITION METAL ADDITIVES

BY

Faisal I. Alresheedi

Baccalaureate Degree (BSc), Physics, Qassim University, Qassim, Saudi  
Arabia, July 2008

Master's Degree (MSc), Materials Physics, Salford University,  
Manchester, United Kingdom, May 2012

DISSERTATION

Submitted to the University of New Hampshire

in Partial Fulfillment of

the requirement for the degree of

Doctor of Philosophy

in

Physics

May, 2018

This thesis has been examined and approved in partial fulfillment of the requirements for the degree of Doctor of Philosophy in Physics by:

Thesis Director, James E. Krzanowski, Professor of Materials Science

Olof E. Echt, Professor of Physics

F. William Hersman, Professor of Physics

Carmela Amato-Wierda, Associate Professor of Materials Science

Jiadong Zang, Assistant Professor of Physics

On 12-11-2017

Original approval signatures are on file with the University of New Hampshire Graduate School.

Dedicated to my parents and my wife

## **ACKNOWLEDGEMENTS**

I am deeply grateful to my PhD thesis advisor Professor James Krzanowski for the help, encouragement, guidance, and enthusiasm he has given me through this study. Actually, he is the greatest and most respectable professor I have ever met.

It is a pleasure to thank the technical staff at the University of New Hampshire Instrumentation Center (UIC), particularly Nancy Cherim for her help in the scanning electron microscopy (SEM) and transmission electron microscopy (TEM) FIB samples preparation. Also, I would like to extend my thanks to Mr. John Wilderman for his generous help in teaching me how to run the x-ray photoelectron Spectroscopy (XPS).

I greatly appreciate Qassim University in Saudi Arabia for their fund and support during my study.

I wish to express my thanks to my parents and my wife for their support and encouragement until I could complete this research.

# TABLE OF CONTENTS

DEDICATION .....	iii
ACKNOWLEDGEMENTS.....	vii
LIST OF TABLES .....	viii
LIST OF FIGURES .....	xii
ABSTRACT .....	xiii

## Contents

Chapter 1: Introduction .....	1
1.1 Stainless Steels Introduction and History .....	1
1.2 Classification of Stainless Steel .....	2
1.2.1 Martensitic .....	3
1.2.2 Ferritic .....	3
1.2.3 Duplex stainless steel .....	4
1.2.4 Precipitation hardening grades.....	5
1.2.5 Austenitic grades.....	6
1.3 The effect of the alloying elements on stainless steel.....	7
1.4 Structure of the Thesis.....	10
Chapter 2: Background .....	13
2.1 Surface Hardening of Austenitic Stainless Steel .....	13
2.1.1 Introduction .....	13
2.1.2 Surface Nitriding Methods.....	14
2.2 Expanded austenite (S-Phase) .....	16
2.2.1 S-Phase History .....	16
2.2.2 Microstructure and characteristics:.....	17
2.2.3 S-Phase Formation within Surface Hardening .....	19
2.2.4 Theories on the structure of the S-phase .....	22
2.5 Nitrogen Diffusion and Thermal Stability within S-Phase.....	28
2.6 Tribology .....	30

2.7 Thin Film Growth.....	32
2.7.1 Sputter Deposition Basic Principles .....	33
2.7.2 Magnetron Sputtering .....	35
2.7.3 Gases Used during Sputtering Process .....	38
Chapter 3: Experimental Procedures.....	39
3.1 Film Deposition .....	39
3.2.1 X-ray Diffraction (XRD) .....	43
3.2.2 X-ray Photoelectron Spectroscopy (XPS) .....	45
3.2.3 Scanning electron microscope (SEM).....	46
3.2.4 Transmission electron microscope (TEM).....	48
3.2.5 Hardness .....	50
3.2.6 Pin-On-Disk .....	52
Chapter 4: Structure and morphology of stainless steel coatings sputter-deposited in a nitrogen/argon atmosphere.....	54
4.1 Film Composition Analysis .....	54
4.2 X-ray Diffraction .....	58
4.3 Film Morphology .....	67
4.4 Mechanical Properties .....	72
4.5. Discussion.....	74
4.6. Conclusions .....	76
Chapter 5: The Effects of Ti Additions on the Structural, Mechanical and Tribological Properties of Stainless Steel-Nitride Thin Films.....	78
5.1 Composition Analysis of SS-Ti-N Films .....	78
5.2 Crystal Structure .....	81
5.3 Microstructural Characterization.....	85
5.4 Mechanical and Tribological Properties of SS-Ti-N .....	88
5.5 Discussion.....	92
5.6 Conclusions .....	93
Chapter 6: A comprehensive study of the effect of R-Values on Nitrogen and Substrate Temperature on SSN-60V and selected films from Chapters 4 and 5.....	94
6.1 X-ray diffraction spectrum Results.....	94
6.2 Effect of the variation in nitrogen concentration in the films and the substrate temperature .....	97
6.3 Effect of Variation in R-value with Nitrogen Concentrations and Substrate Temperature.....	99
6.4 Influence of R-values on the Morphology of Low Titanium Films .....	102

6.5 Determination the Effect of Stacking Faults on The shift in the Peak Positions Using Warren’s Model .....	106
6.6 Discussion.....	108
6.7 Conclusions .....	112
CHAPTER 7: The Effects of increasing Cr concentration on the Structural, Mechanical and Tribological Properties of Stainless Steel-Nitride Thin Films.....	113
7.1 Deposition Parameters and Composition Analysis of SS-Cr-N Films .....	113
7.2 XRD Analysis.....	116
7.3 Microstructural Characterization.....	119
7.4 Mechanical and Tribological properties of SS-Cr-N .....	121
7.5 Discussion.....	125
7.6 Conclusions .....	125
CHAPTER 8: Expanded Austenite in Stainless Steel Carbide .....	127
8.1 Film Composition Analysis of SSC .....	127
8.2 XRD Results .....	129
8.3 Mechanical Properties .....	132
8.4 Discussion.....	133
8.5 Summarize and Conclusions .....	134
Chapter 9: Summary and Conclusion.....	135
References .....	140

## LIST OF TABLES

Table 1.1: Classification of Stainless Steel by Microstructure .....	2
Table 2.1: The calculated values of stacking fault parameter $G_{hkl}$ and elastic constant $(S_1)_{hkl}$ for different reflections.....	26
Table 4.1: Composition Analysis of Deposited Films .....	55
Table 5.1: Deposition parameters and film compositions for the SS-Ti-N films .....	80
Table 5.2: Interplanar spacing and Lattice Constant Data .....	84
Table 5.3: Table 3: Pin-on-disk friction test results .....	91
Table 6.1: Description of Samples Deposited and Basic Parameters .....	96
Table.7.1: The effect of power, substrate temperature and substrate bias on the composition of SS-Cr-N films .....	115
Table. 7.2: The interplanar spacing lattice constant values .....	118
Table 7.3: Pin-on-disk friction test results of SS-Cr-N selected films.....	124
Table 8.1: Deposition Parameters and Carbon Content for SS-Carbon Films for states 1 and 2 ...	128
Table 8.2 Deposition Parameters and Carbon Content for SS-Carbon Films; state 3 .....	128

# List of Figures

Figure 1.1: Shows a Duplex microstructure of ferrite and austenite phases [11] ..... 4

Figure 2.1: Shows a cross-section micrograph of austenitic stainless steel film grade 304 deposited at 420C for 70 min [24]. ..... 14

Figure 2.3: Shows the nitrogen content in films vs. the nitrogen composition in a mixed gas..... 22

Figure 2.4: The XRD pattern of “m-phase” observed from a 316 stainless steel grade for film with a nitrogen content of 30 at. % [50]..... 24

Figure 2.5: Shows an examining of a nitrogen profile as a function of a depth from a film deposited by ion implantation using a 321 stainless steel grade [64]. ..... 28

Figure 2.6: Shows the mean free path between two collisions..... 33

Figure 2.7: Shows a magnetron sputtering schematic [54] ..... 34

Figure 2.8a: “Schematic drawing of a cross section of a balanced magnetron, displaying the magnetic field lines as closed loops above the target surface. Between the inner and outer magnetic rings the target displays an erosion track, or the so-called race track (taken from ref 83). ..... 37

Figure 2.8b: “Schematic drawing of a cross section of an unbalanced magnetron (type II), displaying the magnetic field lines as only partially closed loops above the target surface. Here, the electrons can more easily escape and travel towards the substrate region (taken from ref 83). ..... 37

Figure 3.1: The reactive magnetron sputter depositon system used in the research..... 42

Figure 3.2: Shows an illustration that demonstrates the principle of the X-ray diffraction technique..... 44

Figure 3.3: Principle of generating of a photoelectron in the XPS..... 46

Figure 3.4: Electron beam-specimen interactions in the SEM..... 47

Figure 3.5: Shows transmission electron microscopy (TEM) schematic diagram..... 49

Figure 3.6: Schematic of the Knoop indenter and the impression shape..... 50

Figure 3.7: Shows the pin-on-disk working principle..... 53

Figure 4.1: The nitrogen/metal ratio vs. substrate temperature for films deposited at various substrate bias levels and sputter gas compositions. The ratio increases with fraction of N2 in the sputtering gas, but decreases with increasing substrate temperature..... 57

Figure 4.2: XRD results for films deposited at -100V and a range of substrate temperatures (indicated). Also shown are possible matches to known phases. The upper temperature range (500-600oC) matches CrN, bcc-Fe and Ni, whereas below 450°C the structure is primarily S-phase ..... 59

Figure 4.3: XRD scans for four selected films in the vicinity of the (111)/(200) peaks, with further detail of the (111) peak positions shown on the right. The substrate bias levels and gas flow rates are indicated for each scan. .... 60

Figure 4.4: Example of an area-detector frame showing the (111)/(200) Debye rings, selected integration segment and integration results. Ten integrations were carried out along the Debye ring to obtain the lattice constant vs.  $\psi$  data shown in Figs. 4.5..... 62

Figure 4.5: Measured lattice constants based on (111) and (200) peaks vs.  $\psi$  angle. The lower plot shows the results for a Cu powder standard indicating acceptable alignment over the range of  $\psi$  angles used. The upper plot shows  $a_{111}$  and  $a_{200}$  for films deposited at -100V, 20Ar/5N2 and 200 and 300°C. The decline in  $a_{200}$  with  $\psi$  is notable and contrasts with the relatively constant values for  $a_{111}$ . The peak positions were determined using a pseudo-Voigt peak-fit routine and the error bars represent the calculated variance in the peak position ..... 64

Figure 4.6: Measured lattice constants v.  $\psi$  for a film deposited at -100V, 20Ar/5N2 and 200oC and then subsequently annealed at 400oC for 30 minutes. There is a slight reduction in lattice constant after annealing, possibly due to the out-diffusion of nitrogen ..... 66

Figure 4.7: SEM cross-section images of selected films: (a) -100V, 250oC, 20Ar/5N2, (b) -140V, 450oC, 20Ar/5N2, (c) -100V, 500oC, 20Ar/5N2, (d) -140V, 250oC, 12Ar/12N2. Films (a), (b), and (d) show generally columnar structure with a faceted and angular morphology ..... 68

Figure 4.8: SEM cross-section images of selected films deposited at 12Ar/12N2 and -100V at temperatures of (a) 150oC, (b) 350oC, and (c) 450oC. Film (a) shows a typical columnar morphology, but the structure becomes more faceted and discontinuous as the temperature increases ..... 70

Figure 4.9: (a) SEM image a film deposited at 350 °C, -100 V and 15Ar/10N2, showing a layer-like morphology within the columns giving a “ribbed” appearance to the column edges. (b) TEM image of the same film, showing a segmented or mosaic appearance with..... 71

Figure 4.10: Knoop hardness measurements vs. deposition temperature for films deposited at the indicated parameters. The highest hardness achieved was near 2100 kg/mm2 for the film deposited at 450°C/-140V/20Ar/5N2. .... 73

Figure 5.1: (a) XRD diffraction patterns of the films from groups 1 and 2, and (b) groups 3 and 4. Indexed lines for (111), (200) and (220) reflections are shown. ....	83
Figure 5.2: (111) rocking curves for the films in Group 3, for $\omega$ values ranging from -45 to +45o. Deposited films are: (a) G3-25; (b) G3-150; (c) G3-250 and (d) G3-350. ....	84
Figure 5.3: SEM cross-section images for films: (a) G1-25, (b) G1-150, (c) G1-250, and (d) G1-350. All images were taken in the secondary electron mode .....	86
Figure 5.4: SEM cross section images for films deposited from group 3 at substrate temperatures of (a) 150°C; (b) 250°C and (c) 350°C.....	87
Figure 5.5: Nano-indentation hardness and reduced elastic modulus, $E_r$ , for selected films. The average standard deviation in the measured hardness values was $\pm 1.6$ GPa.....	89
Figure 5.6: Wear track optical microscope images showing a typical portion of the wear track after 1000 cycles: (a) G2-25, (b) G3-25, (c) G3-150 and (d) G3-250.....	91
Figure 6.1: X-ray diffraction spectrum from a sputter-deposited SS304+N2 film, deposited at 150oC and -60V bias. The two peaks are indexed as (111) and (200) based on an FCC structure. An additional spectrum (not shown) was obtained at the higher $2\theta$ range to obtain the peak positions for (311) and (222). The analyzed data are shown in the table, demonstrating the deviation in the (200) lattice spacing; the normal position for the (200) peak should be at $45.5^\circ$ , indicating a (200) shift of $1.4^\circ$ to lower angles.....	95
Figure 6.2: Variation in nitrogen concentration in the films vs the substrate temperature. Note there is no consistent temperature dependence observed within this temperature range.....	98
Figure 6.3: Variation in nitrogen content with R-values for all data given in Table 4.1. A systematic trend is observed where decreased N concentrations correspond to higher R-values. ....	100
Figure 6.4: R-values vs. substrate temperature for films deposited at different substrate bias levels as well as films co-deposited with Ti. Except for the high-Ti films (which also had stoichiometric nitrogen levels) the R-values declined with increasing temperature.....	101
Figure 6.5: SEM cross-section images of films deposited at low-Ti concentrations: (a) S-Ti-25-100L, (b) S-Ti-150-100L, (c) S-Ti-250-100L and (d) S-Ti-350-100L. Images all show evidence of a layered morphology within the columnar structures, and a general coarsening of the structures as the substrate temperature is increased. ....	103

Figure 6.6: TEM image samples deposited at -60V bias: (a) S-150-60, (b) S-250-60, and (c) S-350-60. Examples of a layer-morphology can be found throughout (a) but the films become more dense as the substrate temperature is increased..... 105

Figure 6.7: Proposed model for the S-phase structure: (a) normal stoichiometric nitride structure; (b) nitride structure with approximately 50% nitrogen interstitials removed; (c) distorted lattice resulting from the relaxation of the metal sublattice..... 111

Figure 7.1: X-ray diffraction patterns showing the effect of (a) bias, (b) temperature and (c) gun power ratio on the structure and texture of the deposited films.....117

Figure 7.2 SEM cross-section images for films: (a) 250C, -100V, (SS:1/Cr:3) (b) 250C, -140V, (SS:1/Cr:3) (c) 250C, -140V, (SS:1/Cr:1) and (d) 350C, -100V, (SS:1/Cr:1).....120

Fig. 7.3: The hardness of SS-Cr-N films deposited at different effects (a) effect of substrate temperature; (b) effect of varied bias; (c) effect of applying different power ratio.....122

Figure 7.4: The friction coefficient of the SS-Cr-N films deposited at 150C-350C with bias varied between -100-140V and a constant SS/Cr sputter guns power of 50W/150W.....124

Fig. 7 (a-d) SEM cross-section.....125

Figure 8.1: XRD diffraction patterns for SS-carbon films deposited at -140V bias and temperature ranging from 25-450C (state 1).....129

Figure 8.2: XRD diffraction patterns for SS-carbon films deposited at -140V bias. As the temperature increases, the films showed more phases including FeC, CrC and Ni.....130

Figure. 8.3: SSC films deposited at a 250C and varied carbon power ranging 25W-150W with keeping the stainless steel sputter gun power at 150W.....131

Figure 8.4: Hardness data for SS-carbon films. The higher hardness levels observed in state 2 films were due to higher (near 50 at. %) concentrations of carbon in the films.....132

Figure 8.5: The Knoop hardness of SCC for films deposited at state 2 where films deposited at powers varied between 25W and 150W as a function of the Knoop hardness.....133

## ABSTRACT

# STRUCTURE AND MECHANICAL AND TRIBOLOGICAL PROPERTIES OF MAGNETRON SPUTTER DEPOSITION OF STAINLES-STEEL NITRIDE AND CARBIDE THIN FILMS WITH TRANSITION METAL ADDITIVES

by

Faisal I. Alresheedi

University of New Hampshire, May, 2018

Since the initial discovery of the S-phase in 1985, understanding the structural nature of this phase and the anomalous shift of the (200) diffraction peaks has been a challenging problem. Austenitic stainless steels, ternary Fe–Cr–Ni alloys, like AISI 304, demonstrate excellent corrosion resistance and relatively good levels of toughness and strength. For this reason, they are widely used engineering materials in areas such as aerospace, construction buildings, piping, telecommunications, chemical and petrochemical applications. However, stainless steels have a relatively low hardness, and this leads to a poor wear resistance, resulting in a short lifetime that limits its use in industrial applications. Therefore, surface treatment methods have been developed to improve its mechanical properties without loss of corrosion resistance. Surface hardening of stainless steels can be accomplished using a combination of nitrogen implantation and diffusion to create a hardened surface layer. The incorporation of nitrogen into stainless steels by these techniques results in expansion of the fcc (austenite) lattice; this phase is referred to as “expanded austenite,” or the “S-phase”. A notable feature of the S-phase is the displacement of the (200) reflection from its expected position.

The reactive magnetron sputtering process has been used to deposit thin films of nitrogen-supersaturated stainless steels. In addition, new hybrid coatings were studied by combining stainless steel targets with other transition metals, as well as carbon, in the deposition process. A variety of advanced characterization methods were used to examine the structural, compositional, mechanical and tribological properties of these films. These techniques include x-ray photoelectron spectroscopy (XPS), X-ray diffraction (XRD), scanning electron microscopy with energy dispersive x-ray spectroscopy (SEM-EDX), transmission electron microscopy (TEM), micro-hardness (Knoop indenter), nano-Indentation, and both pin-on-disk and optical microscopy tests for tribological evaluations. In addition, the structural nature of the films was further examined using area-detector based x-ray diffractometry.

Using 304 stainless steel sputtering targets, films were deposited in a mixed Ar/N atmosphere using a variety of Ar/N ratios, as well as parametric variations in substrate bias and temperatures and sputter gun power ratios. XPS analysis showed nitrogen supersaturation levels near 40 at.% in these films. X-ray diffraction analysis showed the structures of the films were strongly temperature dependent: above 450 °C, the films were a mixture of CrN, bcc-Fe, and Ni; below 450 °C, the films were nominally fcc-structured. However, the common anomalous deviation in the position of the (200) reflection was observed, indicating the presence of the S-phase. Area-detector based X-ray diffraction studies, which allowed peak position measurements as a function of the inclination of the diffraction vector (angle  $\psi$ ), showed  $a_{200}$  declined with increasing  $\psi$ , but always remained greater than  $a_{111}$ , which was relatively constant with  $\psi$ . Hardness was measured and also found to be a strong function of

substrate temperature, with the highest hardness of 2100 kg/mm<sup>2</sup> obtained for films deposited at room temperature. SEM and TEM cross-section samples showed uncommon morphological features which provided insight into the structural nature of the S-phase.

Hybrid stainless steel /titanium nitride (SS-Ti-N) films, as well as a hybrid stainless steel/chromium nitride (SS-Cr-N) coatings were investigated and showed superior mechanical properties that may be promising new coatings. The S-phase was also produced in these hybrids coatings. In the SS-Ti-N, titanium concentrations of up to ~14 at.% were obtained, in which case the nitrogen levels were near stoichiometric (50 at.%N). Hardness levels of 18-24 GPa (~1800-2500 Kg/mm<sup>2</sup>) were obtained for the films that had titanium concentrations between 10-14 at.%. These S-phase films made by co-sputtering from both stainless steel and titanium targets could increase the hardness by nearly 100% compared to films made with only stainless steel. A tribological analysis of the films was conducted using a pin-on-disk test with an alumina ball, and the optimal results were obtained on a SS-Ti-N film deposited at 150°C/ -140V, where the average friction coefficient was 0.39. It should be noted that the average of regular stainless steel is 0.6

For the SS-Cr-N films, chromium concentrations of up to 54% were obtained and showed a maximum hardness of ~4639.8 Kg/mm<sup>2</sup> for a film deposited at 250C and -140V. These films tend to have a nitrogen concentration of ~40%. The S-phase was formed in these coatings and the (200) peak also shifted from expected positions. The friction coefficient of the SS-Cr-N coated films was examined and showed an improved friction coefficient (0.41) at film deposited at 150C.

Further studies of N-supersaturated films deposited stainless steel and stainless steel co-sputtered with titanium were conducted to better understand the structural nature of the S-phase. In order to quantify the peak shift in these films, a term denoted the “R-value” was used, which for an FCC structure is given by:

$$R = \frac{\sin^2 \theta_{111}}{\sin^2 \theta_{200}} \quad (1)$$

An R-value of 0.75 is expected for normal fcc structures; a value of  $R > 0.75$  indicates the presence of the S-phase. The effect of nitrogen and titanium concentrations, substrate temperature and the morphology on R-value was investigated. R-values were generally  $> 0.75$ , indicating a deviation from the common fcc structure. The samples with R closest to 0.75 were films with higher titanium levels (10-14 at.% Ti), and these films had stoichiometric nitrogen concentration levels (~50 at.% N). Also, films that have a nitrogen content of 30-43% do not show a consistent relationship to high or low R-values. SEM cross-section of the S-phase films deposited at lower bias showed a layered or ribbed morphology in the coarse columns. TEM images revealed a central spine and branched structure in films deposited at 150C and 250 °C, with fewer branches at 350C. Additionally, increasing the substrate temperature from 150 to 350 °C led to a decrease in the R-value (from 0.802 to 0.779) made the films denser. The effect on the peak shift ( $\Delta 2\theta$ ) calculated and the shift was 0.022°, however, this number was far from the value of  $\Delta 2\theta$  measured from our XRD data. It was concluded that the observed layered morphology does not explain the measured R-values.

Films of stainless steel/carbon were also deposited by co-sputtering. This was done because carbon offers another way to make an alternative version of S-phase using carbon instead of nitrogen. These films maintained S-phase structure when deposited below 450°C. Carbon concentrations near 50% were obtained in several cases, and the hardness of these films reached a maximum value of 2256 Kgf/mm<sup>2</sup> at a deposition temperature of 250°C. In comparison to SSN, SSC has an improved hardness.

# Chapter 1: Introduction

## 1.1 Stainless Steels Introduction and History

Stainless steels are alloys of iron, nickel, chromium and additional elements that are added based on the specific stainless steels grade in order to improve the properties of these steels. They are commonly classified as low carbon steels ( $< 1.2$  wt.% C) and contain at least 10.5% (wt%) chromium [1,2]. The presence of chromium is essential because it forms a thin oxide layer on the surface which is known as a passivation layer. This layer helps to prevent any further corrosion of the steel as a whole. Consequently, the corrosion resistance can be increased by increasing the chromium concentration in the stainless steel [1-3].

To increase the corrosion resistance, improve the formability, increase machinability, and create a harder alloy, nickel and molybdenum can be added to obtain these beneficial properties [2,4-5]. Thus, stainless steels are typically found in applications dealing with aerospace, automotive and medical industries.

The original discovery of stainless steels can be traced to the early 18<sup>th</sup> and 19<sup>th</sup> centuries after the discovery of chromium as an element [6]. In 1821, Pierre Berthier, a French engineer, found that the stiffness of the iron alloys can be enhanced by adding a specific amount of chromium to it [7]. Additionally, this led to an improvement in the iron's corrosion resistance to acids. The microstructure of Fe-Cr and Fe-Cr-Ni alloys were first studied in France in 1909 by Léon Guillet and Albert Portevin [8]. The minimum percentage of chromium (10.5 percent) which was needed to impart rust-prevention properties to steels was specified by P. Monnartz, a German

metallurgist, in 1911 [7]. When this new chromium rich alloy was exposed to the atmosphere, it did not rust or corrode. This new steel was labeled as “rostfrei Stahl” in Germany, “acier inoxyable” in France and “rustproof or rustless iron” in the United Kingdom [9]. In the United States and the United Kingdom, it was given the name of “stainless steel”, which is still used today. In 1913, the first stainless steel casting was produced in Sheffield, England [9].

## 1.2 Classification of Stainless Steel

Throughout the years, the variety of applications for stainless steel alloys has caused the overall number of alloys to expand quickly. Due to the large quantity of alloys, stainless steels are divided into five groups. Four of them (martensitic, ferrite, duplex and austenitic) are dependent on the microstructure or the crystal structure of these alloys. The last one is a precipitation hardened group, which is based on the type of heat treatment used [10]. These types, and their general compositions are shown in Table 1.1.

**Table 1.1** Classification of Stainless Steel by Microstructure [2]

Stainless Steel Types	Typical Composition
Martensitic stainless steels	12-18 wt.% Cr, < 1.2 wt.% C
Ferritic stainless steels	17-30 wt.% Cr, < 0.2 wt.% C
Austenitic stainless steels	18-25 wt.% Cr, < 8-20 wt.% Ni
Duplex stainless steels	18-26 wt.% Cr, < 4-7 wt.% Ni, 2-3 wt.% Mo
Precipitation hardening stainless steels	12-30 wt.% Cr

### 1.2.1 Martensitic

Martensitic stainless steels are alloys of iron (Fe), chromium (Cr) and carbon (C). This grade has a small amount of carbon (less than 1.2 wt.%) and contains 12-18 wt.% Cr with the balance iron [2].

Martensitic stainless steels show the following properties [9]:

- (i) Ferromagnetic
- (ii) Heat treatment by quenching can be used to harden the steel alloys
- (iii) In the hardened state, they have moderately good toughness and high strength
- (iv) They have the lowest corrosion resistance compared to the other stainless steels grades.

Overall, due to their good strength and hardness they can be used in many applications (i.e. - engines, valves, hydroelectric power stations, petrochemical, and chemical applications) [5].

### 1.2.2 Ferritic

Ferritic stainless steels have a body centered cubic (bcc) crystal lattice [9]. At room temperature, the structure is bcc and is commonly called  $\alpha$ -iron. At high temperature, it is known as  $\delta$ -ferrite. Also, ferritic stainless steels mainly contain chromium 17-30 wt.% and often contain less than 0.2% of carbon [2].

Ferritic stainless steels show the following properties [9]:

- (i) They are ferromagnetic.
- (ii) They exhibit bcc crystal structure because of the high content of chromium they have.

(iii) They are not heat-treatable. However, by cold working, harder ferritic stainless steels can be obtained. However, this type of stainless steels is commonly used in the annealed state.

(iv) They show poor weldability like martensitic stainless steels.

When moderate corrosion resistance is needed, and toughness is not a significant need, ferritic stainless steel is regularly used. Typical applications include automotive components and heat transfer equipment for the chemical and petrochemical domains.

### 1.2.3 Duplex stainless steel

Duplex stainless steels grades contain a high percentage of Cr ranging from 18 to 26 wt% and have a low nickel content ranging from 4 to 7 wt%. In addition to these two elements, molybdenum is also added, and this results in a combination structure consisting of both austenite and ferrite phases [9]. Because of the low nickel content, duplex stainless steels grades have lower cost compared to the other stainless steels.

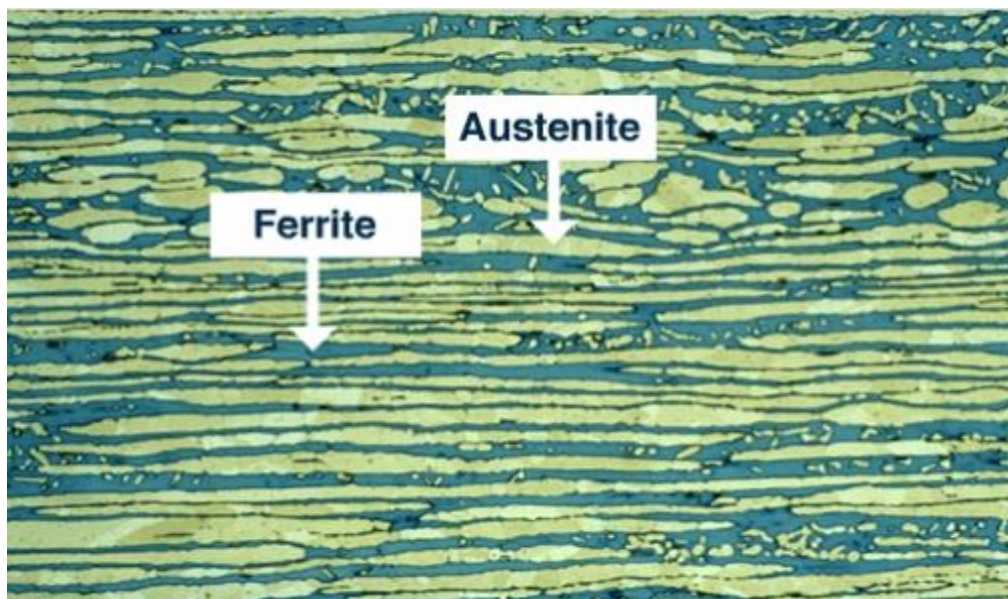


Figure 1.1 Shows a Duplex microstructure of ferrite and austenite phases [11]

Duplex stainless steels include the following properties [9]:

(i) Magnetic

(ii) Good Weldability

(iii) High resistance to stress corrosion cracking

#### 1.2.4 Precipitation hardening grades (PH)

Precipitation hardening (PH) stainless steels are magnetic and hardened by a unique mechanism that forms precipitates within the steels' microstructure. In these grades, the strength can be highly improved through a low-temperature heat treatment. The starting microstructure of the PH alloys is usually austenite. Before the precipitation hardening can be successful, a thermal treatment is used to transform it to martensite [9]. In the applications where a moderate corrosion resistance and excellent formability and strength are needed, these alloys are commonly used. These applications include aircraft hardware, shafting, and high-pressure pumps. Most PH grades contain Titanium (Ti), Cobalt (Co), Aluminum (Al) and Copper (Cu). They are added to assist precipitation hardening in the steel. Also, most PH steels contain Molybdenum and Vanadium for tempering resistance [13].

In summary, precipitation hardening stainless steels are used in aerospace, food, chemical and petrochemical applications. Also, they are used in gears, valves components and turbine blades [12, 14].

### 1.2.5 Austenitic grades

Austenitic stainless steel is known as the iron-chromium-nickel (Fe-Cr-Ni) alloy. It contains 18-25 wt% of chromium and 8-20 wt% nickel and the balance Iron (Fe) [4]. It exhibits a unique austenite ( $\gamma$ - fcc) structure even at room temperature. These alloys provide good toughness and good to moderate levels of strength along with excellent corrosion resistance in many corrosive environments. Austenitic stainless steels are the most commonly used family of stainless steels due to the large number of alloys and good corrosion resistance. These alloys were investigated in 1910 after adding nickel to chromium- iron alloys. Based on the American Iron and Steel Institute (AISI), austenite grade provides around 70-80% of the overall productions of stainless steels [2,5].

Austenitic stainless steels include the following properties [9]:

- (i) They are ferromagnetic;
- (ii) Have face centered cubic (fcc) crystal structure;
- (iii) Are non-magnetic;
- (iv) Have better corrosion resistance compared to other grades;
- (v) Can be easily welded;
- (vi) In many corrosive environments, they show excellent corrosion resistance at both high and low temperatures;
- (vii) Have good toughness and ductility.

Additionally, according to AISI, austenitic stainless steels are divided into three categories [17]:

(i) AISI 200 categories alloys (iron-chromium-nickel-manganese)

(ii) AISI 300 categories alloys (iron-chromium-nickel)

(iii) Nitrogen-infused alloys (where nitrogen elements are infused to stainless steel grades).

Even though austenitic stainless steels have all these beneficial properties and are widely used in many industrial applications, for example, nuclear, aerospace, telecommunications, chemical, and petrochemical industries, they have some drawbacks that limit their use. One significant limitation is their poor tribological properties, such as high friction and poor wear resistance (an inherent property of the austenitic structure) [15, 16].

### 1.3 The effect of the alloying elements on Stainless Steel

Various alloying elements are combined with stainless steels modify the steel's properties, where each element has a particular effect. The effect of the alloying elements on the properties and structure are described below [10,17-20].

#### **Chromium (Cr)**

Chromium is the most valuable material added to the stainless steels. The steel's corrosion resistance, wear resistance and toughness are increased as more chromium is added to the alloys. At high temperature, the corrosion resistance also increases the resistance to oxidation. Furthermore, chromium has the same ferritic microstructure as room temperature (bcc) Fe.

### **Nickel (Ni)**

Nickel is added to the steels in order to promote an austenitic (fcc) structure. In general, nickel improves toughness and ductility as well as decreases the rate of corrosion. When used in precipitation hardening steels, the presence of nickel helps form intermetallic phases, increasing the alloy series' strength.

### **Manganese (Mn)**

Manganese is commonly used to enhance the hot ductility. At low temperatures, manganese tends to be an austenitic stabilizer, but at high temperatures, it stabilizes the ferritic structure. In order to get higher nitrogen content in the austenitic steels, manganese is added because it increases the nitrogen solubility.

### **Molybdenum (Mo)**

Molybdenum significantly raises the corrosion resistance and the strength of stainless steels. Stainless steels which contain molybdenum have higher corrosion resistance than the others grades that don't have molybdenum in them. Furthermore, molybdenum induces a ferritic structure.

### **Silicon (Si)**

Adding even a small amount of silicon to the austenitic stainless steels will enhance the resistance to oxidation, and at high temperature, it prevents the alloys from carburizing. Silicon promotes a ferritic structure.

### **Carbon (C)**

Stainless steels always contain carbon. In all grades, the carbon content is kept low except for the martensitic alloys. In the martensitic grades, the carbon level is intentionally increased to gain higher hardness and strength. In ferritic stainless, the presence of carbon decreases the corrosion resistance and the toughness. In the martensitic-austenitic and martensitic steels, carbon improves strength and hardness. It should be noted that carbon promotes an austenitic structure.

### **Copper (Cu)**

For exposure to specific acids, copper can be added to improve the corrosion resistance. Also, in precipitation hardening steels, it is mainly used to form the intermetallic compounds which are utilized to enhance the strength. Copper promotes an austenitic structure.

### **Nitrogen (N)**

The combination of nitrogen with molybdenum is generally accompanied with increasing the corrosion resistance. The presence of nitrogen in ferritic stainless steels reduces corrosion resistance and toughness. In both martensitic and martensitic-austenitic steels, hardness and strength are increased while the toughness is reduced. The typical concentration is 0.10-0.30 wt. %. Nitrogen promotes an austenitic structure.

### **Titanium (Ti)**

The effect of adding titanium to stainless steel varies from alloy to alloy. For austenitic steels, at high temperature, the hardness is improved and the resistance to the corrosion is increased. For ferritic stainless alloys, it improves the alloy's toughness and corrosion resistance. In

precipitation hardening alloys, the titanium helps form intermetallic compounds that make the alloy stronger.

### **Sulfur (S)**

Sulfur is added to specific stainless steels with the goal of improving the machinability. It also decreases fabrication properties (weldability and formability), corrosion resistance, and ductility.

## **1.4 Structure of the Thesis**

This thesis is focused on the use of reactive magnetron sputtering to study the structure and mechanical properties of nitrogen-containing AISI 304 stainless steel (SS-N) thin films deposited in a mixed argon/nitrogen atmosphere at a wide range of parameters. In addition, the same method was used to investigate new coatings by co-depositing films from AISI 304 stainless steel and titanium targets and chromium bulk materials. A new version of the S-phase was also produced in this study by co-sputtered AISI 304 stainless steel and carbon with the use of argon gas.

The thesis is divided into nine chapters. In addition to this introduction, chapter 2 provides a background on nitriding and surface hardening of stainless steels, as well as the history of the S-phase in both bulk nitride and thin-film deposited stainless steels. The mechanisms of surface hardening due to the S-phase, and the improvements in mechanical properties obtained are reviewed. In addition, the most common hypotheses that described the structure of the S-phase are discussed.

In Chapter 3, the main experimental methods that have been applied throughout the course of the study are explained. Detailed information on the procedures used to characterize the structural and mechanical properties on the deposited thin films are also described.

The results start with chapter 4. In this section, the effects of various deposition parameters on SS-N films were examined in order to improve the mechanical properties of austenite stainless steels. Also, the structural nature of the S-phase was further characterized using area-detector based x-ray diffractometry.

In chapter 5 and 6, new coatings were investigated by co-depositing films from stainless steel and titanium targets (SS-Ti-N) as well as co-depositing films from stainless steel and chromium (SS-Cr-N) targets. This was done to enhance the mechanical properties and wear resistance of the austenitic stainless steel films. The structure of these films was examined and had primarily the S-phase. Also, these films had a very high hardness which may promote their use in the machining industries.

In chapter 7, a comprehensive study is presented on the effect of nitrogen concentration and substrate temperatures on the structure of stainless steel nitride films using selected films from Chapter 5 and 6. These studies are focused on understanding the S-phase structure by quantifying the peak shift using a term denoted the "R-value". These results are followed by a presentation on the correlation between nitrogen concentration and R-values as well as between R-values and substrate temperature. In addition, the stacking fault hypothesis for the S-phase structure is critically examined.

Chapter 8 includes an investigation of a new version of the S-phase made by co-sputtered stainless steel/carbon (SSC) in argon gas. The mechanical properties were also evaluated in hopes of improving its hardness.

Lastly, chapter 9 gives a summary of the results and conclusions that were obtained from chapter four to eight as well as the outcomes that could be inferred from those results. The chapter ends with short suggestions for promising and beneficial future work.

## Chapter 2: Background

### 2.1 Surface Hardening of Austenitic Stainless Steel

#### 2.1.1 Introduction

Austenitic Stainless steels, ternary Fe–Cr–Ni alloys, such as AISI 304 demonstrate excellent corrosion resistance and relatively good levels of toughness and strength, and for this reason, they are widely used in engineering materials [21,22]. However, stainless steels have a relatively low hardness, and this leads to a lower wear resistance, resulting in a short lifetime which limits its use in industrial applications. Therefore, research has been conducted to develop new technologies to improve the hardness and wear resistance of stainless steels without a loss in corrosion resistance. One approach is to diffuse nitrogen into the metal surface to improve the hardness [23].

To improve the wear resistance of a stainless steel alloy, an approach known as nitriding can be helpful. Nitriding is a technique that uses thermal processing in order to diffuse nitrogen into a metal surface to improve the surface hardness [23]. Usually, these techniques are aided by the presence of molybdenum, aluminum, chromium, or titanium. These elements are known as nitride formers. By forming these nitrides within the metal matrix, properties of these nitride compounds can be enhanced. When nitriding, the alloy composition, and processing parameters affect the proportion and composition of the expected nitride compounds, for example, CrN and TiN. Fig. 2.1 [24] shows a micrograph of image of a cross-section of a nitrided

film deposited to reach a thickness of 10  $\mu\text{m}$  (the topmost white treated film or nitrided layer). The nitrided layer does not show any evidence of diffusion layer into austenitic stainless steel.

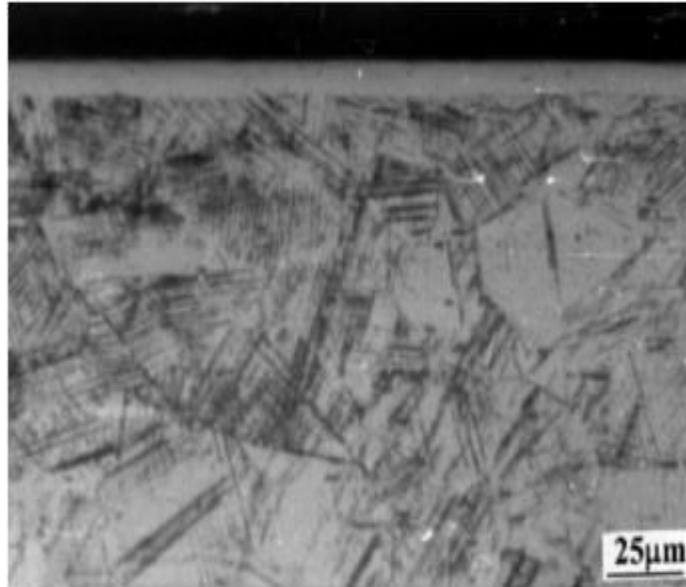


Figure 2.1: Shows a cross-section micrograph of austenitic stainless steel film grade 304 deposited at 420C for 70 min [24].

### 2.1.2 Surface Nitriding Methods

Several methods have been recently used in order to improve the properties of stainless steels surfaces by implanting or diffusing nitrogen to create a hardened surface layer. The most common methods involve exposure to a nitrogen-containing plasma at elevated temperatures, which [25–33] can be achieved using the following methods:

**Plasma immersion ion implantation (PI<sup>3</sup>)** [33,34] which is a surface modification technique where ions from a plasma are accelerated towards a target by applying a pulsed DC or pure DC

voltage on the target. The target is held at a specific temperature (300-500C) to allow the ions to implant themselves within the target's crystal structure.

**Conventional ion implantation (CII)** [25,35-36], where nitrogen ions are accelerated by an electrical field and impacted into a solid. In one notable study, a low-energy ion beam (700 eV) with a high-flux ( $2 \text{ mA cm}^{-2}$ ) of ions was used [36].

Nitriding stainless steels at elevated temperatures (above 400C) are widely used in industry for improving wear resistance but this method does not improve stainless steel mechanical properties without loss of corrosion resistance, because the above techniques are applied at high temperature, which degrades the steel's corrosion resistance [25,37-40]. One potential reason for this is that nitriding at higher temperatures can lead to the precipitation of CrN which removes Cr from the solid solution [39].

In this regard, many researchers have shown that processing deposition temperature is a critical parameter. It has been cited that a low processing temperature (below 450C) is required during nitriding to preserve the stainless steel's corrosion resistance. The process of reactive sputter deposition can also be used to obtain the desired properties in the form of an overlay coating. Reactive sputtering technique is advantageous because it is carried out at lower temperatures, including room temperature, thus enabling nitride formation to take place at a higher concentration of nitrogen without precipitation [30]. This in theory creates a thin film that exhibits high hardness, good wear resistance, and high corrosion resistance.

## 2.2 Expanded austenite (S-Phase)

The incorporation of nitrogen into stainless steels by plasma nitriding or sputter-deposition techniques results in an expansion of the fcc (austenite) lattice, and this phase is often referred to as “expanded austenite”; the term “S-phase” is also used. In this section, the history, formation within surface hardening, and x-ray spectral characteristics of the S-phase is reviewed. Also, the main hypotheses explaining the displacement of the (200) XRD peak and the diffusion of nitrogen in the ‘S-phase’ will be reviewed.

### 2.2.1 S-Phase History

Expanded austenite, which is known as ‘S-phase’, is a nitrogen- rich microstructure formed on the stainless steels’ surfaces when nitrided at a comparatively low temperature. In 1985, this surface layer was first discovered when trying to enhance austenitic stainless steels’ mechanical properties. It was given the name “S-phase” by Birmingham University professors Z.L Zhang and Tom Bell [39] and Kansai University professor Kazuo Ichii [40]. These researchers, who were the first scientists to study the advantageous effect of supersaturation of interstitial austenitic stainless steels, talked about the S-phase as a way to enhance the hardness of stainless steel without losing its good corrosion resistance.

Many studies deposit coatings by keeping the processing temperature below 450C [21,25,33,39,42-45,46-49]. In this case, the wear resistance can be improved without adversely affecting the corrosion performance of the austenite stainless steels. At these lower processing temperatures, it was found that the nitride layer is free from chromium nitride participation. Also, nitrogen remains in solid solution, producing a supersaturated fcc phase.

Throughout the literature, researchers and scientists have been variously calling this surface hardened surface layer 'S-phase', 'expanded austenite' [48,49], ' $\gamma_N$  phase' [25,36,39,42] or 'm phase' (50,51). Throughout this thesis, the term S-phase will be mostly used describing the nitrided surface layer. However, it should be pointed out that the use of the term S-phase is not limited to nitride-based compounds, and, for example, is also used to describe austenitic carbon-based compounds with an fcc-based structure [52].

## 2.2.2 Microstructure and characteristics:

### 2.2.2.1 Crystallography of S-Phase

The nature or the structural details of the S-phase are still controversial over 30 years of research investigation. Even the name, 'S-Phase', has been disputed too since its discovery in 1985, and this is due to an inability to completely characterize the crystal structure of the interstitially supersaturated austenitic phase (S-phase).

The S-phase has been frequently characterized using X-ray diffraction. Fig. 2.2 shows that a typical x-ray diffraction (XRD) patterns for type of AISI 316 stainless steels films deposited at two different nitrided potentials ( $K_N$ ) ( $K_N = 0.293 \text{ bar}^{-1/2}$  and  $K_N = 2.49 \text{ bar}^{-1/2}$ ) and a film deposited without using a nitrogen gas (untreated one). These three films were heat treated at  $445^\circ\text{C}$ .

The austenite peaks for the three austenitic stainless steels films are shown in Fig. 2.2. The Bragg reflections (111) and (200) positions for nitrided films are shifted to lower angle ( $2\theta$

angles) compared to the untreated film. This shift shows a change in the stainless steels' lattice dimensions, caused mainly by the incorporation of nitrogen into austenitic interstitial sites. In addition, the film which has a higher nitride potential has a higher nitrogen content, creating a crystal structure with larger dimensions than another structure with lower nitrogen content [53].

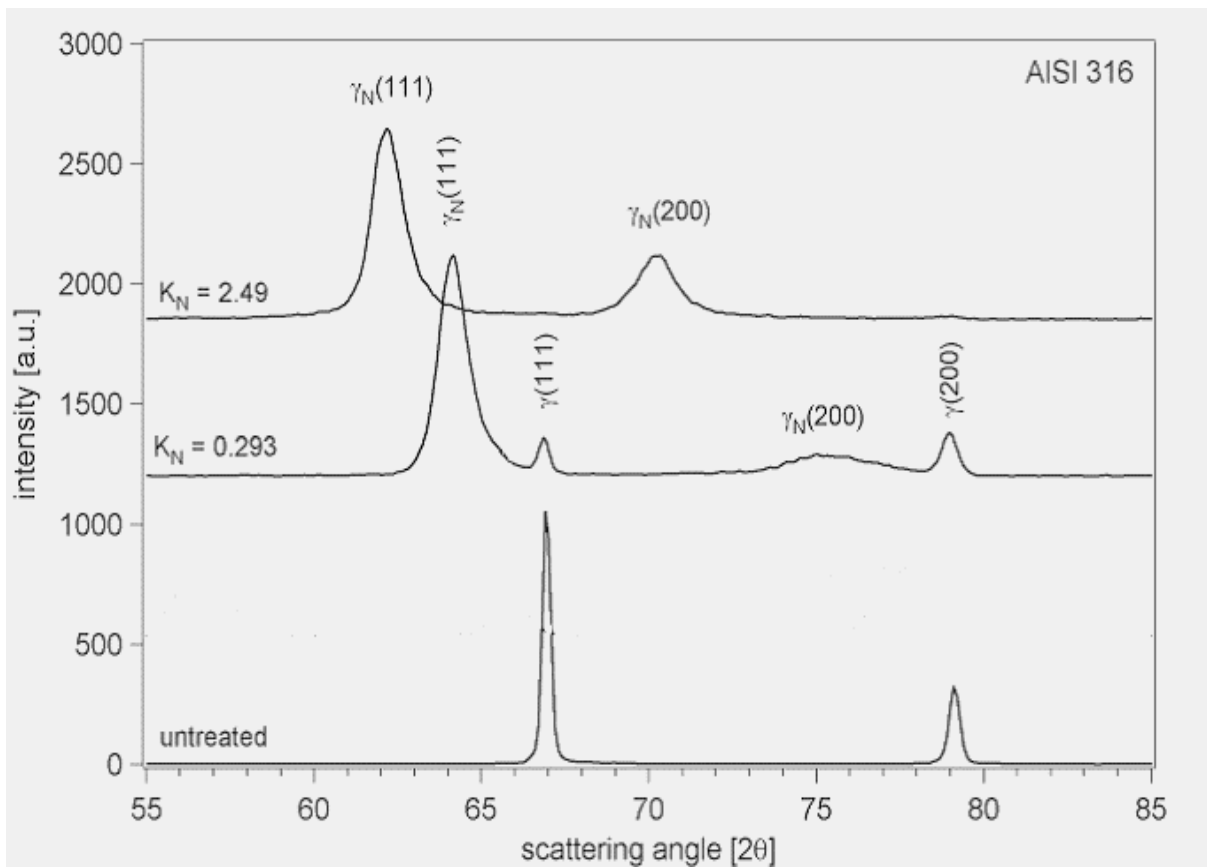


Figure 2.2 XRD patterns showing broadening peaks for an untreated film and nitrided films deposited at 445C.  $\gamma_N$  which is known as expanded austenite or the S-phase for nitrided films for (111) and (200) reflections are shifted to lower angles[52]

### 2.2.2.2 Anomalous Diffraction Observations in the S-phase

Saker et al. [30] reported that the increase in the lattice spacing of the (200) crystal plane was greater than of the (111), (220), (311) or (222) planes. Also, they proposed that because of the nitrogen in the films the S-phase acquires an fcc structure with an expanded lattice parameter (this result is commonly observed in either by plasma immersion ion implantation (PI<sup>3</sup>) or reactive magnetron sputtering). For a cubic structure, the calculated lattice constant,  $a_{hkl}$ , should be independent of the (hkl) used in its calculation and is given by equation (2) [49]:

$$a_{hkl} = d_{hkl} \sqrt{h^2 + k^2 + l^2} \quad (2)$$

where  $a_0$  is the lattice parameter based on the given Miller indices (hkl) and  $d_{hkl}$  is the interplanar spacing. However, the lattice constant (now written as  $a_{hkl}$ ) for the expanded austenite structure has been found to follow the relationship:

$$a_{200} > a_{111} = a_{220} = a_{311} \quad (3)$$

This anomaly in the lattice constant measurement has yet to be resolved.

### 2.2.3 S-Phase Formation within Surface Hardening

There are several methods and ways to form S-phase. The most common procedures are to diffuse or implant nitrogen into the S-phase surface hardening, which can be done through plasma immersion ion implantation (PI<sup>3</sup>) and conventional ion implantation (CI<sup>2</sup>). In addition, S-phase can be produced by sputtering, using reactive magnetron sputtering method.

### 2.2.3.1 S-phase Formation by Nitrogen Implantation or Diffusion

Stainless steels surface hardening can be performed by nitrogen diffusion and implantation. These techniques work well at temperature range from 250<sup>0</sup>C to 400C. The conventional ion implantation (CI<sup>2</sup>) method was used by Öztürk and Williamson [25] to implant nitrogen into AISI 304 Stainless steel films by using 80% nitrogen in a mixed Ar/N<sub>2</sub> atmosphere. In their study, the S-phase (they called it  $\gamma_N$ ) was produced with the anomalous shift in the (200) peak to lower angle in comparison with untreated substrates. In addition, the plasma immersion ion implantation (PI<sup>3</sup>) was used by Samandi et al. [34] to implant nitrogen into 316 stainless steel at substrate temperatures of 350C, 450C and 520C. They observed S-phase at films deposited at 350C and 450C. At these given temperatures the corrosion resistance was examined and showed that S-phase has a similar corrosion resistance in comparison with untreated substrates. Also, they examined the hardness of the S-phase and obtained hardness levels up to 2400HV. In contrast, CrN was formed at 520C, which degraded the corrosion resistance. Menthe et al. [26] achieve a maximum Knoop hardness (HK) levels of about 1400HK for S-phase at 450C which was five times higher than untreated steels. This was accomplished by treating 304L stainless steel in a mixed gas composition of N<sub>2</sub>/H<sub>2</sub> and applying a pulsed d.c. plasma.

### 2.2.3.2 S-phase Formation by Sputter Deposition

Reactive sputter deposition (reactive magnetron sputtering) [30,38,41-45] has been used since 1990 to form S-phase by depositing stainless steel nitrides. In addition, reactive sputter is a common technique that allows the production of different phases and amounts of nitrogen incorporation into the films by varying the sputtering gas mixture's nitrogen concentration.

Increasing the nitrogen/argon ratio in the plasma has been seen to strongly decrease the deposition rate and increase the nitrogen concentration in the coating [44]. Saker et al. [42] made films from AISI 310 stainless steel nitride by reactive magnetron sputtering. A nitrogen content of up to 42% was obtained and the S-phase was confirmed by x-ray diffraction. At a nitrogen concentration of 15%, a maximum hardness of nearly 1500 Kg/mm<sup>2</sup> was obtained. In addition, Kapaganthu and Sun [38,43] grew nitride films using a 316L stainless steel target in a high vacuum with a pressure of  $5 \cdot 10^{-3}$  Torr, in a mixed argon/nitrogen atmosphere. They studied how increasing the nitrogen from 0 to 75% in the gas composition affected the nitrogen content in resultant films. Furthermore, the S-phase was produced in their study, and the (200) reflection peaks of films that have nitrogen content between 35-45% shifted from their predicted position. As shown in Fig. 2.3, increasing the nitrogen fraction in the sputtering gas increased the nitrogen contents in the films and reached a 50% nitrogen:50% metals component (M) (where M are Fe, Cr, Ni, and Mo) at 50% of N<sub>2</sub> in the gas composition. This proposed the S-phase films had a zinc blende (ZnS)-type lattice structure. Moreover, they showed that raising the amount of nitrogen to more than 50% in the mixed gas led to a constant nitrogen content in the resultant films: for example, when they tried to increase the N<sub>2</sub> content in the gas to 75%, they still obtained 50% of nitrogen in the resultant films.

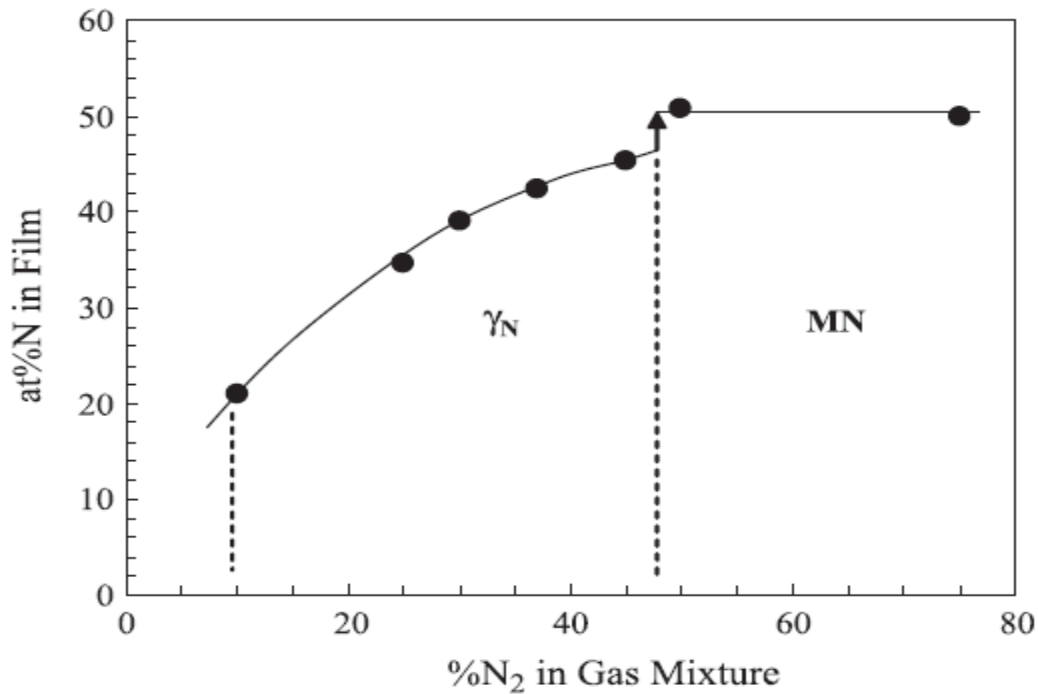


Figure 2.3: The nitrogen content in sputter-deposited films vs. the nitrogen composition in a mixed gas (after Kapaganthu and Sun [38,43])

Additionally, Shedden et al. [54] deposited coatings from 316 stainless steel using magnetron sputtering and a substrate temperature of 350°C. They found the nitrogen content in the films increased with the proportion of N<sub>2</sub> in the sputtering gas, and reached a maximum of about 40%.

#### 2.2.4 Theories on the structure of the S-phase

The S-phase is expected to have an fcc crystal structure with expanded lattice compared to the substrate. The first peak for an fcc structure is (111) and based on the position of this peak the (200) position can be calculated. The displacement of (200) from its expected position has led to research to try to understand how the structure of the S-phase is different than that of a normal

fcc lattice. These researchers have been trying to investigate its real structure since 1985. There are four main hypotheses explaining the displacement of the (200) peak. The four possible hypotheses for this diffraction anomaly are:

1. The S-phase has non-cubic structure;
2. There may be multiple phases present;
3. The anomaly may be due to the effect of stacking faults;
4. It could be the result of a large anisotropy in elastic constants.

These various hypotheses are examined more closely below.

### **2.2.3.1 Non-Cubic Structure or Possibility of Multiple Phases**

The S-phase might possess a non-cubic crystal structure, such as tetragonal, triclinic, or monoclinic. It has been proposed in past studies [50,52] that the (200) peak being at lower angles than expected (based on calculations of the (111) plane's position) could imply a tetragonal or monoclinic structure. Marchev et al. [50,52] proposed that S-phase (they called it m-phase in their study) had a body-centered tetragonal (bct) structure with lattice constants of  $a = 3.99\text{\AA}$  and  $c = 3.69$ , which makes  $c/a = 0.925$ . Based on their results, x-ray diffraction patterns in this situation should display split (200)/(002) peaks, but as shown in figure 2.4, no such splitting was observed. However, it was claimed the absence of this split might be related to the pronounced crystallographic texture in their films.

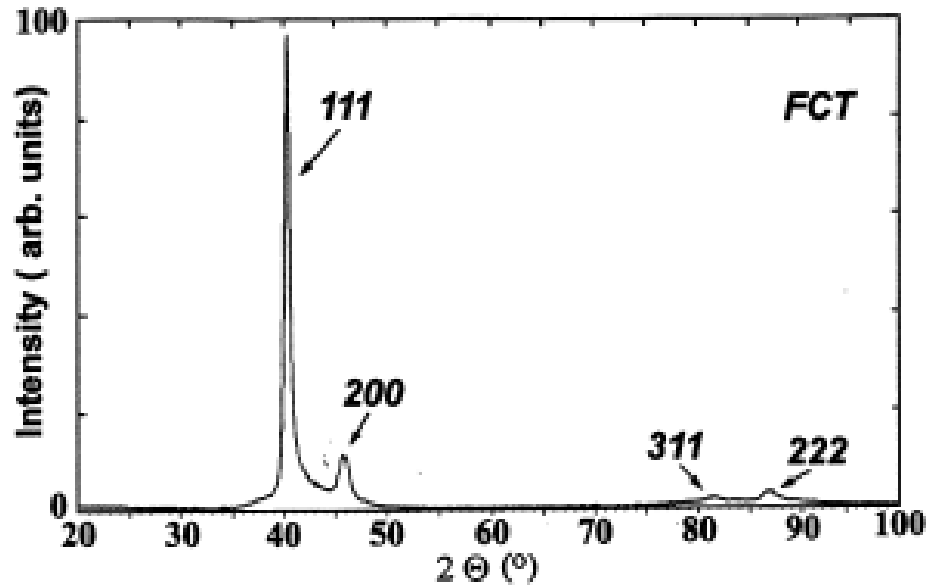


Figure 2.4 The XRD pattern of “m-phase” observed from a 316 stainless steel grade for film with a nitrogen content of 30 at. % [50].

To investigate the structure in more detail, Fewell et al. [49] carried out diffraction studies of stainless steel plasma-nitrided samples using synchrotron radiation, which allowed the S-phase to be studied at higher orders of diffraction, and permitting measurements of the d-spacings up to the (622) reflection. They suggested that the (200) reflection has a triclinic type structure even though they have failed to produce the expected (100) and (221) peaks with good matches. Also, they made several comparisons using other non-cubic crystal structures but their result failed to fit well with any of these structures.

Another explanation of the anomalous (200) peak is the possibility of multiple phases [25,27]. Fewell. et al. [49] also tested this hypothesis using the synchrotron radiation method and measured the d-spacing between lattice planes by changing the angle of the incident beam.

Their study did not find any extra phases, and this discredited the possibility of the multiple phases hypothesis.

### 2.2.2.3 Effect of Stacking faults and Residual stresses

Residual stresses are generally produced close to surface interfaces when modifying a sample's mechanical properties. The effects of residual stresses in S-phase layers have been discussed frequently. One particular experiment, performed by T. Christiansen and M. Somers [55], used x-ray analysis data to recreate residual stress profiles in 316L stainless targets applying a low processing temperature. They reported that large values of residual stress of about - 7.5GPa could be obtained for treated austenitic steel samples. These values were found when examining the sample with the (200) expanded austenite reflection. In addition, Grigull and Parascandola [31] found that increasing the nitrogen content in the nitride layer leads to an increase in the residual stress and a compressive stress of 2.5-3 GPa was obtained when the S-phase contained 23% N<sub>2</sub>.

In another study by Wanger [56], when a residual stress is produced in a film, the change in the lattice parameter  $\Delta a_{hkl}$  is given by the following equation

$$\Delta a_{hkl} = a_0 (S_1)_{hkl} \sigma \quad (4)$$

Where  $(S_1)_{hkl}$  is defined as an elastic constant for the hkl plane; their values for multiple reflections are given in Table 2. The variable  $\sigma$  is defined as the system's residual stress.

The values of the  $(S_1)_{hkl}$  for the expanded austenite are tabulated in Table 2.1. The shifting in the (111) and (200) peaks is a result of the presence of a compressive residual stress [55]. The

(200) peak shifted to more than two times higher  $2\theta$  angles in comparison to (111) plane. This is due to the fact that the elastic constant in (200) direction is greater than (111) direction.

Another explanation for the peak shifting from its predicted positions is due to the effect of stacking faults in the face-centered-cubic (fcc) lattices. Paterson [36] and Warren's [58] theories stated that if there is a presence of stacking faults with probability  $\alpha$  in a film ( $1/\alpha$  is the stacking fault spacing in terms of number of lattice planes), then the relationship between the changes in lattice parameter  $\Delta a_{hkl}$  and  $\alpha$  is given by equation (5):

$$\Delta a_{hkl} = a_0 G_{hkl} \alpha \quad (5)$$

Where  $G_{hkl}$  is an  $hkl$ -dependent constant as seen in table 2.1 [59]. Based on the parameters shown in Table 2.1 and because of the presence of stacking faults, the (111) peak position is shifted to a higher angle while (200) peak is shifted to lower angles.

$hkl$	$G_{hkl} \times 10^2$	$(S_1)_{hkl} \times 10^5 \text{ (kg/mm}^2\text{)}$
111	-3.45	-0.97
200	+6.89	-2.97
220	-3.45	-1.47
311	+1.25	-2.03
222	+1.73	-0.97
400	-3.45	-2.97

Table 2.1 The calculated values of stacking fault parameter  $G_{hkl}$  and elastic constant  $(S_1)_{hkl}$  for different reflections [59].

Other studies also reported that the anomalous (200) peak in the fcc structure is due to stacking faults on the (111) plane [60-63]. The stacking faults' effect on the peak positions was determined by Warren [48] and gave equation (6) in order to explain the peak shifting:

$$\Delta(2\theta)^{\circ} = \frac{90\sqrt{3}\alpha \tan \theta_{hkl}}{\pi^2} c_{hkl} \quad (6)$$

Where  $\alpha$  is the stacking fault density and is usually measured based on the change in the shifting angles  $\Delta(2\theta)$ , which is calculated from the (200) peak shift. In addition,  $c_{hkl}$  is constant, and its values are determined by Warren and have constant values of  $c_{111} = +1/4$ ,  $c_{200} = -1/2$ , and  $c_{400} = +1/4$ . The number of planes between stacking faults can be determined by  $1/\alpha$ .

Blawert et al. [60] used Warren's model to calculate the stacking fault density ( $\alpha$ ) for S-phase samples and found  $\alpha = 0.167$ . Also, Christiansen and Somers [61] found that when  $\alpha = 0.03$ , their results would fit their data. Another research [62] showed that  $\alpha$  relies on the nitrogen content and doesn't have a specific number as it varies with the nitrogen content. Recently, a study was given by Stroz and Psoda [63] used high-resolution transmission electron microscopy (HRTEM) to examine the stacking fault density  $\alpha$  of nitrided stainless steels samples independently of diffraction data. They found that stacking faults with a high density can be present in the expanded austenite phase with stacking fault density ( $\alpha$ ) value of  $\sim 0.1$ . Nonetheless, they proposed (200) reflection was shifted because the S-phase has a non-cubic structure (they suggested a rhombohedral structure).

## 2.5 Nitrogen Diffusion and Thermal Stability within S-Phase

When dealing with nitriding below 450C, precipitate-free interstitially supersaturated systems can be formed. The primary condition for this is having the interstitial diffusivity being significantly higher than substitutional element diffusivity. For the system of stainless steels, nitrogen is considered as an interstitial element while Cr, Fe and Ni are typically substitutional elements. Based on the presence of these elements, a precipitate free system should form because nitrogen has a diffusion coefficient that is significantly higher than chromium in the range of several orders of magnitude [64].

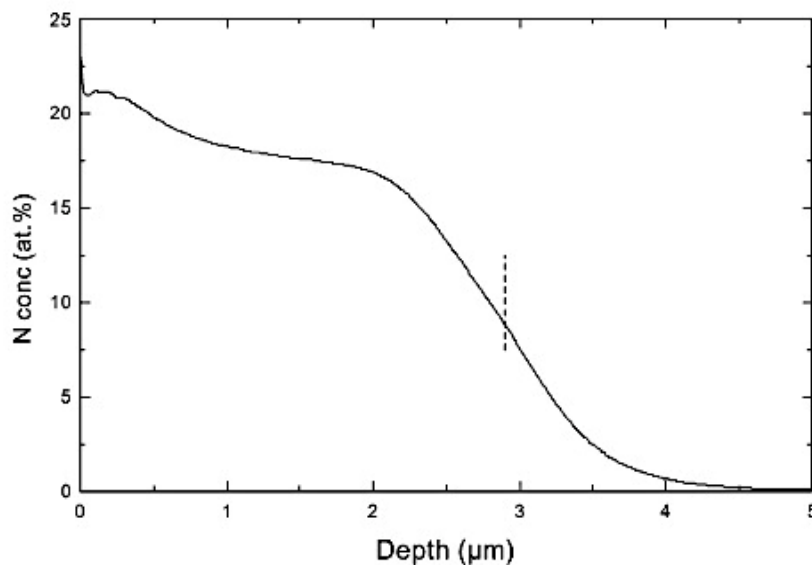


Figure 5 Figure 2.5 Shows an examining of a nitrogen profile as a function of a depth from a film deposited by ion implantation using a 321 stainless steel grade [64].

Examining a nitrogen profile, seen in Figure 2.5 [64], several regions can be seen with different characteristics. The first region portion, closest to the surface, shows a relatively fixed composition. This indicates that the region has a constant concentration of nitrogen. As the

sample is examined further from the surface, though, two more regions emerge. The first is a slowly decreasing nitrogen region, followed by a region with a very rapid nitrogen drop. An explanation for this behavior comes from two phenomena: an expanded austenite crystal structure and an octahedral site “trapping” mechanism [66]. The expanded austenite crystal structure is notable because it is characterized by a very high interstitial diffusion rate. It should be noted that, this is one reason why nitrogen can diffuse so quickly into a structure. This scenario creates a profile that tends to have a shallow diffusion profile. The second portion (i.e. – the rapid decline of nitrogen) in Figure 2.5 can be additionally explained by the ability of the crystal structure to trap interstitials. Researchers have hypothesized that chromium within the stainless steel creates octahedral “trap sites” that need to be filled with nitrogen before the nitrogen can continue diffusing through the system. This leads to a profile with a gradual decline in concentration as shown in figure 2.5.

From a mechanical perspective, one way to affect nitrogen diffusivity is to apply a tensile force on the system, expanding the crystals mechanically and helping diffusion occur. Similarly, high plastic deformation or other mechanisms that decrease grain size can also help to increase nitrogen diffusion through a system by increasing the number of low-energy diffusion paths [67].

Thermal stability within an expanded austenitic system is an essential matter because the treatment of the surfaces of the nitride/carbide stainless steels thermally might degrade the coatings previously made. Thermally speaking, decomposition of the S-phase results in chromium nitride (CrN) or chromium carbide (CrC) precipitation. Consequently, the good

corrosion resistance of the S-phase will be lost when the chromium nitride/carbide is precipitated, and this leads the Cr to be removed from the solid solution [38,43]. Furthermore, it has been observed that the S-phase relies on the nitriding/carbide progress where the temperature and the time are important. Chromium nitrides/carbides precipitate when the process temperature is above 400°C or when the time of the depositing films is too long [53]. Also, studies vary on the factors that allow this precipitation to occur. Li et al. [68] found that at 500°C for stainless steel nitride and at 650°C for stainless steel carbide, Cr precipitation could start happening under 1 hour. Bodycote discovered that the precipitation of Cr for materials modified with the Kolsterising treatment should not exceed 300°C [68- 70].

## 2.6 Tribology

Tribology is defined as the study of interacting surfaces as they move relative to each other. Typically classified as a branch of materials science and mechanical engineering, it studies and applies the principles of friction, lubrication, and wear [71].

Even though these principles are found in people's daily lives, they are not commonly taken into consideration when designing or engineering solutions. However, these principles are responsible for technical problems in modern society and their associated costs. This makes their use in design imperative to create lasting products and engineered solutions [72].

One major field within tribology is designing surfaces that slide or roll against each other while in the meantime the friction and wear is minimized. Reducing the friction and wear has many economical advantages where the life time of tools or methods will be longer. In addition, it

has benefits in environmental where reducing friction between machine components creates fewer heat-based energy losses, consuming less input energy [73].

Even though austenitic stainless steels are frequently used in many industries due to their good corrosion resistance, they are known to have poor friction and wear properties. When austenitic stainless steel comes into contact with other materials, they tend to wear out quickly. This is mostly due to strong adhesion junctions between the contacting surfaces and the resulting plastic deformation that occurs on the surface or subsurface of the parts. As a result, the iron, chromium and nickel which are the composition of the austenitic stainless steels will most likely fail due to mechanical wear instead of corrosion degradation. To combat this, the surface and subsurface of these components must be altered to undergo less mechanical wear while maintaining a high level of corrosion resistance. Attempts to do so have evolved over time, leading to the development of low temperature nitriding [74, 75]. In terms of sliding, friction force coefficients ranging between 0.5 and 0.7 have been found for a large set of conditions [76-78].

Given this summary of friction and wear mechanics, it is noted that austenitic stainless steels generally have poor tribological characteristics which limits its application in the many applications. Since this a major concern in designing systems, the steels must be modified to improve these mechanical properties while retaining their good corrosion resistance [79].

## 2.7 Thin Film Growth

Thin film deposition can be defined as the transportation of a material into gas phase either by physical vapor deposition (PVD) or chemical vapor deposition (CVD) methods. This material during this gas phase will then be transported towards a substrate in order to form a thin film.

In general, there are two types of deposition techniques. Firstly, physical vapor deposition (PVD), which is a large group of techniques that are used to synthesize thin films in vacuum conditions where high vacuum conditions are required in the deposition system to minimize the incorporation of large impurity concentrations [80]. Examples of PVD methods include thermal evaporation, cathode arc deposition, pulsed laser deposition (PLD) and reactive sputtering deposition [81]. Generally, in these techniques, the material is vaporized by bombardment of the target with ions, electrons or photons. The second kind of deposition techniques is chemical vapor deposition (CVD). In CVD when the chemical reactions are applied, the vapor will be produced and the thin film will be formed [81].

In addition, the concept of the mean free path (MFP) is important in the deposition process.

Here, the mean free path is defined as the average distance that a particle, molecule, or other atomic structure travels between collisions with other molecules.

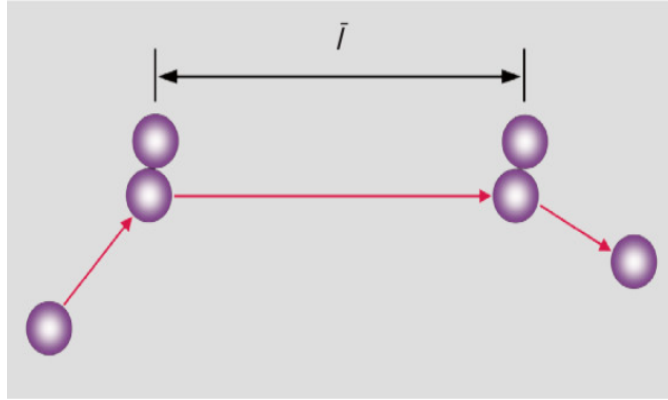


Figure 6 Figure 2.6 Shows the mean free path between two collisions

The mean free path is given by [70]

$$\lambda = 5 \times 10^{-5}/P \text{ (meter)} \quad (7)$$

Where  $\lambda$  is the mean free path and P is the pressure (m-torr).

In this thesis all films deposition were grown under a high-vacuum system (base pressure of  $10^{-6}$  Torr =  $1.3 \times 10^{-4}$  Pa) using reactive magnetron sputtering technique which, is a PVD process. The mean free path for all stainless steel coated films was typically 1 cm. A brief describing of this deposition technique is given in the following sections.

### 2.7.1 Sputter Deposition Basic Principle

Sputtering can be described as a method where atoms are ejected from a target source onto a substrate, creating a thin film of atoms. This target source is also known as a sputtering target or a target. This material target includes elements that are expected to be deposited on the substrate. The sputtering process is started by creating a plasma [80]. This plasma is formed by producing the inert (argon) gas into a high vacuum chamber as well as by creating a voltage bias

between the anode (substrate) and the cathode (target). The target, which has a negative electric charge and performs as a negatively charged electrode (cathode), will be then mounted in a magnetron [79]. In Fig 2.7 [54], a schematic of sputter system is illustrated and shows that an electric discharge is formed by applying a high voltage within the plasma to the target. This applied voltage will ionize the gas in this plasma. The ionized gas will then impact the target with a high kinetic energy. Upon striking the target, some of the target atoms will be driven out from their original lattice sites, becoming high energy neutral atoms or clusters of neutral atoms. These atoms tend to travel towards the substrate, and due to their high energy, will create a thin film on the substrate's surface [80].

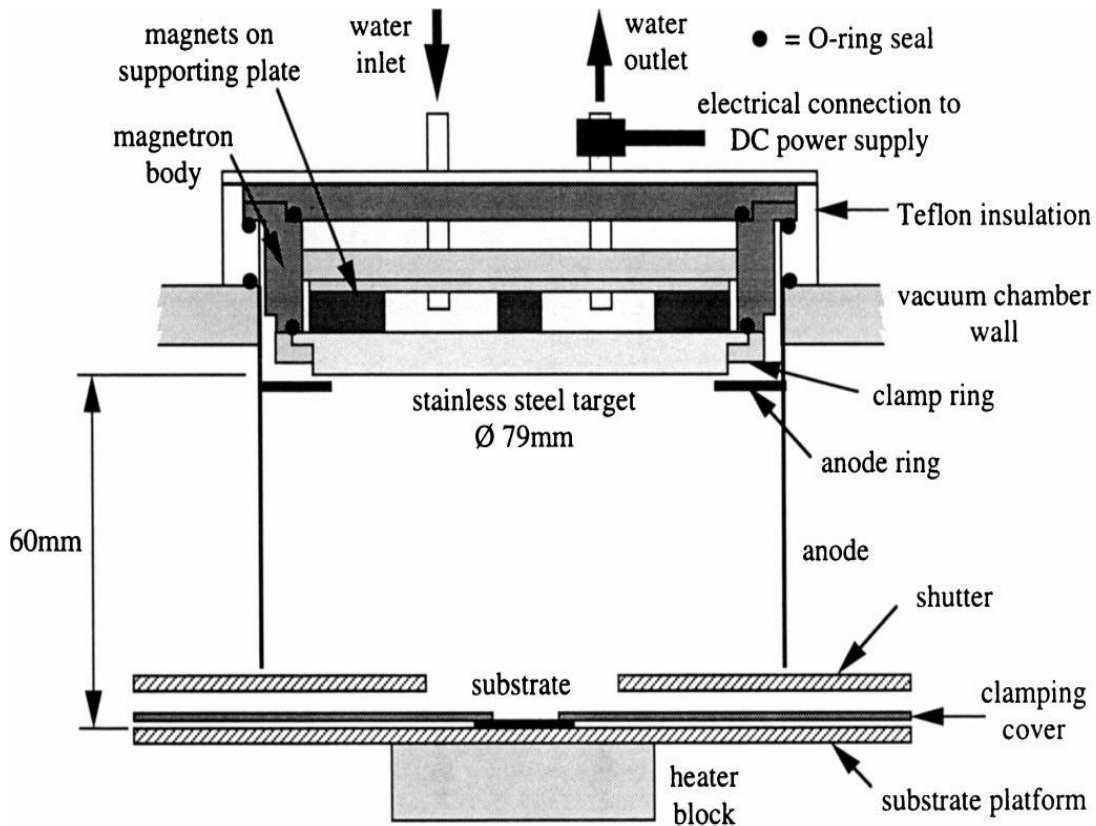


Figure 2.7 Shows a magnetron sputtering schematic [54]

### 2.7.2 Magnetron Sputtering

Magnetrons are widely used in the sputtering methods [80,82]. In the magnetron, behind the sputter target, magnets are placed as can be seen in Fig. 2.8a and 2.8b. The presence of the magnetron is important in the sputtering process because of the using of magnetic fields which help to confine ionizing electrons and to make the plasma facing the target. It does so by influencing electrons via the Lorentz Force where

$$\vec{F} = q * (\vec{E} + \vec{v} \times \vec{B}) \quad (8)$$

Where  $\vec{B}$  is the magnetic field,  $\vec{E}$  is the electric field,  $q$  is the charge and  $\vec{v}$  is the velocity.

Using a magnetic field to strongly modify the behavior of the electrons. The resulting force causes electrons to follow the magnetic field lines in oscillating, spiral-like paths when they are ejected in any path that is not parallel to the magnetic field. This creates an environment that helps to confine ionizing electrons using the magnetic field lines as a guide, keeping the electrons closer to the target surface. Since the electrons tend to follow these distinct paths, a higher ionization probability occurs in these regions, inducing more efficient sputtering and a higher rate of sputtering. This, in turn, creates erosion tracks on the target while making the deposition rate higher. As a result, magnetrons cause an improved overall sputtering rate and enhance the resulting film's properties by allowing the sputtering process to run at lower sputtering gas pressures.

The type of magnetron depends on the configuration of the magnets and the resulting fields. A balanced magnetron is one that has balanced magnets. However, this can create an environment that confines a plasma too strongly. To counteract this, some magnetrons have unbalanced magnets and fields [66]. Two configurations of an unbalanced magnetron exist. In Type I, the inner magnets are stronger while in Type II the outer magnets are stronger [83]. Figure 2.8b shows a Type II configuration where a “magnetic bottle” allows the plasma to reach out farther towards the substrate, improving transport phenomena and enhancing the growing film.

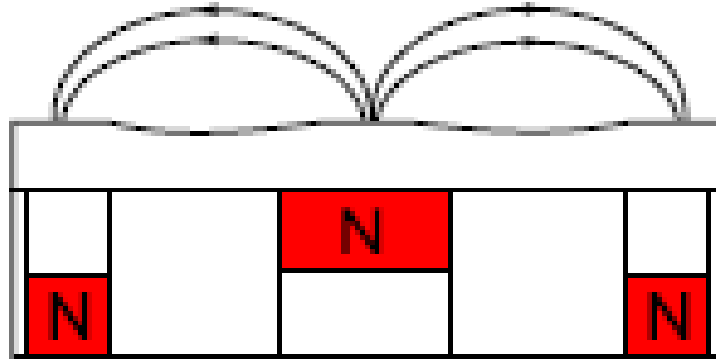


Figure 2.8a "Schematic drawing of a cross section of a balanced magnetron, displaying the magnetic field lines as closed loops above the target surface. Between the inner and outer magnetic rings the target displays an erosion track, or the so-called race track (taken from ref 83).

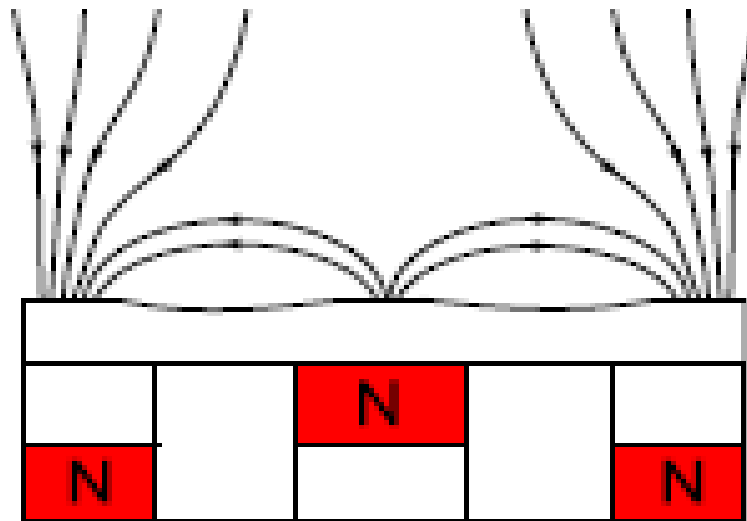


Figure 2.8b "Schematic drawing of a cross section of an unbalanced magnetron (type II), displaying the magnetic field lines as only partially closed loops above the target surface. Here, the electrons can more easily escape and travel towards the substrate region (taken from ref 83).

### 2.7.3 Gases Used during Sputtering Process

Argon is the most widely used gas for the sputtering process. This gas is commonly known as a noble gas and will not interact chemically with atoms that are sputtered. However, in some cases, if the distance between the substrate and the target is fairly short, argon atoms can become trapped within the substrate, affecting the substrate's morphology [80,84,85]. It should be noted that argon gas can be utilized with any sort of a source material. Besides argon, reactive gases, like nitrogen or oxygen, can also be used in a similar process called reactive magnetron sputtering. The difference here is that the reactive gases form compound materials, such as nitrides and oxides. In addition, the first researcher who used nitride as a reactive sputtering was Veysi [86], who in 1953 depositing tantalum nitride (TaN) as a thin film.

## Chapter 3: Experimental Procedures

### 3.1 Film Deposition

Thin films of stainless steel nitride (SSN), stainless steel titanium nitride (SS-Ti-N), stainless steel chromium nitride (SS-Cr-N), and stainless steel carbide (SSC) were fabricated at the University of New Hampshire using rf-magnetron sputtering. Commercial targets of AISI 304 stainless steel (with a composition of 8% Ni, 18% Cr, and 74% Fe), titanium, chromium, and carbon were used for deposition onto silicon wafers.

Fig. 3.1 shows an image of the reactive magnetron sputtering system that was used in this research. The depositions were performed in a high-vacuum system (base pressure of  $10^{-6}$  torr ( $1.3 \times 10^{-4}$  Pa)). This low pressure was always used in order to minimize the amount of impurities in the film. A turbo molecular pump was utilized to achieve high-vacuum conditions. In the system, two 50mm-diameter sputter guns were inserted in the top lid of the chamber are water cooled during deposition. The sputter guns are driven by RF-power supplies which helps to transfer the power to the sputter targets. The substrate holder which is placed inside chamber vacuum can be heated at temperature up to  $650^{\circ}\text{C}$  by connecting it with an AC power supply. To measure the resultant temperature, a thermocouple is inserted in the samples holder. Silicon (100) wafers were used as substrates in this thesis. They were first cleaned by alcohol and rinsed by ethanol. After that, a silver paint was pasted and stuck between a piece of a silicon substrate and the substrate holder and bonded by heating it at  $100^{\circ}\text{C}$ . The use of silver paint is common and provides a good thermal connection between the substrate holder and the Si substrate. To improve adhesion of the nitride films to the Si substrates, a metallic

stainless steel film was first deposited using only Ar and applied at a bias of -50V. The thickness of these bond layers were approximately 50nm for co-sputtered films (SS-Ti-N, SS-Cr-N and SSC) and 60nm for SSN films. Immediately following this deposition, desired nitrogen gas was added to the chamber (except for the SSC films for which Ar gas was the only gas used during the process). The ratio of argon and nitrogen gases was adjusted by mass flow controllers. The film thickness during deposition was monitored by a quartz crystal microbalance using a Sycon STM-100/MF device and later verified using SEM cross-sections.

A summary of the deposition parameters for chapters four to eight are given below:

#### **Chapter 4: SSN Films**

SSN films were deposited in a mixed Ar/N<sub>2</sub> gas, with the proportion of N<sub>2</sub> in the sputter gas varied by changing the Ar and N<sub>2</sub> flow rate. Three cases were used with the following gas flowrates (in sccm): 20Ar/5N<sub>2</sub>; 15Ar/10N<sub>2</sub>; and 12Ar/12N<sub>2</sub>. The total gas flow rate remained approximately constant at 25 sccm. All depositions with mixed Ar/N<sub>2</sub> were carried out at 150W. The target-to-substrate was 8cm. Deposition times of 2h were used, with a typical rate of 1 μm/h; several samples were deposited for 5 h to improve peak position measurements in XRD studies. The substrate temperature were varied between 150C-600C.

#### **Chapter 5: SS-Ti-N Films**

Deposition of the co-sputtered films from the stainless steel/ titanium targets were carried out in a mixed Ar + N<sub>2</sub> gas mixture with flowrates of 20 sccm Ar and 5 sccm N<sub>2</sub>. Four different sets of parameters were used for the for SS-Ti-N films. The substrate-to-target distance in the deposition of these films was approximately 9 cm. Different film compositions for the SS-Ti-N

films was obtained by varying the gun power ratios. A radio frequency (Rf) power supply was used to deliver 25-175 watt to each sputter target. During deposition, the substrate holder was held at a temperature ranging from room temperature to 450 °C.

### **Chapter 6: SSN/SS-Ti-N Films**

Several films were co-deposited using the stainless steel target as well as a titanium target. All nitride film depositions were carried out with 20 sccm Ar/ 5sccm N<sub>2</sub> gas flow and a target-to-substrate distance of 60 mm. The substrate temperature of the films were varied between 25C-350C and bias levels varied between -60V-140V. The films are designated as “S” for those deposited using only the stainless steel target and “S-Ti” from those co-deposited from stainless steel and titanium. Each film designation also shows the substrate temperature and bias, and additional designations are “L” for the lower-titanium level films, “H” for the higher titanium levels, “LR” for the lower rate film depositions.

### **Chapter 7: SS-Cr-N Films**

Numerous parameters were applied for SS-Cr-N coatings in the goal of studying the effect of applying different power, substrate temperature and levels of bias. Substrate temperature was varied between 25-350C and power ratio were 2:3, 1:1, 3:1 and 1:3. The bias levels were ranging from 100-160V.

### **Chapter 8: SSC Films**

Different film compositions for the SSC films were obtained by varying the power at various ratios. Mass flow controllers were used to set the flow rates of argon gas. A radio frequency (rf)

power supply was used to delivered 25-150 watt to the carbon sputter target. During deposition, the substrate holder was held at a temperature ranging from room temperature to 450 °C.



Figure 3.1: The reactive magnetron sputter deposition system used in this research.

## 3.2 Film Characterization

The microstructure and mechanical properties of the deposited films were characterized using a variety of methods after making these films by reactive magnetron sputtering. These methods include: X-ray diffraction (XRD), x-ray photoelectron spectroscopy (XPS), Scanning electron microscope (SEM), Transmission electron microscope (TEM), micro-hardness and pin-on-disk tests. These characterization methods are explained in more detail in the following sections:

### 3.2.1 X-ray Diffraction (XRD)

X-ray diffraction is a common phase identification analytical technique that is frequently used by materials scientists. In x-ray diffraction (XRD), diffracted beams are detected coming out from a structure that has had an incident beam fired into it. Based on the orientation of the sample and the distance between the sample's crystallographic planes, the intensity of the detected radiation will vary greatly [87]. **Figure 3.2** [88] shows an illustration that demonstrates the principle of the technique. In it, Bragg's law can be described as the path length difference of reflected atomic planes, which occur at an integer number of wavelengths and allow constructive interference of the reflected beams to occur.

As a result of the pathway difference between the atomic layers, defined as

$$n\lambda = 2d_{hkl} \sin\theta \quad (9)$$

Where  $\lambda$  is the x-ray wavelength,  $hkl$  are Miller indices defining the atomic plane and  $n$  is an integer.

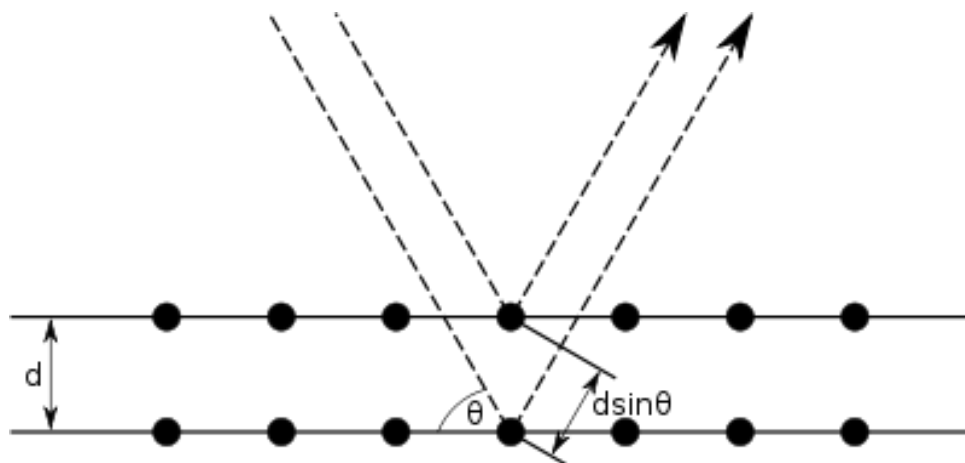


Figure 3.2 An illustration that demonstrates the principle of the X-ray diffraction technique

A maximum intensity will occur at an integral number of wavelengths. These intensities are then dependent on the structure factors and multiplicity of crystal planes. Certain crystal structures, which are smaller than 2 to 5 nanometers, may not be properly characterized by this technique, encountering peak broadening. These samples are known as being x-ray amorphous [89].

To quantify the peak shift in the FCC structure, as it will be seen in chapters 5 and 6 a term denoted the “R-value” was used, which for an FCC structure is given by:

$$R = \frac{\sin^2 \theta_{111}}{\sin^2 \theta_{200}} = 0.75 \quad (1)$$

In this thesis, the spectra of the resultant films were analyzed by a Shimadzu 6100 equipped with Cu K $\alpha$  radiation (the wavelength  $\lambda=1.5406 \text{ \AA}$ ) using PDF-2 database function of the Jade 9 (MDI, Inc) software program. Another XRD was also employed, a Bruker/ AXS general area detector diffraction system (GADDS), which employed Co K $\alpha$  tube ( $\lambda=1.79 \text{ \AA}$ ). These two XRD

analyses were done because substrate peaks sometimes overlap with film peaks; these two scans allow these overlapping peaks to be differentiated, allowing the distinct peak of the film to be characterized.

### **3.2.2 X-ray Photoelectron Spectroscopy (XPS)**

X-ray photoelectron spectroscopy (XPS) is a non-destructive and surface sensitive method that is used to measure and analyze the elemental composition of a material. XPS can provide a depth information of as low as approximately 10 nm [90]. One advantage of this equipment is it is capable of detecting all elements in the periodic table that have atomic numbers greater than 2, meaning it cannot detect Hydrogen (H) and Helium (He) elements.

The basic principle of operation of this equipment is that x-rays are used to eject electrons from the molecular shells. The kinetic energy of the photoelectrons which are emitted from the film surface are measured and the elemental composition on the surfaces of the films are determined from the elements that the electrons are dislodged from [90]. To calculate the binding energy ( $E_B$ ) for each individual element, equation (10) can be used

$$E_B = hv - E_K - \phi \quad (10)$$

Where  $hv$  is the x-ray photon energy,  $E_K$  is the kinetic energy for electrons and  $\phi$  is the work function which is dependent on the material.

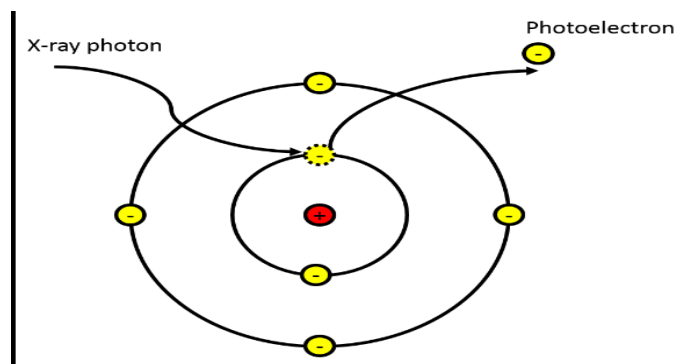


Figure 3.3: Principle of generating of a photoelectron in the XPS [91]

In the thesis the composition of the coatings was evaluated by x-ray photoelectron spectroscopy (XPS) to determine the atomic percentage of each element. The analysis was carried out on a Kratos AXIS-HS Analytical instrument using monochromatic Mg K $\alpha$  x-ray source operating at 15 kV and running at a current of 10 mA. A high vacuum of about  $10^{-8}$  Torr is needed to complete XPS process of analyzing the kinetic energy of the electrons. The accuracy in nitrogen concentration measurements is estimated to be  $\pm 2-4$  at. % N. To remove surface contaminants, a 4 keV Ar $^{+}$  ion beam was used to etch the surface before analysis.

### 3.2.3 Scanning electron microscope (SEM)

Scanning electron microscopy (SEM) is a technique that is extensively used in academia and in industry. This is because SEM gives a lot of valuable data and it is an easy equipment to be utilized. SEM additionally has a wide depth of field which helps the operator to control the microscope in an extensive magnification range, allowing captured images to have full focus even when dealing with very complex or contoured surfaces. An SEM works by generating collimated, focused electrons from a source (tungsten, LaB6, or field emission gun) and

rastering them over a surface. The electrons that backscatter off the surface, or secondary electrons (where secondary electrons are referred to as “secondary” because something else beforehand has knocked these electrons off the samples atoms) emitted by the surface atoms, are detected and ultimately processed into an image. To achieve high magnification and high resolution, a large electron mean free path is required, which necessitates high vacuum [92].

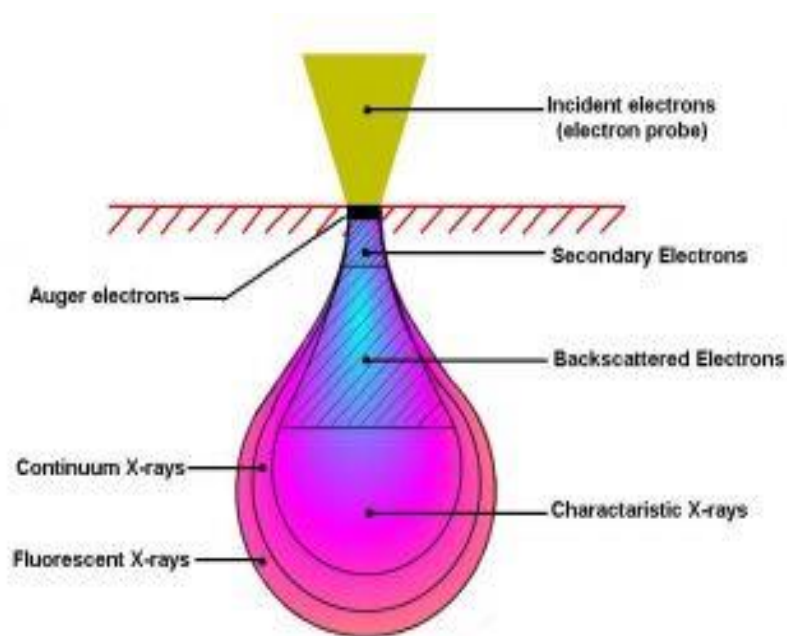


Figure 3.4: Electron beam-specimen interactions in the SEM [93].

In the thesis, the secondary electron was used for imaging the samples and the samples were prepared by cutting the cross-section of films using a specimen preparation tool called diamond saw. This tool helps to cut thin films by rotating a blade at a controlled speed. A cross-section is prepared by cutting both ends of the thin film and its substrate, but not all the way through. After making these notches, the thin film sample is then snapped off from the bulk by hand. After that, the films were examined with a Tescan Lyra FIB-SEM system operating at 6 KeV. It should be noted that surfaces of the films in this thesis were not coated with either gold or carbon before analysis using SEM technique.

### **3.2.4 Transmission electron microscope (TEM)**

TEM is a highly sophisticated technique used by scientists to study and characterize materials down for atomistic level. TEM can provide atomic resolution images of materials under defects [94].

In TEM electrons are accelerated (normally by 120KV potential) and by using the electrons lenses they are focused on the sample. When the electrons pass through the film, two states can be observed, a scattered or transmitted electrons. These two states again are focused and a visible image can be produced by projecting both images (see fig. 3.5).

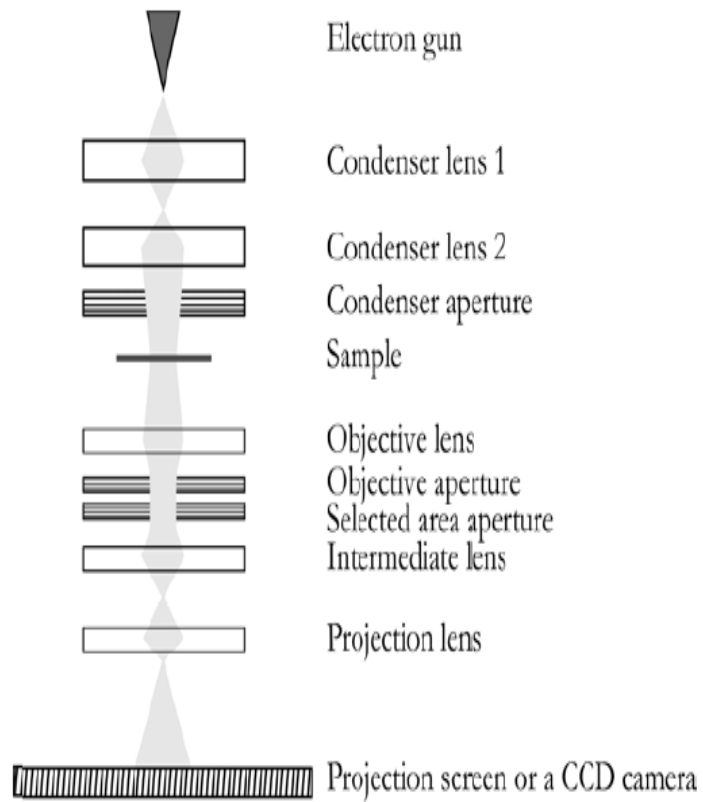


Figure 3.5: Transmission electron microscopy (TEM) schematic diagram [95].

In this thesis, TEM cross-section samples were prepared in the TESCAN instrument using the FIB attachment and a Ga<sup>+</sup> ion source. The samples were examined in a Zeiss LEO922 TEM operating at 120 kV.

### 3.2.5 Hardness:

Hardness is a property that used to assess the mechanical properties of materials. The hardness describes how a material can be able to resist indentation.

The hardness of the films was measured using micro-indentation equipped with a Knoop indenter (Fig. 3.6). Micro-hardness testing is a method that allows evaluation of material's hardness on a microscopic length scale. Various loads, from grams to a kilogram, can be applied to a precision diamond indenter, pushing it into the coated film at different locations [96].

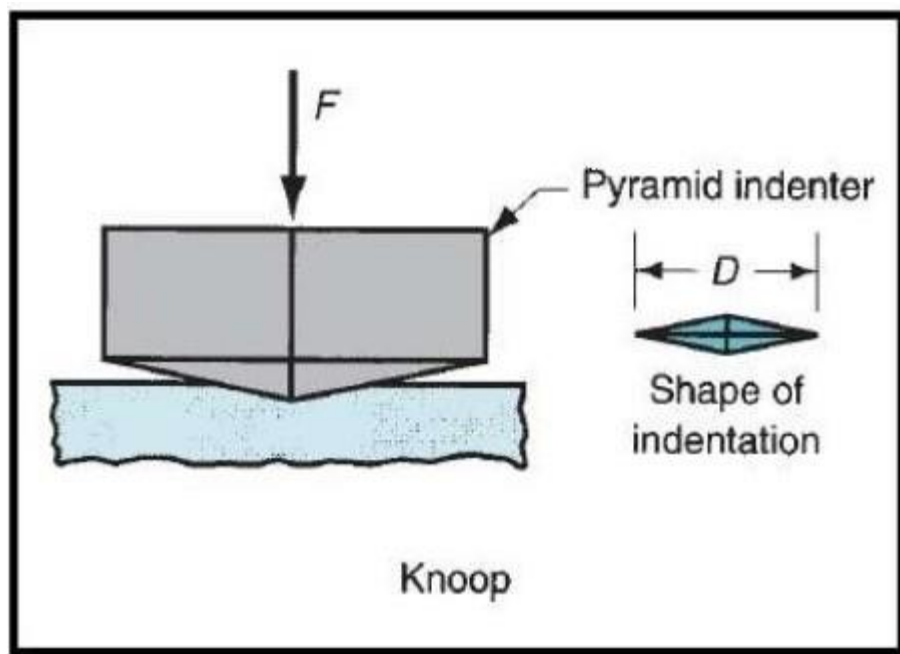


Figure 3.6: Schematic of the Knoop indenter and the indentation shape [97].

In this thesis, hardness testing was carried out using a 10-gram load, and each film was measured ten times, and the average is reported. For each measurement, a dwell time of 15 seconds was applied. Then the indenter was removed from the surface after making a diamond shaped indentation. Generally, the hardness value is determined when a surface of the material is indented and a projected area is acquired from the longer diametrical length of the indentation (d). The Knoop hardness (HK) is calculated using the following equation

$$HK = F/A = F/c \cdot d^2 = 14.23 \times F \text{ (Kg)} / d^2 \text{ (mm}^2\text{)} \quad (11)$$

Where F is the test load in Newton (N) and usually has a Kgf unit, A is the indentation projected area, c is a constant (=0.070279) and d is the longer diametrical length of the indentation.

The indentation depth is nearly 1/30 of the diametrical distance. To avoid the effect of a substrate on thin films, it is essential the depth of the indent should not overtake 10% of the film thickness [98,99].

In chapter 5, the hardness of the SS-Ti-N films was first measured using micro-indentation equipped with a Knoop indenter and a 10-gram load as tested in most of the coatings in this thesis. Due to the limited thickness of the films, these results were primarily used as a screening test to select films for further testing using nano-indentation. The nano-indentation tests were carried out on a Micro Materials NanoTest indentation testing platform (Micro Materials Ltd., Wrexham, UK) using a diamond Berkovich (3 sided pyramid) indenter. The indentation tests were performed by increasing the indentation force until the desired indentation depth (approximately 10% of the coating thickness, to avoid the substrate effect) was reached.

In general, for films with hardness levels near or above 1000 kg/mm<sup>2</sup>, the depth of indentation was ~15–20% of film thickness. Films which have lower hardness levels can possibly have substrate effects. However, higher indenter loads were used in some cases when the coated films had rough surfaces, and this could help to get better results. Micro-hardness tests provide information about how the bias, substrate temperature and film composition effect the relative film hardness.

### 3.2.6 Pin-On-Disk

A large number of methods are available to determine the tribological (friction and wear) properties of the coatings. In this thesis, the tribological behavior of the deposited films was measured using an equipment called pin on disk set-up [100] in an air at room temperature. The pin or a ball is pushed into a flat coated disk with a chosen load (100g was used as a chosen load for this thesis). The sliding track is formed on the films while it is rotating for thousands of cycles against the pin [96]. The materials in the ball or pin (in this thesis Aluminum Oxide (Al<sub>2</sub>O<sub>3</sub>) material was used) and the disk are easily changed and the load, sliding speed and diameter of the wear track can be adjusted to the desired value. During the test, the sliding force of the pin on the coated sample is measured, and the friction coefficient calculated continuously by dividing the sliding force by the normal force. Following this test, the wear track image of the coating is examined using an optical microscope. This is done to evaluate the wear patterns on the sample and to see if the coating has been worn off during the test.

The friction force is defined as

$$F_f = \mu_k N \quad (12)$$

Where F is the friction force,  $\mu_k$  is the friction coefficient, and N is the normal force

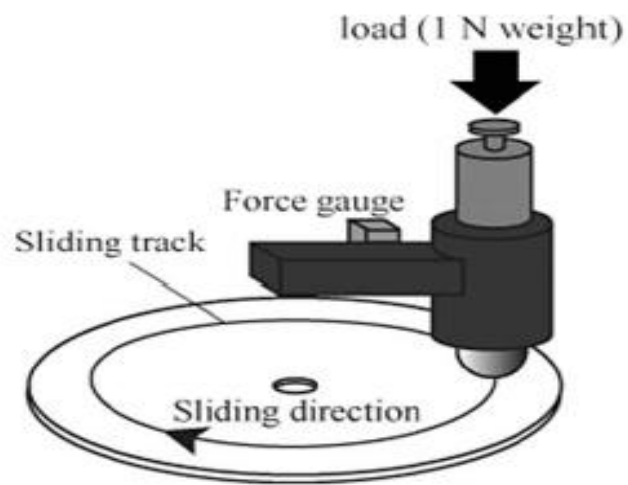


Figure 3.7: Pin-on-disk working principle [100].

## Chapter 4: Structure and morphology of stainless steel coatings sputter-deposited in a nitrogen/argon atmosphere [101]

While previous studies have been made using sputter-deposition to create N-supersaturated stainless steel films [21,25,33,39,42-45-49], a comprehensive study examining both the structure and mechanical properties of the deposited film has not been reported. Therefore, this research program began by examining magnetron-sputter deposited films using 304 stainless steel targets with deposition carried out in a mixed Ar/N<sub>2</sub> gas. The deposition variables included the substrate bias and temperature as well as nitrogen concentration.

### 4.1 Film Composition Analysis

Films were deposited under a wide variety of deposition conditions and substrate temperatures as shown in Table 4.1. The results of the composition analysis by XPS for are also shown in Table 4.1. The relative concentrations of Fe, Cr and Ni should correspond closely with the nominal composition of 304 stainless steel. To test this, the Cr/Fe and Ni/Fe ratios were calculated as shown in Table 4.1. The average Cr/Fe ratio was 0.28, while for Ni/Fe the ratio was 0.11. These values correspond well with the nominal values of 0.26 for Cr/Fe and 0.10 for Ni/Fe. The oxygen content of the films is also shown, and in most cases the oxygen level was below the detection limit for the XPS (about 2%). In samples where oxygen was detected, the average concentration was 5.4%.

Temp., °C	At.% Fe	At. % Cr	At.% Ni	At.% N	At. % O	Cr/Fe	Ni/Fe	N/(Fe+Cr+Ni)
-100V Bias, 20 sccm Ar + 5 sccm N <sub>2</sub>								
25	42.04	11.07	3.55	42.51	ND	0.26	0.08	0.75
150	49.9	12	7.4	30.7	ND	0.24	0.15	0.44
250	48.3	12.6	5.8	33.3	ND	0.26	0.12	0.50
350	49.5	13	5.7	32.7	ND	0.26	0.12	0.48
450	50.3	13.6	7.1	28.9	ND	0.27	0.14	0.41
550	59.1	19.8	5.36	17.7	ND	0.34	0.09	0.21
-140V Bias, 20 sccm Ar + 5 sccm N <sub>2</sub>								
25	47.76	11.36	5.63	34.92	0.34	0.24	0.12	0.54
150	45.2	12.2	4.15	30.8	7.6	0.27	0.09	0.82
250	43.9	10.5	4.5	29.2	11.8	0.24	0.10	0.76
350	50.8	14.7	3.87	30.7	ND	0.29	0.08	0.58
450	46.2	13.0	5.8	34.6	0.55	0.28	0.12	0.54
-100V Bias, 15 sccm Ar + 10 sccm N <sub>2</sub>								
150	39	10.1	3.6	43	4.2	0.26	0.09	0.82
250	38.3	10.3	5.1	40.7	4.4	0.27	0.13	0.76
350	43.4	11.7	4.8	35	4.1	0.27	0.11	0.58
450	42.4	14.7	7.7	35.1	ND	0.35	0.18	0.54
-100V Bias, 12 sccm Ar + 12 sccm N <sub>2</sub>								
150	40.1	11	2.9	46	ND	0.27	0.07	0.82
250	40.1	12.2	3.9	42	1.7	0.30	0.10	0.76
350	41.2	11.3	4.5	37	5.4	0.27	0.11	0.58
450	45.4	11.8	5	33.6	4.3	0.26	0.11	0.54

Table 4.1: Composition Analysis of Deposited Films

ND= not detected

The nitrogen content of the film was measured as an absolute value as shown in Table 4.1 and then the ratio of nitrogen to metal (Fe + Cr + Ni) was calculated from these results. Fig. 4.1 shows the N/ Me ratio vs. substrate temperature for films deposited at various substrate bias levels and sputter gas compositions. The general trend observed here is for the nitrogen level to decrease as the substrate temperature increases, although the extent of this varies with deposition conditions. The samples deposited at  $-140$  V (20Ar/5N<sub>2</sub>) show the least overall impact of substrate temperature on nitrogen content. The corresponding samples deposited at  $-100$  V show a small decrease up to  $450$  °C, followed by a sharp decline. The effect of process gas composition is also shown, and it can be seen that at higher N<sub>2</sub> concentrations, 15Ar/10N<sub>2</sub> and 12Ar/12N<sub>2</sub>, the nitrogen levels in the films are general higher, but undergo a significant decline with substrate temperature. However, little difference is seen between these higher two gas concentrations in terms of nitrogen content in the films.

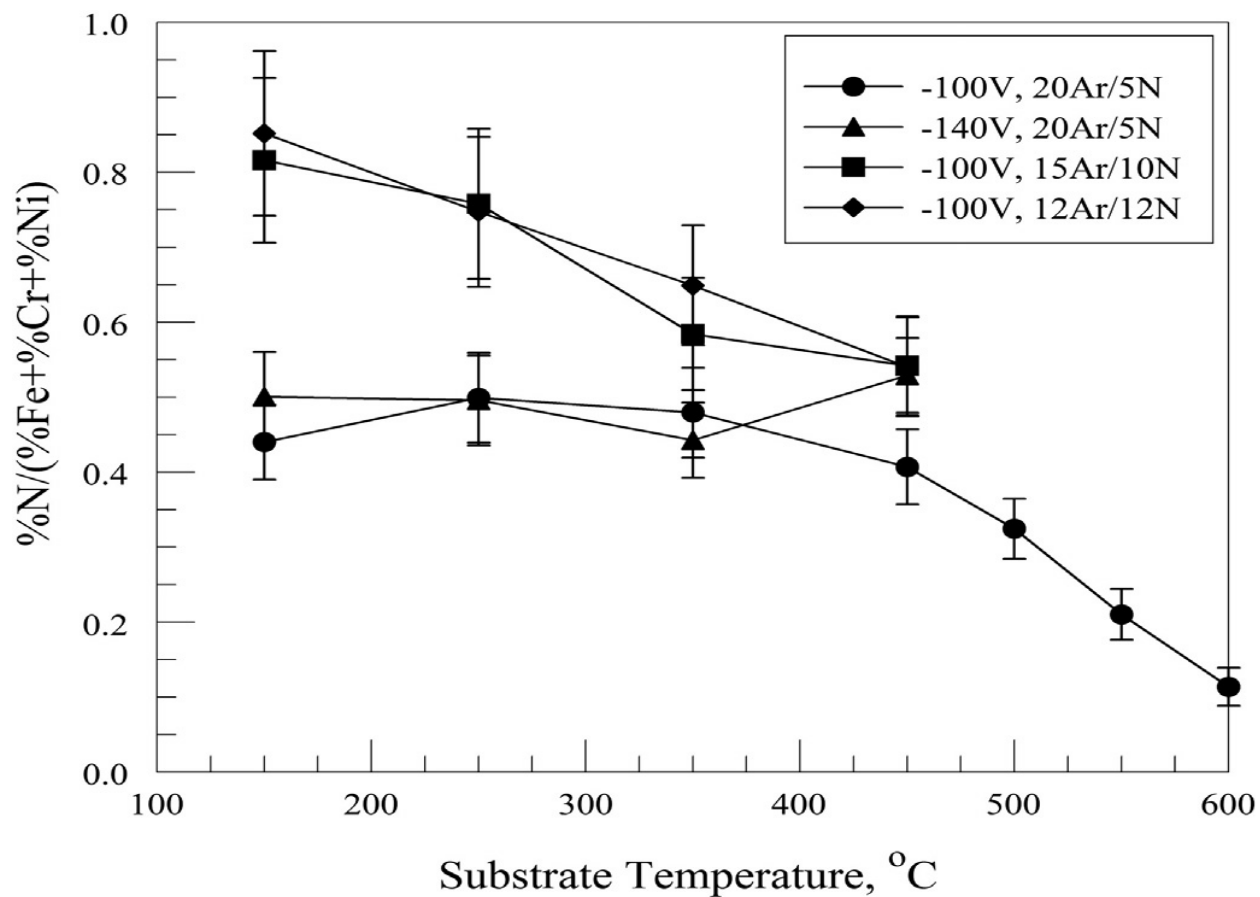


Figure. 4.1: The nitrogen/metal ratio vs. substrate temperature for films deposited at various substrate bias levels and sputter gas compositions. The ratio increases with fraction of N<sub>2</sub> in the sputtering gas, but decreases with increasing substrate temperature.

## 4.2 X-ray Diffraction

Fig. 4.2 shows the x-ray diffraction patterns for films deposited on Si substrates at -100V bias, 20Ar/5N<sub>2</sub>, with substrate temperatures ranging from 150-600°C. In addition, reference peak position patterns are shown for CrN,  $\gamma_N$  (S-phase), and bcc-Fe. The results show two general forms of x-ray patterns: one for samples ranging from 500-600°C and a second for 150-350°C, with the pattern at 450°C representing a transitional state. At higher temperatures, the patterns match well with the CrN and bcc-Fe reference patterns. In addition, the small peak near  $2\theta=52^\circ$  is close to the expected (200) reflection for Ni (note the (111) of Ni ( $44.6^\circ$ ) would be nearly coincident with the (110) bcc-Fe peak, at  $44.7^\circ$ ). Therefore, the films appear to have a multiphase structure containing CrN, bcc-Fe and a small amount of fcc-Ni.

Films within the lower temperature range are nominally consistent with an fcc diffraction pattern, showing (111), (200), (311) and (222) reflections, as expected within the scanned ranges. (The (220) cannot be observed due to Si substrate peak overlap). The reference  $\gamma_N$  pattern was calculated using a lattice parameter based on the position of the (111) peak. The corresponding (200) peak is shifted significantly from position that would be expected based on this calculation. This is a common observation for this phase, as discussed in the above. The position of the fcc-reflections within the films varies with deposition parameter, as shown in Fig. 4.3, which shows the lower  $2\theta$  range for four selected films as well as a detailed comparison of the (111) peaks. Increasing the bias to -140V resulted in a small increase in peak position, consistent with the small reduction in N content (as shown in Fig. 4.1) At higher N<sub>2</sub> gas levels (15Ar/10N<sub>2</sub> and

12Ar/12N<sub>2</sub>), the (111) peak positions are shifted to lower angles, also consistent with the higher nitrogen content in the films and an increase in the lattice constant.

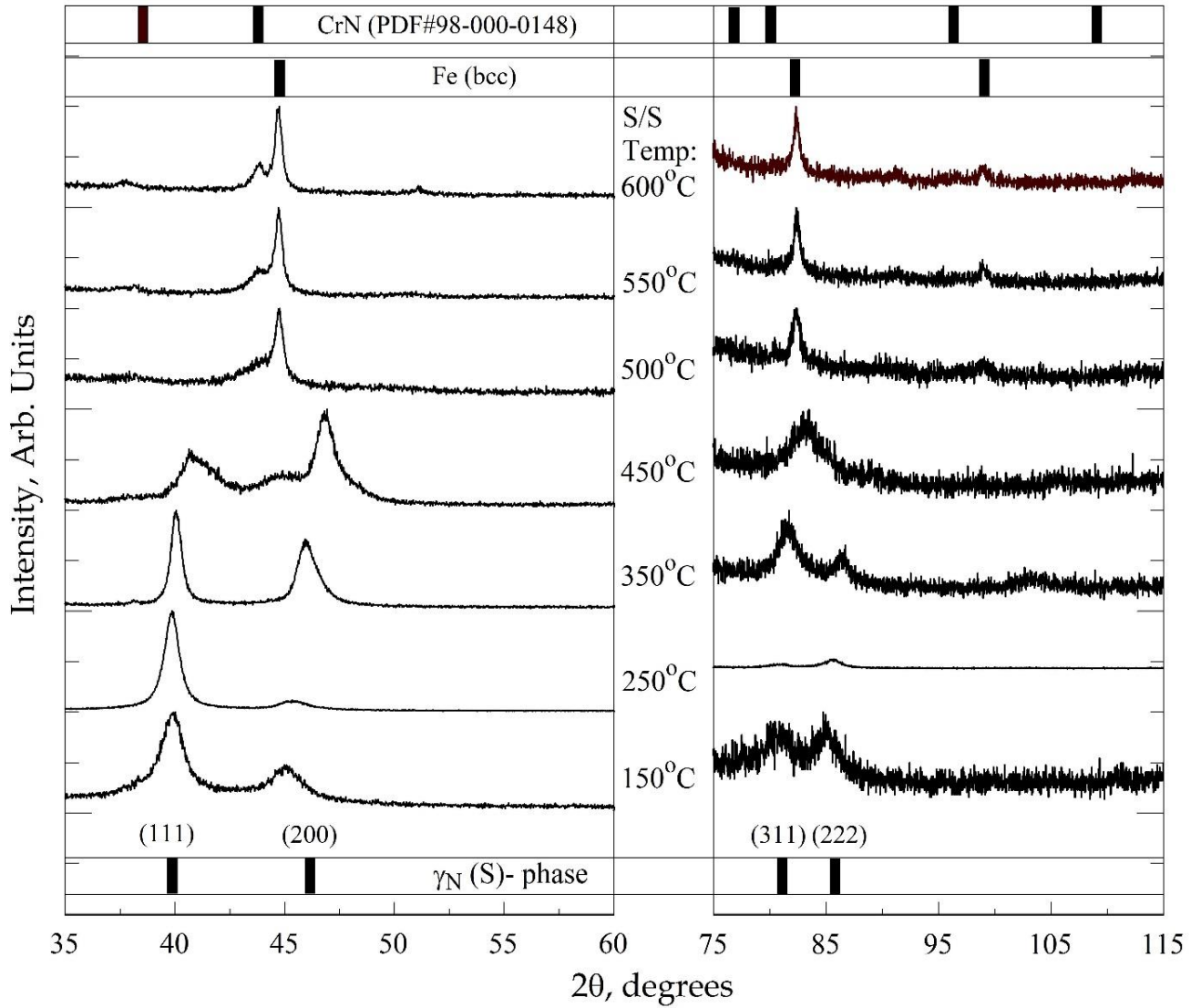


Figure 4.2: XRD results for films deposited at -100V and a range of substrate temperatures (indicated). Also shown are possible matches to known phases. The upper temperature range (500-600°C) matches CrN, bcc-Fe and Ni (see text), whereas below 450°C the structure is primarily S-phase

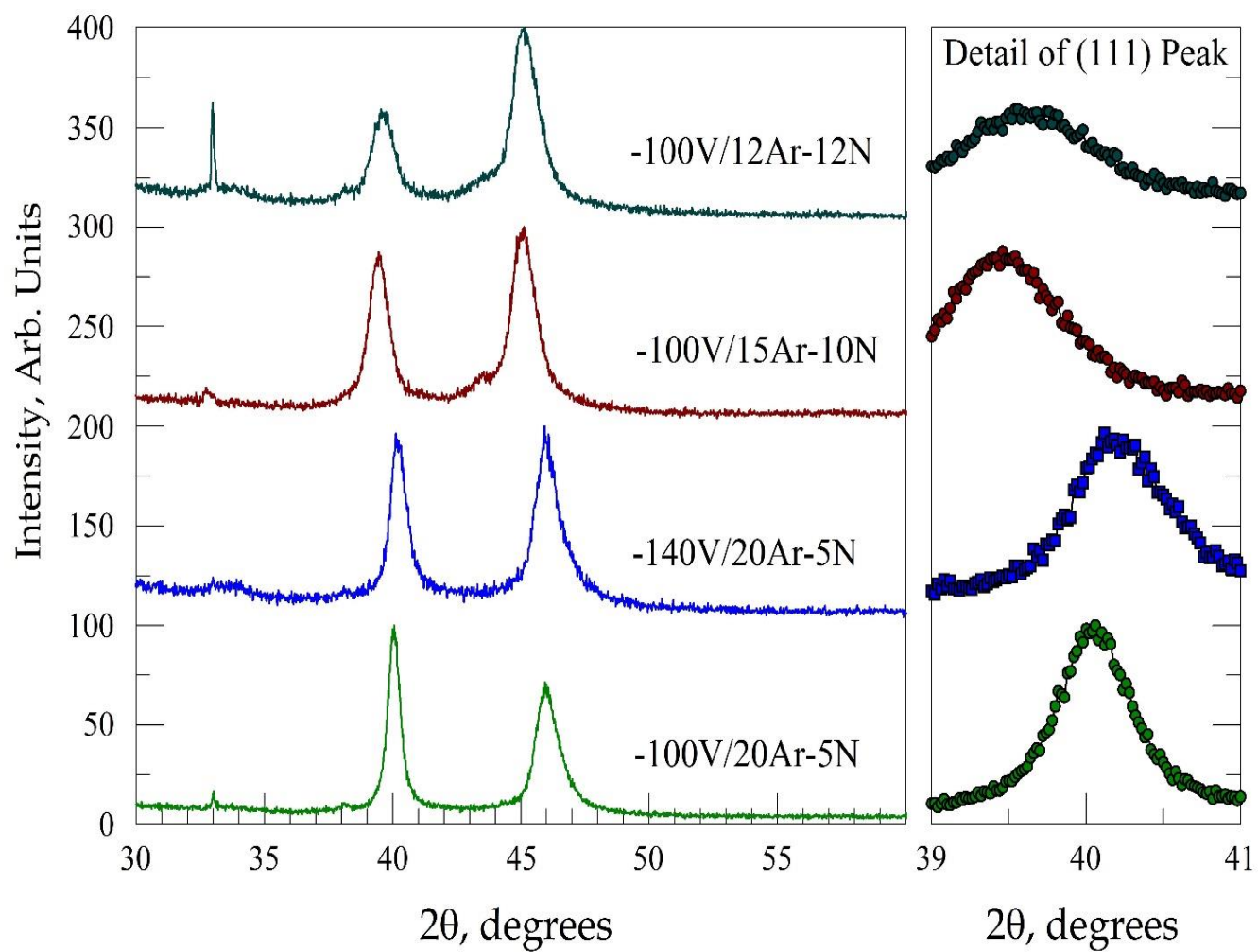


Figure 4.3: XRD scans for four selected films in the vicinity of the (111)/(200) peaks, with further detail of the (111) peak positions shown on the right. The substrate bias levels and gas flow rates are indicated for each scan.

In order to further examine the nature of the anomalous (200) peak position, several samples were examined in an x-ray diffraction system employing an area detector. This enables diffraction patterns to be acquired over a continuous range of  $\psi$  angles, where  $\psi$  is the angle of tilt of the diffraction vector off of the surface normal. An example of an area detector frame is shown in Fig. 4.4. As shown in the figure, a small segment of the Debye ring was selected and integrated to find peak positions. For the complete analysis, the Debye rings within each frame were divided into 10 segments, and the peak positions within each segment were determined by fitting the results with a Pseudo-Voigt peak fit model. The standard deviation for each peak fit was also calculated and is shown as well using error-bars on the plotted points, although in many cases the error bar range is smaller than the symbol size and hence is not visible. Along with examination of the sample of interest, a sample of pure Cu powder was run to verify detector alignment, particularly along the Debye ring. In order to minimize error in peak positions, a larger diffracting volume was desirable, and therefore additional samples, deposited at 200 and 300°C, were deposited to obtain ~5  $\mu\text{m}$  thick films. In general, the area detector scans showed the same peaks as diffractometer scans, i.e., no additional peaks were observed at any  $\psi$  values. This tends to discredit the concept of multiple phases or non-cubic structures.

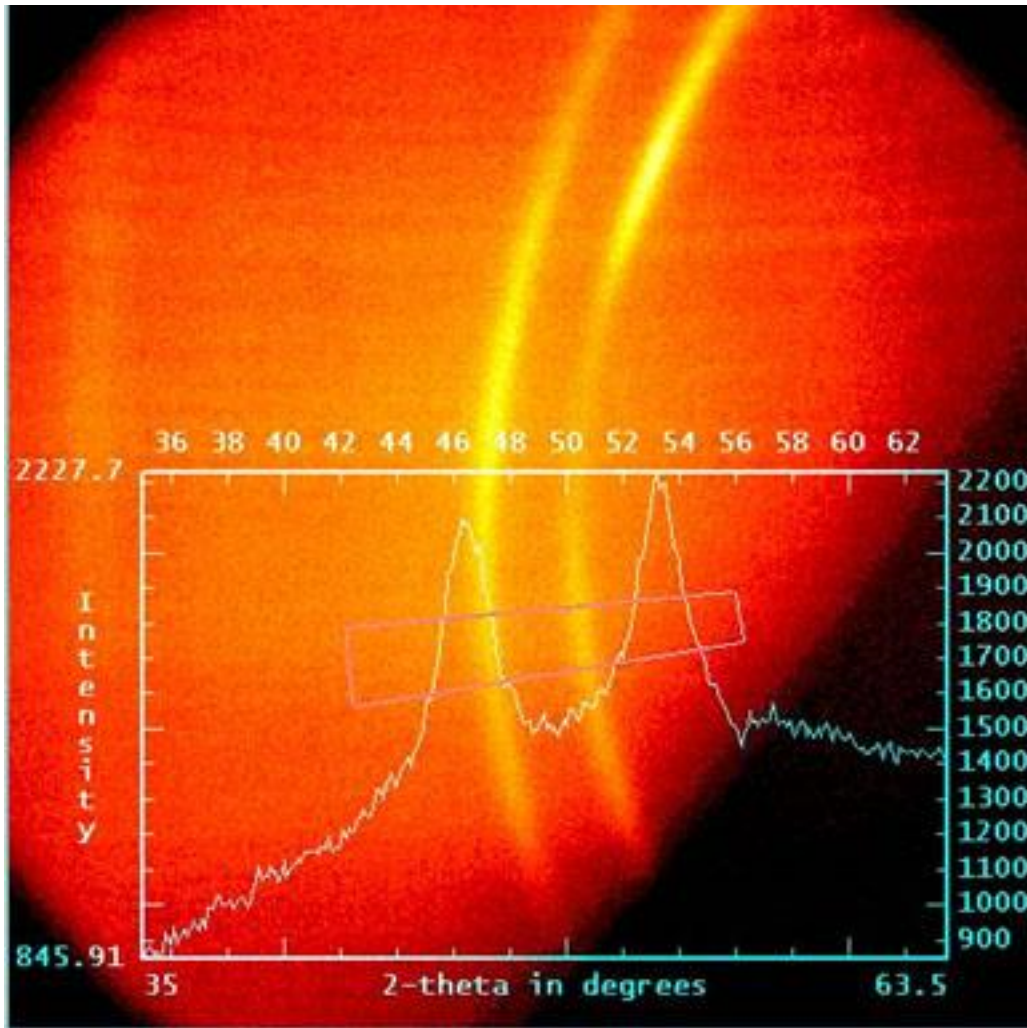


Figure 4.4: Example of an area-detector frame showing the (111)/(200) Debye rings, selected integration segment and integration results. Ten integrations were carried out along the Debye ring to obtain the lattice constant vs.  $\psi$  data shown in Figs. 4.5.

Fig. 4.5 shows the results for films deposited at 200 and 300°C, both with a bias of -100V and a 20Ar/5N<sub>2</sub> process gas composition. The nitrogen content of the films was again determined by XPS and the 200 °C film had a slightly higher measured percentage of 33.6% vs. 32.6% for the 300 °C film. The plot shows  $a_{hkl}$ , which is the value of the lattice constant calculated from the indicated (hkl) reflection, vs. the  $\psi$  angle. The lower plot shows a similar result for Cu (based on the (111) peak), and as expected the lattice parameter is constant and does not vary significantly with  $\psi$ . For the deposited films, for  $\psi$  near zero, the lattice constant based on the (200) reflection (denoted  $a_{200}$ ) is significantly larger than  $a_{111}$ . In addition, the peak position for (200) and hence the calculated  $a_{200}$ , as shown in the figure, is reduced as the  $\psi$  angle increases. However,  $a_{111}$  is relatively constant over the same range. At the lower substrate temperature, the difference between  $a_{200}$  and  $a_{111}$  increases, or, in other words, the anomalous nature of the (200) peak position becomes more pronounced. The minor difference in nitrogen content may explain slightly larger  $a_{111}$  values for the 200 °C (33.6% N) vs. 300 °C (32.6%) shown in the figure, but the differences in  $a_{200}$  values are more significant and must be due to other factors. Further analysis of the structural implications of this result is presented in the discussion section 4.4.

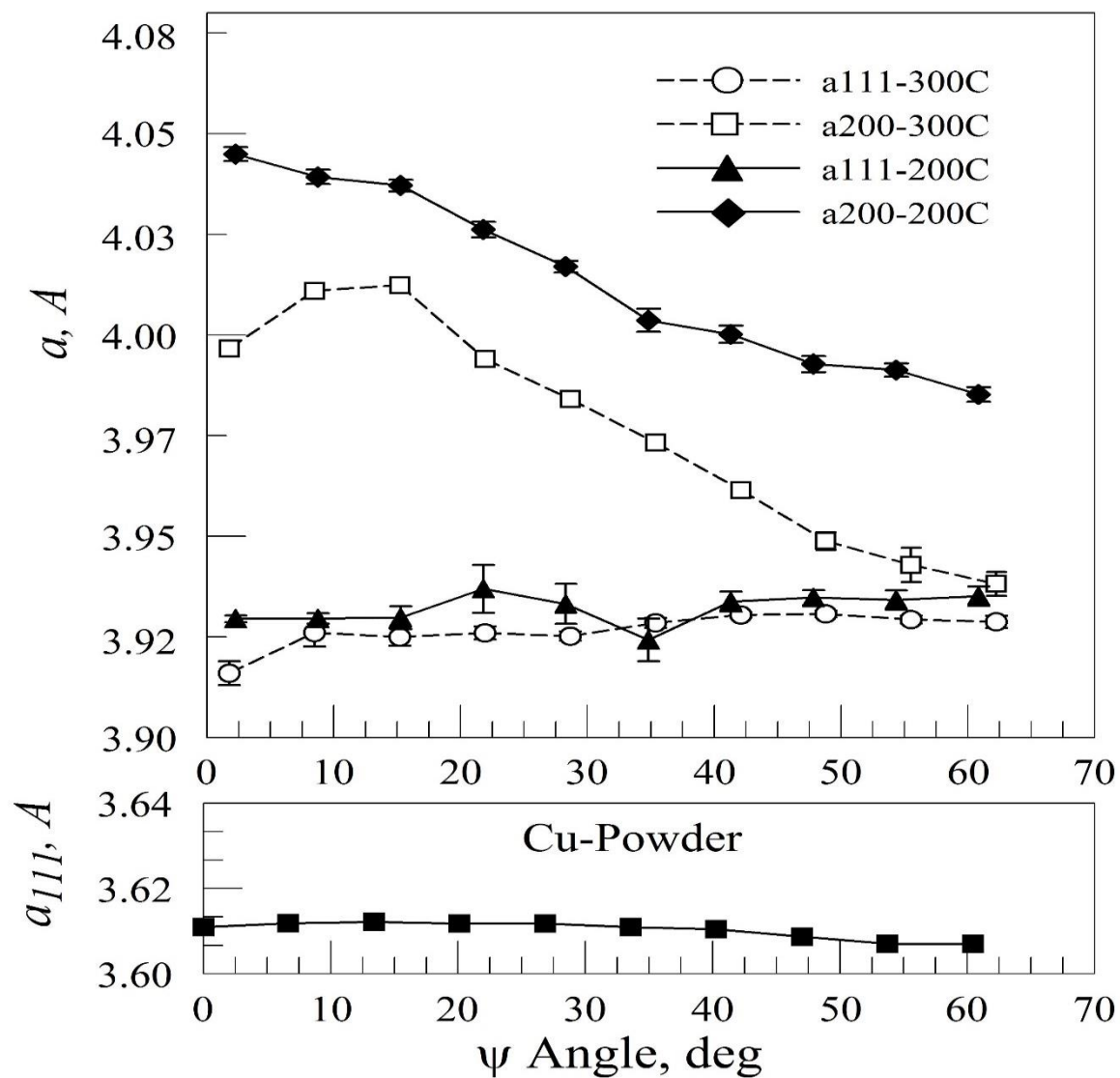


Figure 4.5: Measured lattice constants based on (111) and (200) peaks vs.  $\psi$  angle. The lower plot shows the results for a Cu powder standard indicating acceptable alignment over the range of  $\theta$  angles used. The upper plot shows  $a_{111}$  and  $a_{200}$  for films deposited at -100V, 20Ar/5N2 and 200 and 300oC. The decline in  $a_{200}$  with  $\psi$  is notable and contrasts with the relatively constant values for  $a_{111}$ . The peak positions were determined using a pseudo-Voigt peak-fit routine and the error bars represent the calculated variance in the peak position

The finding that the  $a_{200}$  values decline continuously with increasing  $\psi$  suggests a residual stress effect. However, the fact that  $a_{111}$  does not similarly decline and is not consistent with a residual stress effect. Nonetheless, an additional experiment was carried out where the sample deposited at 200°C was subsequently annealed at 400°C in air for 30 minutes. The intent of this experiment was to induce some stress relaxation and determine the effect of stress on the observed diffraction results. Fig. 4.6 shows the results in plot of the calculated  $a_{hkl}$  values vs.  $\psi$  angle. The slopes of the  $a_{200}$  and  $a_{111}$  curves remains largely unchanged, indicating that the sloping  $a_{200}$  curve is not a result of film stress. In addition, both curves appear at a lower position. This is likely due to the out-diffusion of nitrogen during annealing, which reduces the lattice constant. It should also be noted that a thin oxidized layer formed on the surface and was observed in the x-ray diffraction patterns as weakly diffracting Debye rings. However, the bulk of the film still consisted of the S-phase.

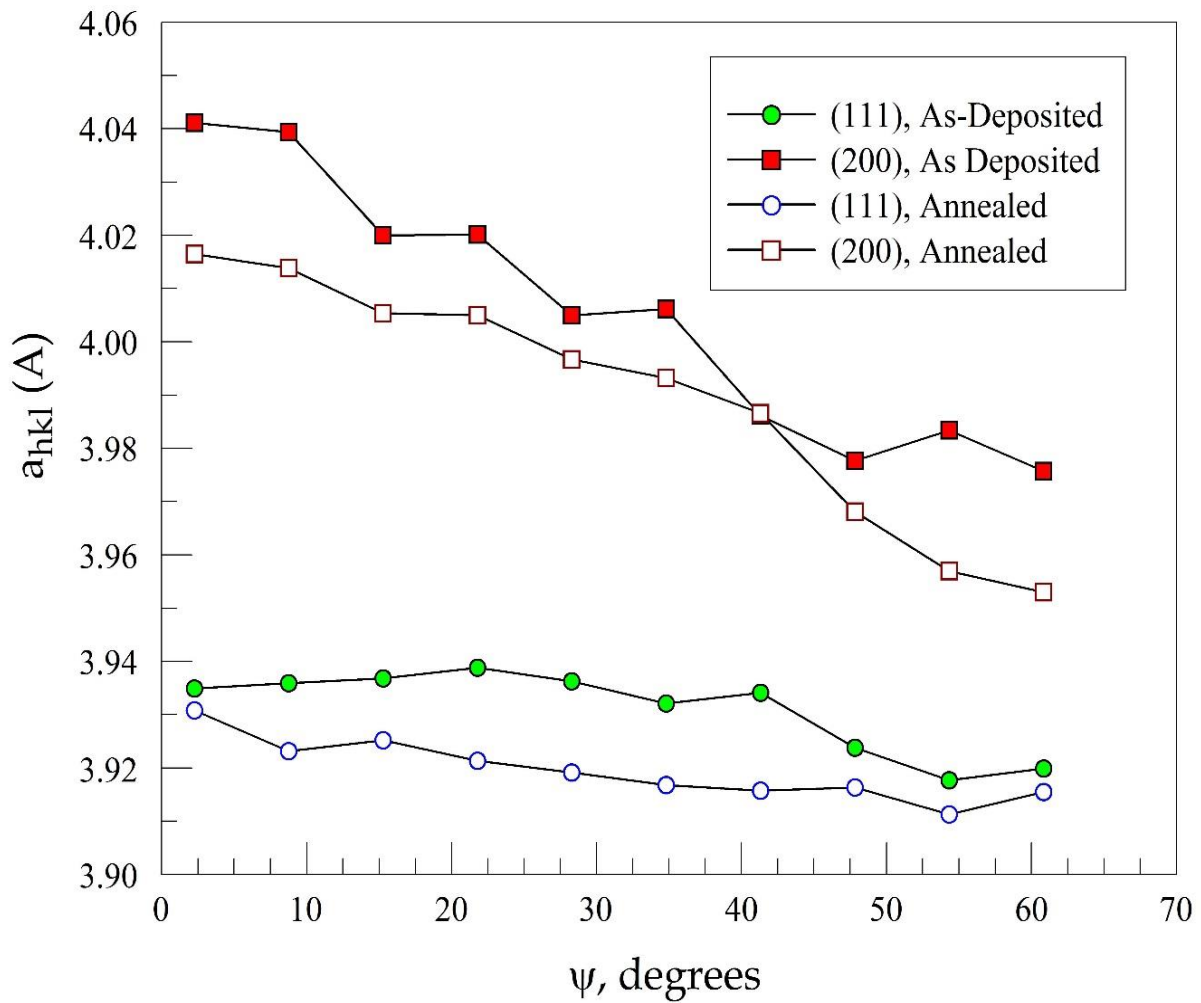


Figure 4.6: Measured lattice constants v.  $\psi$  for a film deposited at -100V, 20Ar/5N<sub>2</sub> and 200oC and then subsequently annealed at 400oC for 30 minutes. There is a slight reduction in lattice constant after annealing, possibly due to the out-diffusion of nitrogen

### 4.3 Film Morphology

SEM cross-section images are shown in Fig. 4.7 for several of the deposited films, showing the effects of temperature and bias for films deposited at 20Ar/5N<sub>2</sub>. Fig. 4.7(a) shows the film deposited at 250 °C, -100 V bias, where the structure can be described as generally columnar, but with a faceted and angular morphology with small wedge shaped grains. The surface also shows highly faceted features on top of the vertical columns. The resulting morphology would suggest a high degree of porosity within the film. Fig. 4.7(b) shows a film deposited at the same gas concentration and temperature but an increase of the bias to -140 V. This film shows somewhat coarser crystallites and larger voids, but more continuous columns. Fig. 4.7(c) shows the film substrate temperature to 350 °C. Here the columns are still coarser and surface roughness is also higher. Fig. 4.7(d) shows a film deposited at 500 °C and 20Ar/5N<sub>2</sub>/-100 V, revealing a nodular or particle-like morphology, which is very different from the morphology shown in the three previous images. However, it can be recalled from Fig. 4.2 that the phase content in the films changes at 450 °C, becoming a mixture of CrN, bcc-Fe and fcc-Ni above this temperature.

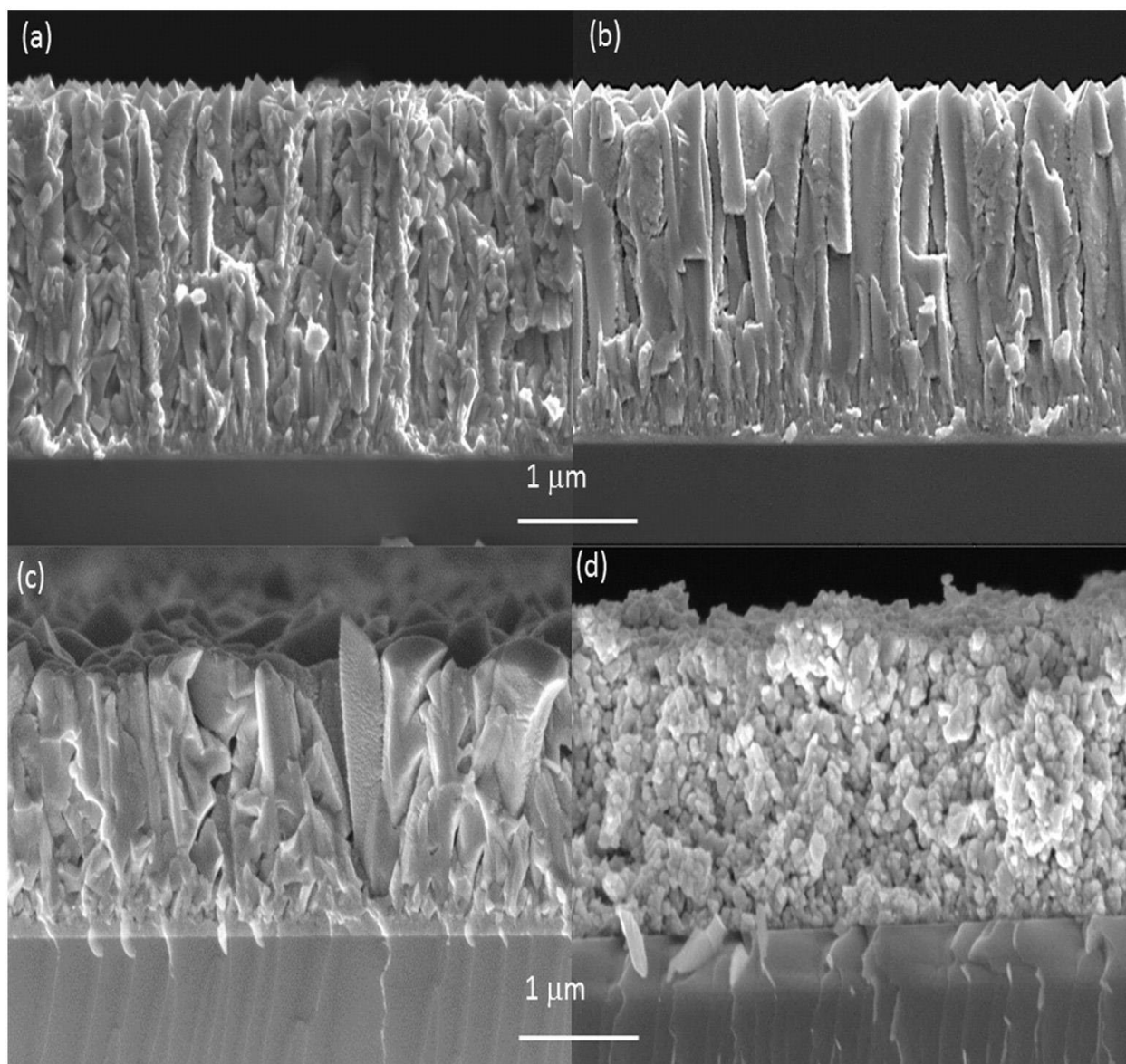


Figure 4.7: SEM cross-section images of selected films: (a) -100V, 250°C, 20Ar/5N<sub>2</sub>, (b) -140V, 450°C, 20Ar/5N<sub>2</sub>, (c) -100V, 500°C, 20Ar/5N<sub>2</sub>, (d) -140V, 250°C, 12Ar/12N<sub>2</sub>. Films (a), (b), and (d) show generally columnar structure with a faceted and angular morphology, while (c) shows a more powder-like morphology.

Fig. 4.8 shows a series of samples deposited at  $-100$  V bias and  $12\text{Ar}/12\text{N}_2$ . At  $150$  °C (Fig. 4.8a), a more typical columnar structure is shown and the columns are tilted, as is typically observed in off-axis deposition. In this case, the columns are less faceted than in Fig. 4.8(a) and (c) and as a result forms a smoother surface. It should also be noted that the N level in the film,  $\text{N}/\text{Me} = 0.85$ , which was the highest level achieved in this study. Depositing under similar conditions but at a higher temperature of  $350$  °C, Fig. 4.8(b) shows a return of some of the morphological features shown in Fig. 4.8(a)–(c), namely an increase in faceting and a coarse, angular structure. At  $450$  °C, (Fig. 4.8c), a nearly “worm-like” morphology is observed, but with the retention of significant faceting. A commonly observed feature in many of these films was the appearance of a layer-like morphology, as evidenced by a “ribbed” appearance in the columnar structures. Fig. 4.9(a) shows an SEM image of a film deposited at  $350$  °C,  $-100$  V and  $15\text{Ar}/10\text{N}_2$  where these microstructural features are indicated. Fig. 4.9(b) TEM image of the same film, showing a segmented or mosaic appearance within the coarse columns present in the film. This morphological feature is not common to thin-film structures and hence cannot be fully explained at this time. Recent research has shown the presence of a high density of stacking faults in S-phase samples as revealed by TEM studies [43].

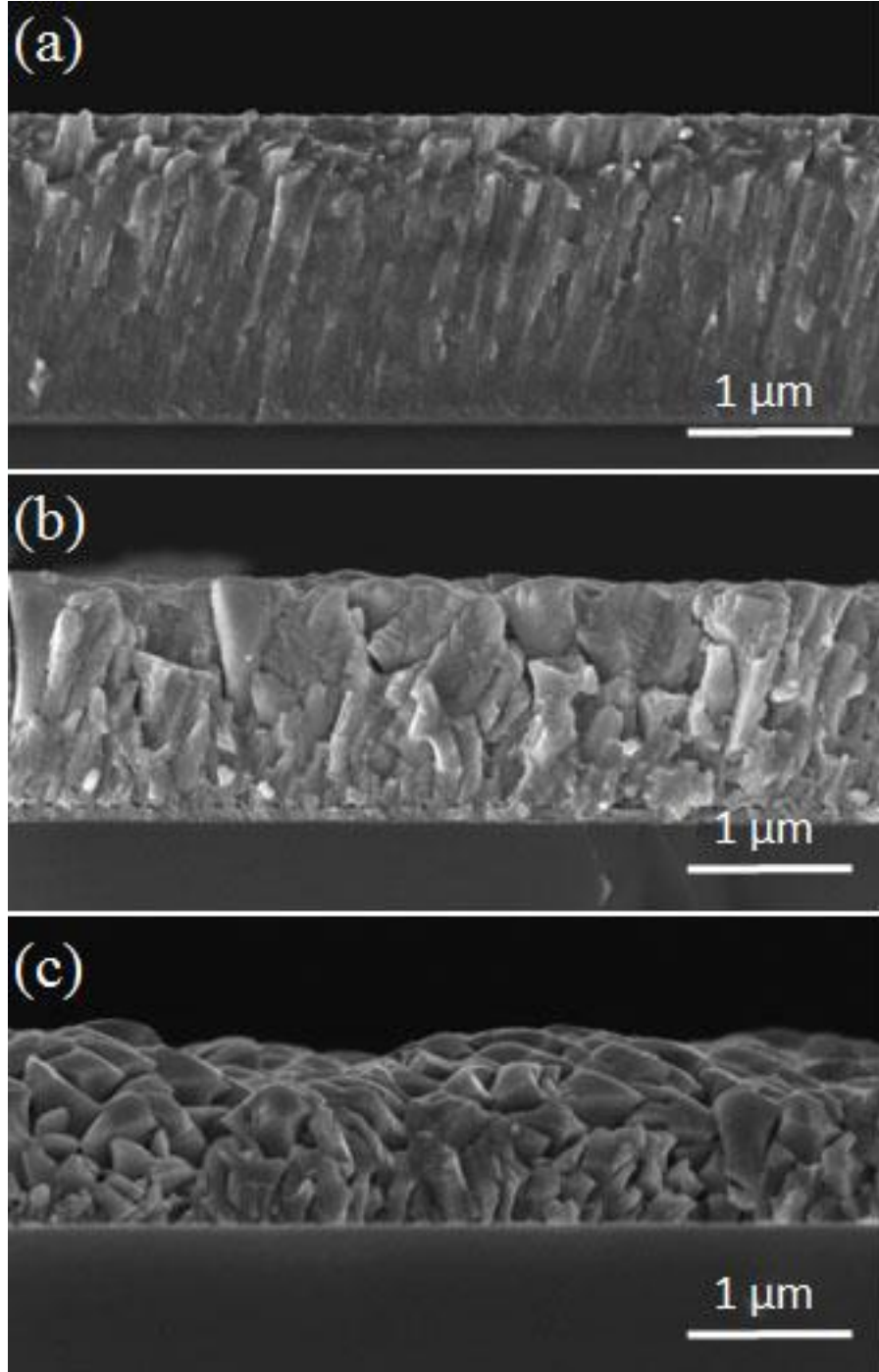


Figure 4.8: SEM cross-section images of selected films deposited at 12Ar/12N<sub>2</sub> and -100V at temperatures of (a) 150°C, (b) 350°C, and (c) 450°C. Film (a) shows a typical columnar morphology, but the structure becomes more faceted and discontinuous as the temperature increases

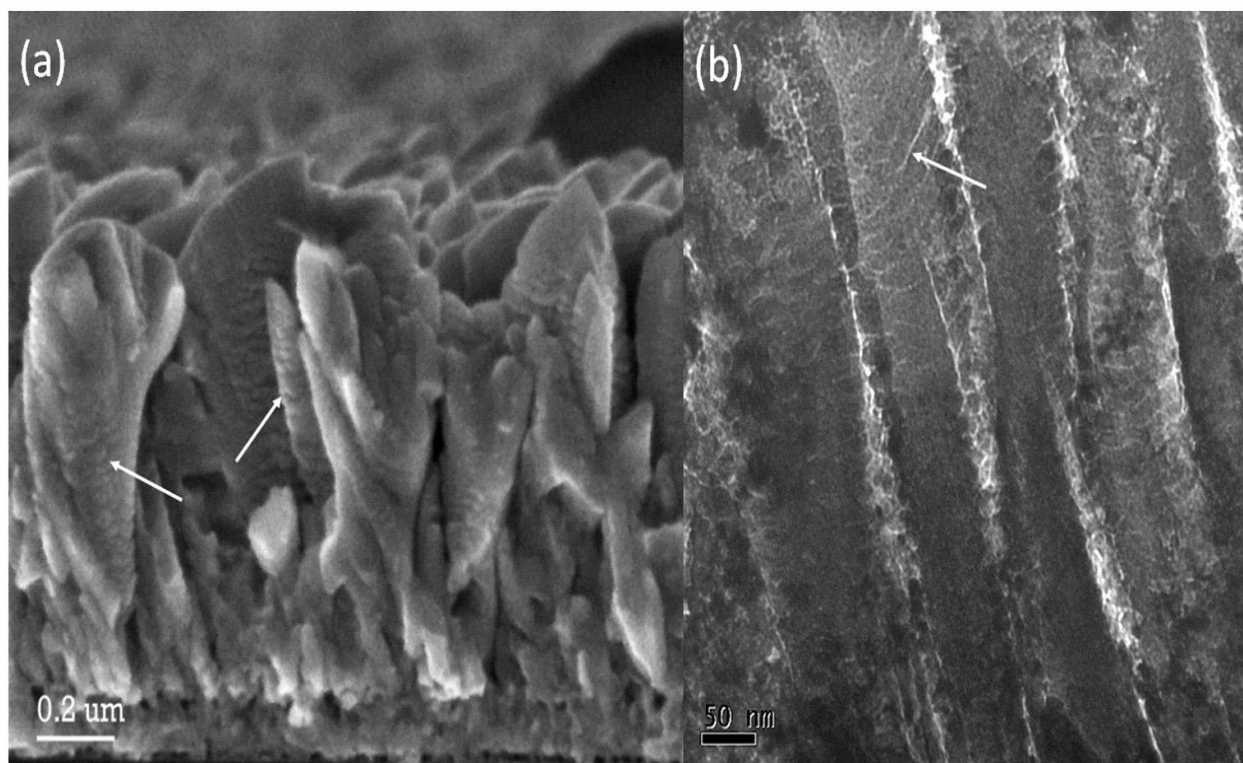


Figure 4.9: (a) SEM image a film deposited at 350 °C, -100 V and 15Ar/10N<sub>2</sub>, showing a layer-like morphology within the columns giving a “ribbed” appearance to the column edges. (b) TEM image of the same film, showing a segmented or mosaic appearance within the coarse columns present in the film.

#### 4.4 Mechanical Properties

Several of the deposited films were tested using the Knoop hardness method. Films deposited at 550°C and above had a very rough surface with a loose granular structure and were found to have very low hardness values ( $< 400 \text{ kg/mm}^2$ ). The remaining films were tested and the results are shown in Fig. 4.10. It can be observed that for films deposited with 20Ar/5N<sub>2</sub> the hardness generally increased with deposition temperature. For the films at -140V bias, the maximum hardness reached was at 25 °C, where the value was 2104 kg/mm<sup>2</sup>. The films deposited at 15Ar/10N<sub>2</sub> and 12Ar/12N<sub>2</sub> varied only slightly with increasing deposition temperature, and were consistently near 1000 kg/mm<sup>2</sup>. Menthe et al. [26] showed plasma-nitrided stainless steels to have a maximum Knoop hardness level of about 1000-1400 kg/mm<sup>2</sup> in samples where the surface layer was known to consist only of the S-phase, generally consistent with the results shown here.

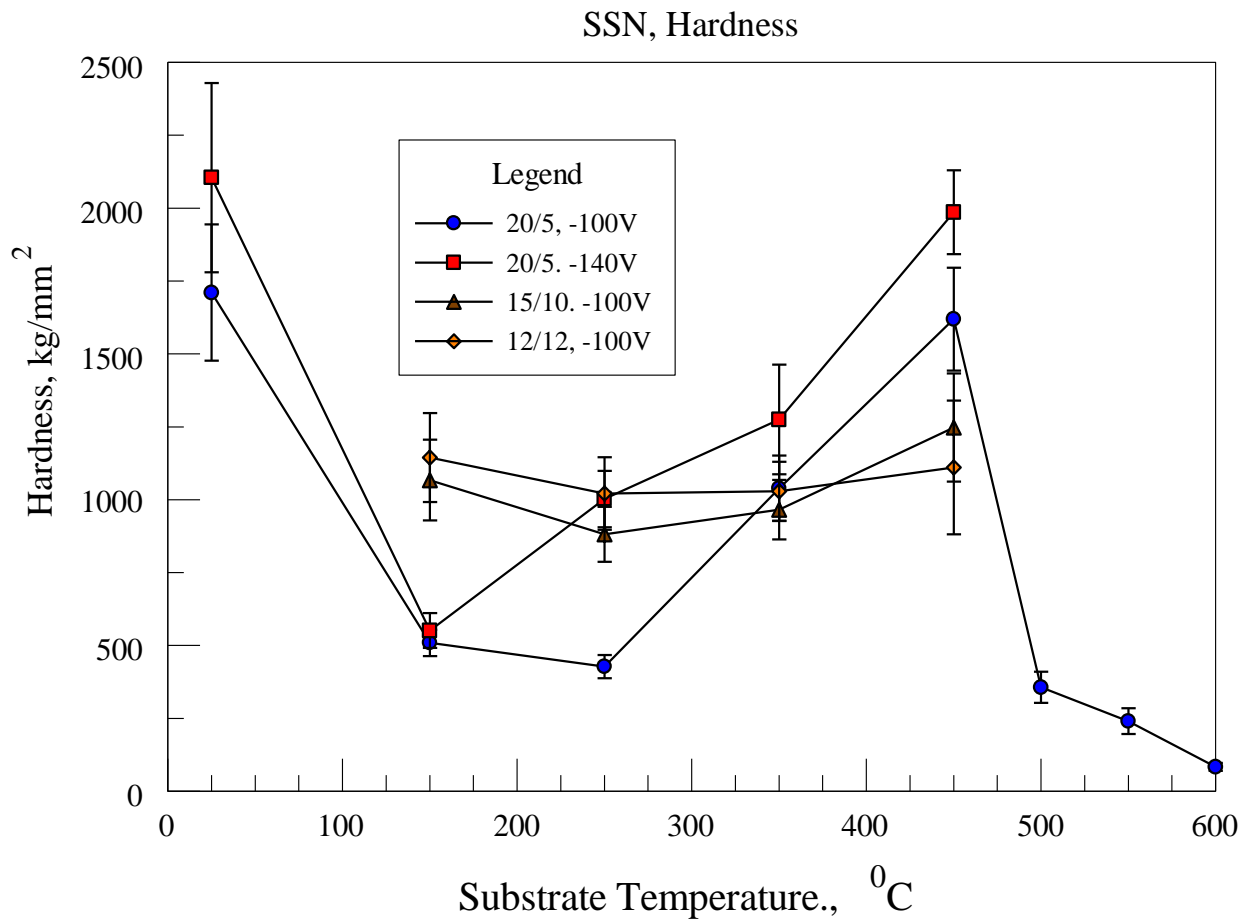


Figure 4.10: Knoop hardness measurements vs. deposition temperature for films deposited at the indicated parameters. The highest hardness achieved was near 2100 kg/mm<sup>2</sup> for the film deposited at 450°C/-140V/20Ar/5N<sub>2</sub>.

## 4.5. Discussion

Nitrogen-containing stainless steel films have been deposited using a variety of deposition parameters, with an emphasis on studying the effects of substrate temperature and nitrogen partial pressure during sputtering. Compositional analyses of the deposited films showed that the nitrogen content generally decreased with increasing substrate temperature. Generally, the residence times of adatoms on a substrate surface obeys an Arrhenius relating and decreases as temperature increases [80]. This suggests the chemical reaction of nitrogen with atoms on the substrate is weak and incorporation of the nitrogen in the film is favored by longer residence times at lower temperatures. In addition, higher nitrogen concentrations in the sputter gas favors nitrogen incorporation in the films, as shown by comparing the 20Ar/5N<sub>2</sub> and 15Ar/10N<sub>2</sub> films in Fig. 4.1. However, at a ratio of 12Ar/12N<sub>2</sub> there was not further significant increase in nitrogen in the films, so that it appears a saturation point was reached.

The XRD results for the films deposited below 450°C show the typical FCC pattern with a slightly displaced (200) peak. Further analysis using area-detector diffractometry gave the results shown in Fig. 4.5. In particular, it is useful to compare values for  $\psi = 0$  and values at  $\psi = 54.74^\circ$ , since this is the angle between the {200} and {111} planes in cubic systems. For example, unit cells with the (200) planes parallel to the sample surface, examined at  $\psi = 0$ , have corresponding (111) planes at  $\psi = 54.74^\circ$  where their interplanar spacings can be measured. At 200°C, for the (200), Fig. 4.4 shows  $a_{200} = 4.045\text{Å}$ , whereas the corresponding (111) planes indicate  $a_{111} = 3.935\text{Å}$ . The possibility of these results implying a face-centered tetragonal structure (with  $c > a$ )

can be examined by using the equations developed by Fewell and Priest [29], where if we assume that  $a_{200} = c$  then:

$$a = \left( \frac{2a_{111}^2 a_{200}^2}{3a_{200}^2 - a_{111}^2} \right)^{1/2} \quad [13]$$

Using the above values this gives  $a = 3.883A$  and a  $c/a$  ratio of 1.042. However, extrapolation of the  $a_{200}$  line to  $\psi = 90^\circ$  gives a value of 3.954A, which is inconsistent with the calculated value. Furthermore, the f.c.t. structure allows only two values of {200} d-spacings and peak splitting, or at least broadening, should be observed. However, no such effects were observed and instead we observed a gradual decline in  $a_{200}$  with  $\psi$ . Therefore, the results are inconsistent with this tetragonal structure.

The film morphologies observed here for S-phase samples are somewhat atypical of the columnar-type thin film structures commonly observed. The presence of sharp, angular facets was prominent in the cross-section views of many samples, as was the frequent observation of a layered morphology. These morphological characteristics were specific to the samples with the S-phase, and at higher deposition temperatures where the bcc-Fe/CrN/Ni phases were observed a more powder-like morphology was found.

The film morphology as well as nitrogen content are expected to have a significant impact on the hardness. Films deposited at lower temperatures and bias had a finer, discontinuous broken crystallite structure; as the temperature and bias increased (compare, for example Figs. 4.7(a) and (c)) the grains become larger, possibly giving a reduced void concentration. A second factor is the nitrogen content. As the nitrogen fraction in the sputtering gas increases, the

nitrogen concentration of the film is higher, as demonstrated in Fig. 4.1. It is well-known that stoichiometric nitrides, such as TiN and CrN, have very high hardness levels ( $\sim 2500 \text{ kg/mm}^2$ ). We may expect more nitrogen-deficient metal nitrides to have lower hardness levels. However, in the present case, the film deposited with 12Ar/12N<sub>2</sub> at 150°C, which had a dense columnar structure (Fig. 4.8a) and a N/Me ratio of 0.85 should have the highest hardness, yet it is surpassed by the film deposited at 25°C (20Ar/5N<sub>2</sub> and -140V) which has a N/Me ratio of 0.54 and hardness of near 2104.5 kg/mm<sup>2</sup>.

#### 4.6. Conclusions

Films for this study were deposited from a 304 stainless steel target in a mixed Ar/N<sub>2</sub> environment. Samples were analyzed using x-ray diffraction, x-ray photoelectron spectroscopy, SEM imaging of cross-sections and micro-hardness testing. Samples were deposited over a temperature range of 150-600°C, and it was found that the nitrogen content in the films decreased with increasing substrate temperature at a fixed nitrogen partial pressure. Increasing the nitrogen partial pressure increased the nitrogen content in the films, while increasing the bias slightly decreased it. Films deposited at higher temperature (>450°C) consisted of CrN, bcc-Fe and Ni, whereas films deposited at lower temperatures were primarily S-phase. The S-phase exhibited the well-known anomaly of a shifted (200) reflection in the XRD patterns, but the extent of this shift decreased with the degree of tilt of the planes relative to the surface. The SEM images for the S-phase samples showed highly angular and faceted crystallites, while films deposited at higher temperatures had a powder-like morphology. The

hardness of the films was also tested and a maximum of 2104 kg/mm<sup>2</sup> was achieved in a film deposited at 25°C and -140V bias.

## Chapter 5: The Effects of Ti Additions on the Structural, Mechanical and Tribological Properties of Stainless Steel-Nitride Thin Films

### 5.1 Composition Analysis of SS-Ti-N Films

Table 5.1 shows the deposited nitrogen-incorporated stainless steel and titanium films deposited onto silicon substrates. The films are divided into four groups as indicated in Table 4, with each group having common bias and gun power levels:

Group 1: Films were deposited using a power level of 150W on both sputter guns, a bias level of -100V, and a deposition time of 2h. The substrate temperature was ranged from room temperature to 350C. The nitrogen content in these films (absolute values between 30.41 and 35.27%) was similar to the stainless-steel nitride films (deposited without titanium) previously studied [101].

Group 2: The power to the SS gun was reduced to 50W to obtain a higher relative Ti concentration. To compensate for the reduced overall deposition rate, the time was increased to 3 hours. The Ti concentration was about double that of the previous set, and in addition the nitrogen content in the films was between 46.48 and 52.61 at. %. Nitrogen concentrations in rocksalt-structured transition metal nitrides are typically slightly less than 50%, so the values reported here may reflect the error range in the XPS measurement (estimated above as  $\pm 2-4\%$ ).

Group 3: Conditions here were similar to that of the second group except the bias voltage was increased to -140V. The bias did not appear to significantly influence the nitrogen content in the films.

Group 4: Films were deposited at equal stainless steel and titanium target-to-substrate distances and power levels of 150W (SS) and 175W (Ti). Here the nitrogen content average is 46.4%, which showed an enhancement of nitrogen content compared to the first group (33.8 at. % average). This may be due to the higher substrate bias.

In the discussion below films will be designated by group and temperature, for example, G1-150 will refer to the group 1 film deposited at 150°C, with additional parameters as shown in Table 5.1.

The effect of bias and the sputter gun power on the ratio of nitrogen (N) to metal (Fe + Cr + Ni + Ti) was calculated for all cases and the values are listed in Table 5.1. For films in groups 1, 2 and 3 increasing the substrate temperature does not lead to a substantial change in relative nitrogen content. The relative nitrogen content is mostly dependent on the concentration of Ti, as the Ti in the film acts as a getter for nitrogen.

Temp., °C	At.% Fe	At.% Cr	At. % Ni	At. % O	At.% N	At. % Ti	N/ (Fe+Ni+Cr+Ti)
<b>Group 1: -100V Bias, SS:150W, Ti:150W</b>							
<b>25</b>	35.62	9.26	4.42	10.21	35.27	5.23	0.6468
<b>150</b>	40.27	8.91	4.41	12.48	30.41	3.53	0.5323
<b>250</b>	37.9	9.63	4.34	8.53	34.78	4.79	0.6138
<b>350</b>	42.04	11.5	4.95	3.71	34.78	3.00	0.5654
<b>Group 2:-100V Bias, SS:50W, Ti:150W</b>							
<b>25</b>	23.7	6.85	5.22	2.65	50.32	11.23	1.0706
<b>150</b>	23.03	7.17	4.27	2.97	52.18	10.38	1.1634
<b>250</b>	22.42	6.15	5.87	4.45	46.48	14.63	0.9472
<b>350</b>	19.18	6.82	5.20	4.30	51.61	12.89	1.1705
<b>Group 3:-140V Bias, SS:50W, Ti:150W</b>							
<b>25</b>	23.04	6.18	5.09	4.27	50.33	11.09	1.1085
<b>150</b>	24.06	7.48	4.82	1.45	51.65	10.54	1.1012
<b>250</b>	21.79	6.39	4.62	3.22	52.86	11.13	1.2032
<b>350</b>	20.08	7.73	4.57	4.03	50.63	12.95	1.1169
<b>Group 4:-140V Bias, SS:150W, Ti:175W</b>							
<b>25</b>	28.98	9.22	3.37	5.04	47.94	5.45	1.0195
<b>150</b>	33.24	9.67	4.52	1.87	44.41	6.30	0.8265
<b>250</b>	26.15	7.62	5.29	4.53	46.89	9.52	0.9652
<b>350</b>	34.83	9.35	4.90	9	35.14	6.78	0.6290

**Table 5.1:** Deposition parameters and film compositions for the SS-Ti-N film

## 5.2 Crystal Structure

The influence of deposition parameters on crystal structure was studied using x-ray diffraction and the results are shown in Fig. 5.1. The main peaks (neglecting the peaks at  $33^\circ$  which are due to the Si substrate) are indexed as the (111), (200) and (220) reflections of the fcc structure. The film orientations vary, but a preferred (200) orientation is most common. The only film with a strong (111) orientation was the film G1-150. In contrast, the other films show either a mixed or (111) preferred orientation. Comparing the results for films in groups 1 and 2, where the bias remained constant but the gun power levels were altered to increase the Ti content in group 2 films, the peaks are observed to shift to lower angles indicating higher lattice constants. This is a result of the higher Ti and N concentrations in the group 2 films. Peak shifts are observed in comparing group 3 to group 4 films, where higher diffraction angles were found in the latter due to lower Ti and N concentrations.

Films of stainless steel nitrides typically have an S-phase structure, whereas TiN films are found to deposit with a rocksalt structure [102]. The difference is usually identified by examining the position of the (200) reflection based on the (111) position. The following equation can be used to assist in the evaluation of these structures:

$$R = \frac{\sin^2 \theta_{111}}{\sin^2 \theta_{200}} = \frac{d_{200}^2}{d_{111}^2} \quad (1)$$

For the standard fcc/rocksalt structure  $R = 0.75$ , but for S-phase structures  $R > 0.75$ . Table 5.2 shows the interplanar spacings, lattice constants, and R-values for the films deposited in this

study that had sufficient intensities in both the (111) and (200) peaks to enable reliable R-value calculations. All Group 1 films show  $R > 0.75$ , indicating S-phase formation. For films in Groups 2 and 3, where the nitrogen is at stoichiometric levels, the R values are very close to 0.75, indicating a primarily rocksalt structure. For films in Group 4, the films deposited at 25 and 350°C show  $R > 0.75$ , whereas for films deposited at 25 and 250°C the R-value is near 0.75. The higher value of R for film G4-350 is consistent with its lower nitrogen content (35.14%). Overall, the data suggests that for films with at least 10% Ti the nitrogen will be near the stoichiometric level and the rocksalt structure is formed, whereas below 10% Ti the films are sub-stoichiometric (typically less than 40% N) and the S-phase is formed.

For samples in Group 3, for the 25-250°C temperature range, only weak diffracting peaks were observed. Therefore, samples in this group were examined using the Bruker area-detector system, and rocking curves were obtained for the (111) reflection. The results are shown in Fig. 5.2, where  $\psi$  is the angle tilted away from the film normal axis. For the (nominally) room temperature deposition, there is some diffracted intensity near  $\psi = 0$ , but the strongest peaks are at  $\psi \cong 35-40^\circ$ . At 150°C, there is a broad peak centered near  $\psi = 8^\circ$ , and this orientation effect may be due to the gun tilt (guns were held at  $14^\circ$  to the substrate normal during deposition). At 250°C there is again a split in the rocking curve, which becomes wider at 350°C. This may be due to a grain coarsening effect at higher temperatures.

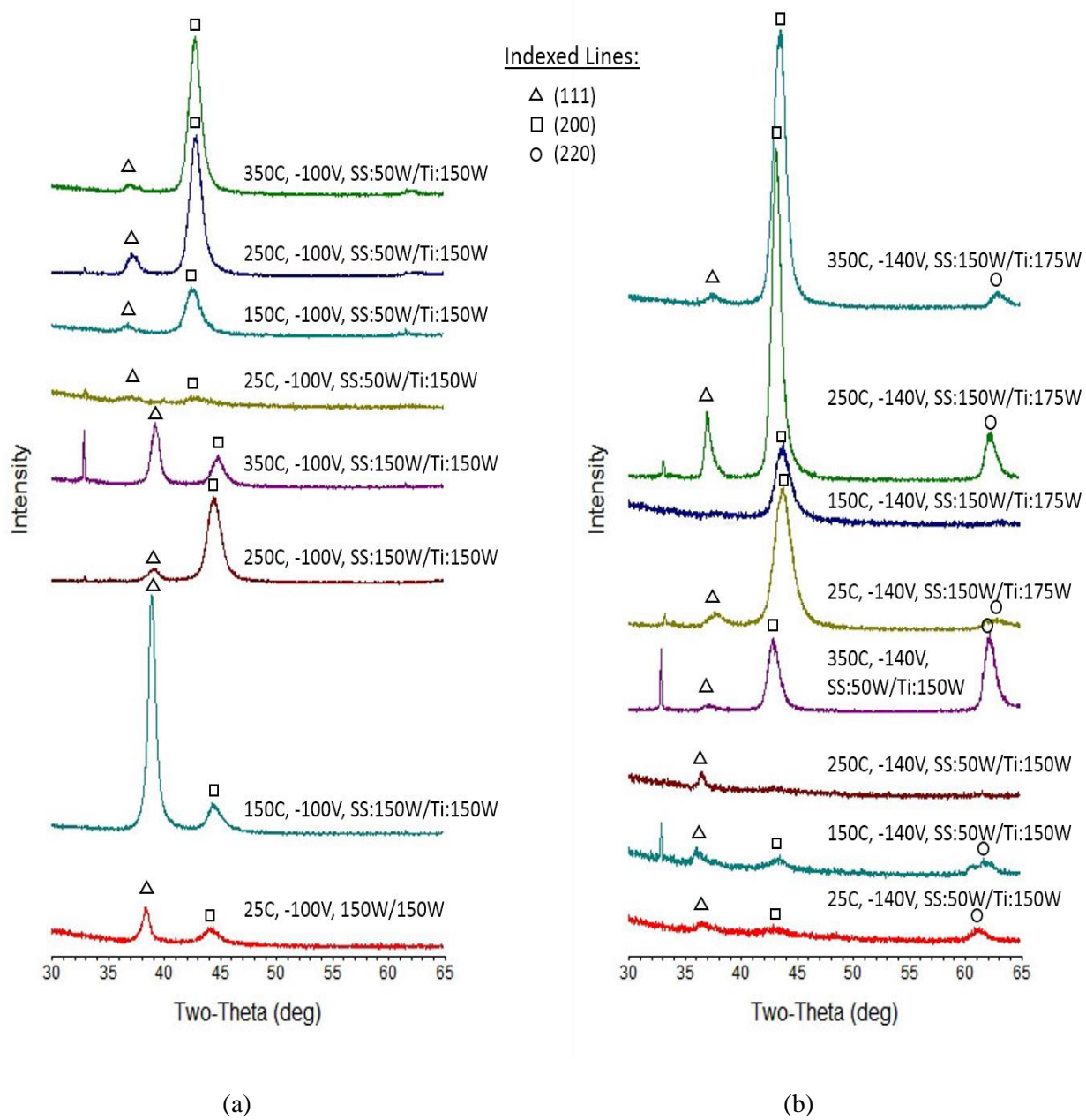


Figure 5.1: (a) XRD diffraction patterns of the films from groups 1 and 2, and (b) groups 3 and 4. Indexed lines for (111), (200) and (220) reflections are shown.

Sample	$d_{111}$ , nm	$d_{200}$ , nm	$a_{111}$ , nm	$a_{200}$ , nm	R
G1-25	0.234	0.205	0.405	0.410	0.767
G1-150	0.231	0.204	0.400	0.408	0.778
G1-250	0.230	0.203	0.398	0.407	0.784
G1-350	0.229	0.202	0.397	0.403	0.776
G2-250	0.241	0.211	0.418	0.422	0.765
G2-350	0.243	0.211	0.421	0.422	0.753
G3-350	0.242	0.211	0.420	0.421	0.757
G4-25	0.237	0.207	0.411	0.415	0.763
G4-250	0.242	0.209	0.420	0.419	0.747
G4-350	0.235	0.208	0.407	0.416	0.783

Table 5.2: Interplanar spacing and Lattice Constant Data

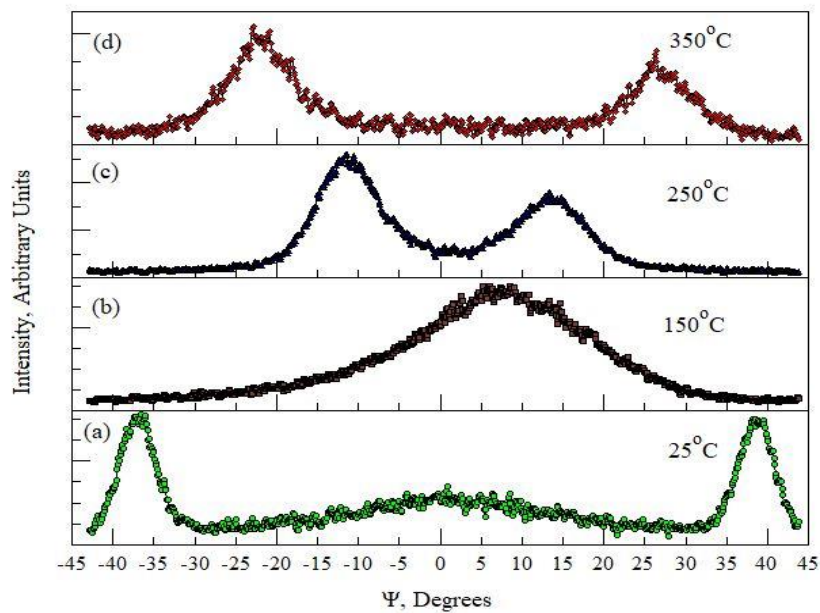


Figure 5.2: (111) rocking curves for the films in Group 3, for values ranging from  $-45$  to  $+45^\circ$ . Deposited films are: (a) G3-25; (b) G3-150; (c) G3-250 and (d) G3-350.

### 5.3 Microstructural Characterization

SEM cross-section images are shown in Figures 5.3(a-d) for the films in Group 1. In Fig. 5.3(a), deposited at 25°C, the film shows a granular-powder-like morphology. Increasing the temperature to 150°C, Fig. 5.3(b), shows a distinct columnar structure. Further increases to 250 and 350°C show a coarse, faceted morphology with a voided columnar structure indicating a low film density. The film thickness in these samples ranges from 2.4-2.9  $\mu\text{m}$ .

Fig. 5.4 (a-c) show films from Group 3, where the bias was constant at -140V, and the power to the stainless steel target was reduced to 50W. In these cases, the film thickness is significantly reduced, with film thicknesses measured at about 1000 nm. While the deposition time was increased by 50% compared to Group 1, it did not completely compensate for the lower power to the SS target. The films in this group show improved density and fewer voids compared to Group 1, and the film structure also shows less temperature dependence than Group 1. In addition, the films showed reduced surface roughness compared to those in Group 1. Films deposited in Group 2 were also examined and similarly show higher density but reduced film thickness compared to Group 1.

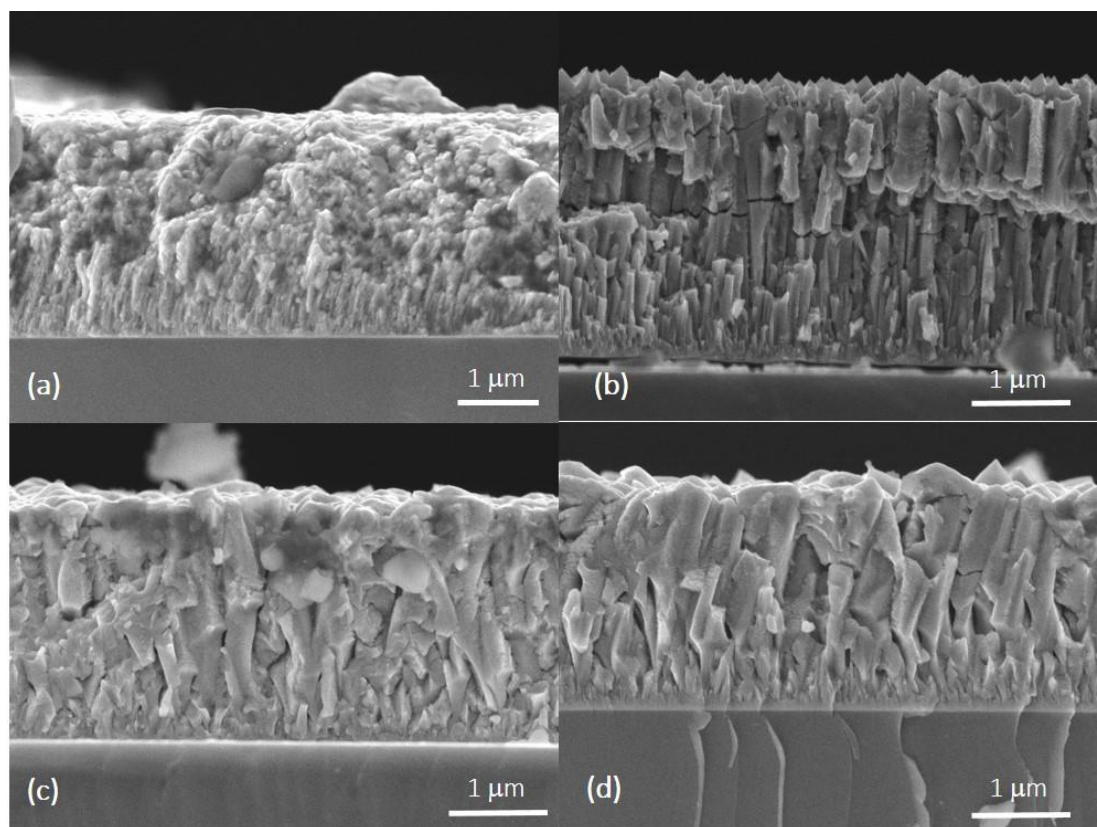


Figure 5.3: SEM cross-section images for films: (a) G1-25, (b) G1-150, (c) G1-250, and (d) G1-350. All images were taken in the secondary electron mode.

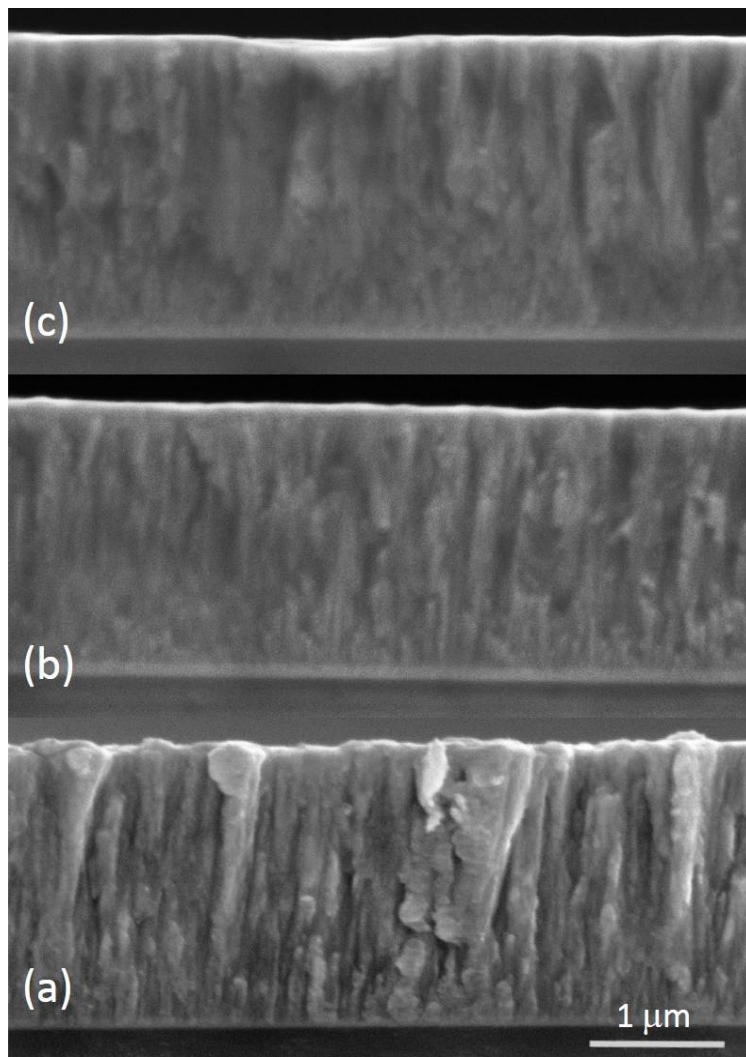


Figure: 5.4 SEM cross section images for films deposited from group 3 at substrate temperatures of (a) 150°C; (b) 250°C and (c) 350°C.

#### 5.4 Mechanical and Tribological Properties of SS-Ti-N

Micro-hardness testing was first used to measure film hardness using a 10-gram load and a Knoop indenter. This provided an assessment of the relative film hardness, and showed the samples in Groups 2 and 3 had the highest hardness. However, due to the reduced film thickness in these samples, it was necessary to use nano-indentation to obtain an accurate measure of film hardness. With nano-indentation, the appropriate load could be selected so that the indentation depth was close to 10% of the film thickness. The results of the nano-indentation tests for the selected films are shown in Fig. 5.4, where the hardness is shown. For films in Groups 2 and 3 (in the 150-350°C range) the hardness values ranged from 18-24 GPa. These values are typical for transition metal nitrides [50], and are significantly higher than previously reported levels for nitrided stainless steels [103]. One additional film was tested, sample G4-250, which had a somewhat lower hardness of 15.8 GPa. This film had a similar N/Metal ratio (see Table 4) as G2-250 as well as the same deposition temperature, although a higher bias level (-140V vs. -100V), which should improve hardness. The reduced hardness may be related to the higher deposition rate, which may result in a higher defect concentration.

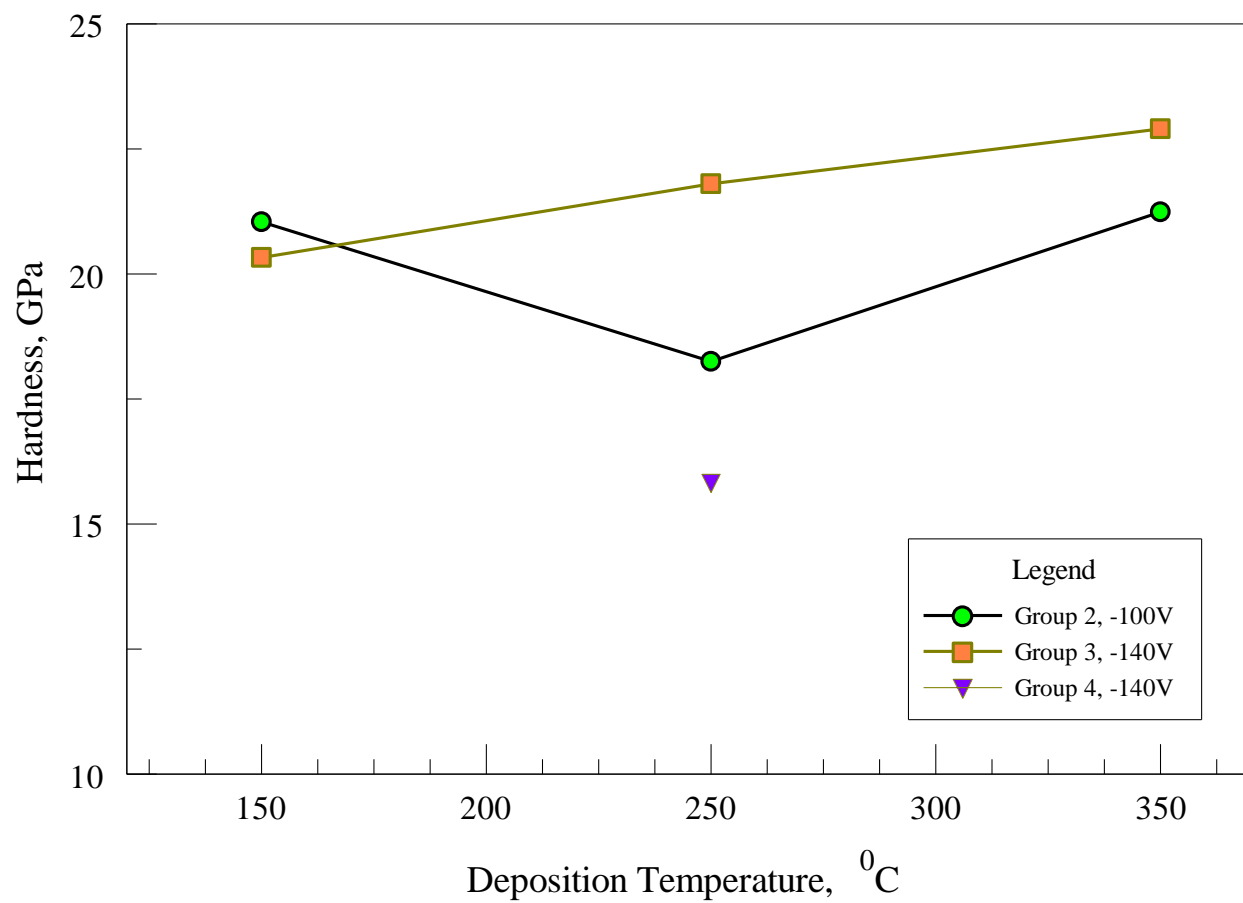


Figure 5.4: Nano-indentation hardness and reduced elastic modulus,  $E_r$ , for selected films. The average standard deviation in the measured hardness values was  $\pm 1.6$  GPa.

Pin-on-disk wear tests were used to evaluate the tribological behavior of selected SS-Ti-N films, primarily those exhibiting highest hardness levels. Coated stainless steel substrates were tested at room temperature using an Al<sub>2</sub>O<sub>3</sub> 6.25-mm diameter ball as the counter face. The load was 100g (1N), and the disc was rotated at 200 rpm, and the tests were run to 1000 cycles. Track diameters were typically 0.7-1.2 cm. Table 5.2 shows the results as the average friction coefficient ( $\mu$ ) over the range of 50-1000 cycles, the minimum and maximum within this range, and the standard deviation. Data for the first sample listed, SSN-140V, was obtained from a previous study [101] in order to compare the effects of Ti additions. This sample was deposited at the same sputter gas pressures (20Ar/5N<sub>2</sub>) and at a substrate temperature of 250°C. The tribological behavior of this film as well as sample G2-25 were poor, and so further tests were not conducted. Films deposited in group 3 (-140V bias) at 25 and 150°C showed better results, with an average friction coefficient of 0.39 for sample G3-150. Films in group 4 all showed higher friction coefficients (not shown), indicating poor wear behavior, which was confirmed by optical microscope observations of the wear tracks. Wear track images for several films are shown in Fig. 5.5. Fig. 5.5(a) shows film G2-25, where the high friction coefficient is consistent with the track image showing a heavily oxidized metallic compound, indicating rapid wear of the film and excessive interaction between the ball and steel substrate. Figs. 5.5(b) and (c), for films G3-25 and G3-150, show the coating is mostly intact, consistent with their lower friction coefficients. For sample G3-250, Fig. 5.5(d), the surface is worn to the steel substrate, but visually in terms of look at it, does not appear to be oxidized but rather shows the bare steel track. Nonetheless, the friction coefficient is higher due to interaction between the alumina ball and the steel substrate.

Sample	$\mu$ (average)	$\mu$ (max)	$\mu$ (min)	Std. dev.
SSN-140V	0.69	0.78	0.63	0.04
G2-25	0.72	0.99	0.47	0.13
G3-25	0.47	0.63	0.13	0.07
G3-150	0.39	0.52	0.29	0.04
G3-250	0.67	0.86	0.32	0.11
G4-25	0.78	0.86	0.72	0.03
G4-150	0.69	0.77	0.41	0.07
G4-250	0.82	0.89	0.76	0.03

Table 5.3: Pin-on-disk friction test results

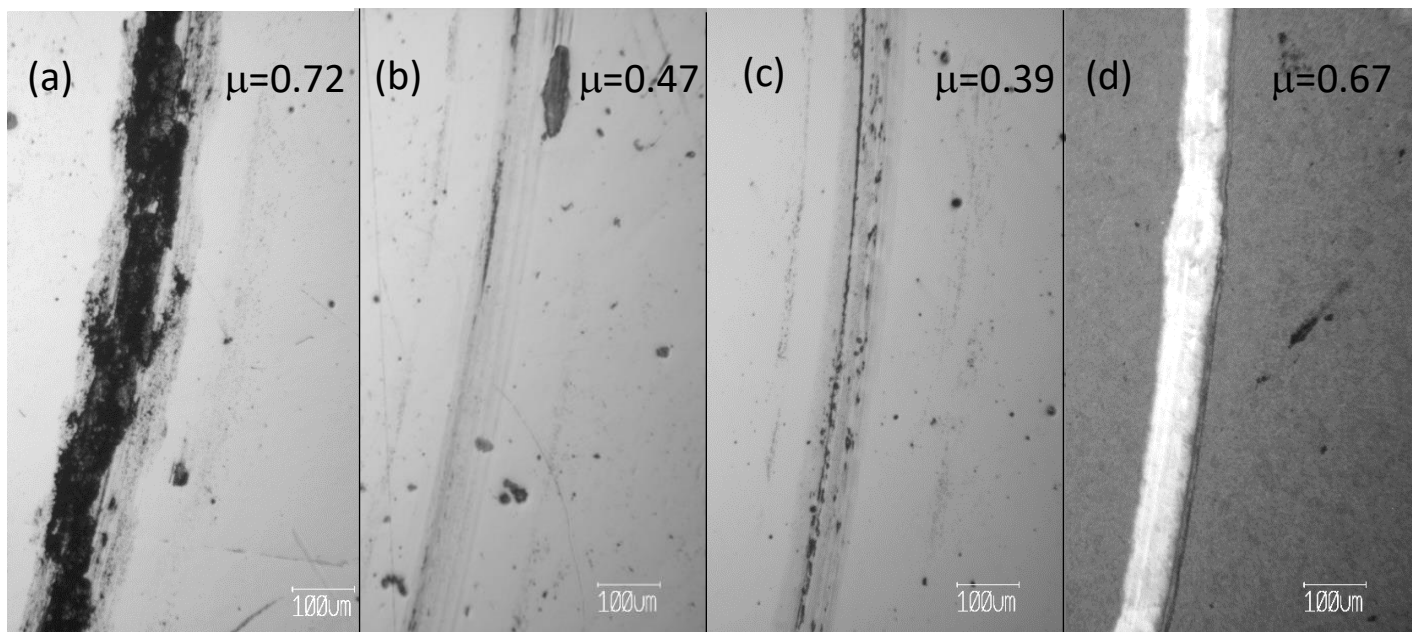


Figure 5.5: Wear track optical microscope images showing a typical portion of the wear track after 1000 cycles: (a) G2-25, (b) G3-25, (c) G3-150 and (d) G3-250.

## 5.5 Discussion

Films of nitrogen-incorporated stainless steel have been modified by the addition of titanium by co-sputtering, and the structure and mechanical properties of the films have been examined. For SS-N films with average Ti concentrations of 4.1% (group 1 in Table 4) the concentration of N was similar to films deposited without Ti [101]. However, additions of Ti at concentrations of 12.2% (Group 2 average) or 11.4% (Group 3 average) increased the N concentration to typical stoichiometric levels. The elements within stainless steel have varying affinities for nitrogen. Both Fe and Cr are known nitride formers, with CrN being a commonly used and studied hard coating [104-106]. Fe-nitrides are less commonly used as hard coatings, but some studies have been conducted to examine their synthesis and mechanical properties [107-109]. In contrast, Ni has little affinity for nitrogen and is a poor nitride former, however, films of nickel nitrides have been synthesized and studied [110, 111]. Ti is a strong nitride forming element and will readily react with available molecular nitrogen. Therefore, it is not surprising that Ti increases the N content in the deposited films. However, there appears to be a threshold in Ti content required to significantly increase the N concentration in the films, and the current experiments indicate this is between 4 and 10%Ti (this would require between 8 and 20% in the metallic source or target material). X-ray diffraction analysis of the higher-Ti films did not show any peak splitting or evidence of phase separation between Ti and the stainless steel constituents. This suggests that the Ti atoms occupy random sites on the metal sublattice. As a result of the Ti additions, the hardness levels are significantly increased. Hardness levels for stainless steel nitrides are typically 10-15 GPa [26,28,30,34,36,38] although in thin films nitrides, there is a strong dependence on deposition method and parameters used. In our recent study we found a Knoop hardness of

1275 kg/mm<sup>2</sup> for S-phase-structured films deposited at 350C and a bias of -140V bias. Under similar conditions for the films in the present study, namely, sample G3-350, the hardness was 23.9 GPa (equivalent to 2437 kg/mm<sup>2</sup>, thereby representing nearly twice the hardness. For the N-stoichiometric films in groups 2 and 3 the hardness ranged from 18.2-22.9 GPa, which is in the typical hardness range for transition metal nitrides such as TiN and CrN [113].

The pin-on-disk test showed that films G3-25 and G3-150 had the best overall results. It is notable the film G3-250, despite having a similar hardness levels as G3-150, did not perform as well. This may be due to temperature effect on grain structure as well as the change in film texture as indicated in Fig. 5.3.

## 5.6 Conclusions

Films of nitrogen-incorporated stainless steel have been augmented by co-sputtering with titanium in a mixed Ar/N<sub>2</sub> atmosphere. Calculated R-values and measured nitrogen contents in the films showed that either the S-phase or the rocksalt structure can be formed. Increasing the substrate temperature leads to an increase in the  $2\theta$  peak angles. It was found that with sufficient Ti in the films (~11-14%) the nitrogen content can be raised to stoichiometric levels. The hardness of the films also increased as a result, and a maximum of 23.9 GPa was obtained, which is well above hard levels typically reported for stainless steel nitride films without Ti additives or plasma-nitrided bulk stainless steels. The tribological properties of selected films were also examined, and in one case an average friction coefficient of 0.4 was realized.

## Chapter 6: A comprehensive study of the effect of R-Values on Nitrogen and Substrate Temperature on SSN-60V and selected films from Chapters 4 and 5

### 6.1 X-ray diffraction spectrum Results

Fig. 6.1 shows an X-ray diffraction spectrum from sample S-150-60 (150C, -60V Bias). Two peaks are indexed, (111) and (200), based on an FCC structure. An additional spectrum (not shown) covering the higher  $2\theta$  range enabled the peak positions for (311) and (222) to be obtained. (The (220) peak position could not be obtained due to interference from the Si substrate.) The analyzed data shown in the figure demonstrate the deviation in the (200) lattice spacing compared to the remaining peak. The expected position for the (200) peak, based on an FCC structure, should be at  $45.5^\circ$ , indicating a (200) shift of  $1.4^\circ$  to lower angles. XRD data for the remaining films were obtained and the results for the  $a_{111}$ ,  $a_{200}$  and R-values are shown in Table 7. Also, table 6.1 shows the atomic percent nitrogen and titanium, with the balance being metallic elements in 304 stainless steel (Fe, Ni, Cr in a distribution reflecting that of the target), as well as oxygen (up to 7 at.%). The accuracy in nitrogen concentration measurements is estimated to be  $\pm 2-4$  at.% N. It can be noted that the R-values are all greater than 0.75. The closest to 0.75 are the high titanium films (sample name terminating in "H"), where values only slightly greater than 0.75 were obtained. These films also had the highest nitrogen content, with an average of 50.1% N. In comparison, samples with lower Ti concentrations (terminating in "L") had lower nitrogen concentrations and higher R-values. One sample was deposited at  $25^\circ\text{C}$  where the R-value was 0.766. For samples deposited without Ti, room-temperature depositions

did not result in a crystalline structure. The addition of Ti promotes crystallization and therefore allowed measurement of the R-value.

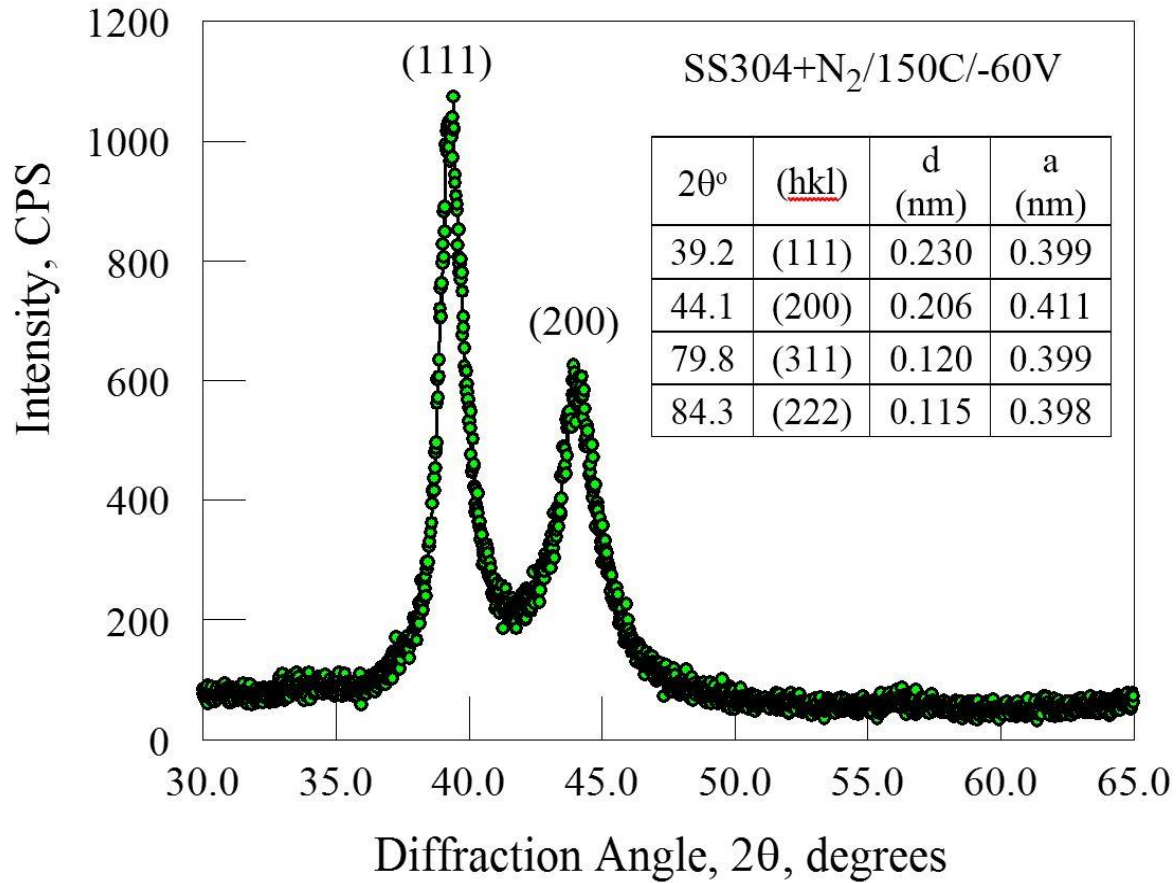


Figure 6.1: X-ray diffraction spectrum from a sputter-deposited SS304+N<sub>2</sub> film, deposited at 150°C and -60V bias. The two peaks are indexed as (111) and (200) based on an FCC structure. An additional spectrum (not shown) was obtained at the higher 2θ range to obtain the peak positions for (311) and (222). The analyzed data are shown in the table, demonstrating the deviation in the (200) lattice spacing; the normal position for the (200) peak should be at 45.5°, indicating a (200) shift of 1.4° to lower angles.

Sample	Substrate Temp. (C)	Substrate Bias, -V	$a_{111}$ , A	$a_{200}$ , A	R-Value	FWHM, Deg-2 $\theta$	% N (At.%)	% Ti (At.%)
S-150-60	150	-60	3.990	4.110	0.802	0.601	32.5	-
S-250-60	250	-60	3.973	4.071	0.787	0.468	38.9	-
S-350-60	350	-60	3.973	4.050	0.779	0.493	40.1	-
S-150-100	150	-100	3.923	4.033	0.792	0.540	30.7	-
S-250-100	250	-100	3.923	3.992	0.777	0.478	33.3	-
S-250-100-LR	250	-100	3.931	4.072	0.805	0.514	43	-
S-350-100	350	-100	3.903	3.950	0.768	0.416	32.7	-
S-250-140	250	-140	3.877	4.016	0.805	0.429	29.2	-
S-350-140	350	-140	3.877	3.956	0.781	0.523	30.7	-
S-Ti-25-100L	25	-100	4.060	4.102	0.766	0.429	35.3	5.23
S-Ti-150-100L	150	-100	3.908	4.083	0.818	0.485	30.4	3.53
S-Ti-250-100L	250	-100	3.977	4.072	0.786	0.478	34.8	4.79
S-Ti-350-100L	350	-100	3.976	4.040	0.774	0.434	34.8	3
S-Ti-150-100H	150	-100	4.233	4.251	0.757	0.535	52.2	10.4
S-Ti-150-100H	250	-100	4.185	4.216	0.761	0.468	46.5	14.6
S-Ti-150-100H	350	-100	4.213	4.227	0.755	0.511	51.6	12.9

Table 6.1: Description of Samples Deposited and Basic Parameters

## 6.2 Effect of the variation in nitrogen concentration in the films and the substrate temperature

The nitrogen content vs. the substrate temperature is shown in Fig. 6.2 for films deposited in the 150-350°C temperature range (except the “LR” film which will be discussed separately). For the films without Ti deposited at -60 and -100V bias, the nitrogen content first increases with temperature from 150 to 250°C and then remains essentially level to 350°C (For the films deposited at -140V bias, the film deposited at 150°C was amorphous, and therefore not included in this analysis). The effect of bias shows an overall decrease in nitrogen content as the substrate biased is increased from -60 to -140V. The nitrogen content in these films can be influenced by sputtering as well as implantation effects, depending on the ion energy and incident angle. The results shown here suggest that at -60V, the effects of sputtering or implantation are likely to be minimal. Increasing the bias to -100V causes some sputtering of N atoms to occur, resulting in lower nitrogen contents. Increasing the bias level to -140V may cause additional sputtering to occur, reducing nitrogen content further. For the films co-deposited with Ti, with low Ti concentrations (an average of 4.1%) the Ti level was not sufficient to significantly impact nitrogen concentration. For films with high Ti concentrations nitrogen levels increased significantly and achieved stoichiometric levels.

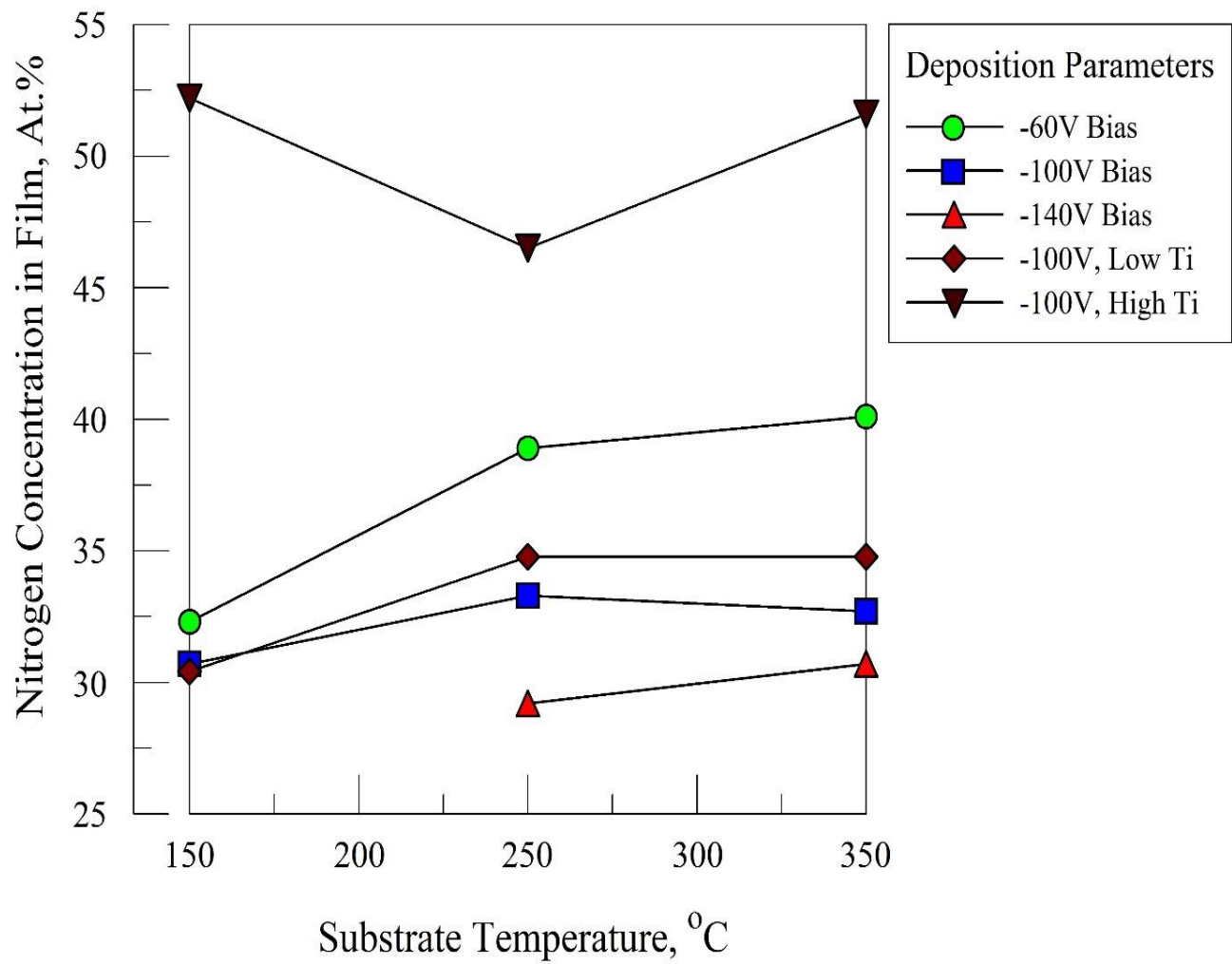


Figure 6.2: Variation in nitrogen concentration in the films vs the substrate temperature. Note there is no consistent temperature dependence observed within this temperature range.

### 6.3 Effect of Variation in R-value with Nitrogen Concentrations and Substrate Temperature

The variation in R-value with nitrogen content for all films is shown in Fig. 6.3. The intent here is to first set aside any possible dependence on deposition parameters and determine if there are any global trends that can relate the nitrogen concentrations in the film to the R-values. R-values close to 0.75 correspond to films that are at or near 50 at.% N. Overall, at higher R-values correspond to lower nitrogen contents, although there is significant scatter between these variables at intermediate nitrogen concentrations. The R-values for films deposited at different temperature and bias levels are shown in Fig. 6.4. With the exception of the high Ti films, the temperature dependence shows a decreasing R-value with increasing temperature. Starting with the -60V samples, we note that increasing the bias to -100V results in a nearly parallel line but at lower R-values. The fact that the -60V films have higher R-values that cannot be attributed to their higher N content, as Fig. 6.3 shows the tendency would be to reduce, rather than increase, R. For the films deposited at -140V, the R-values are higher than those deposited at -100V, despite the similar nitrogen levels. This suggests that the extent of the anomalous (200) peak shift is not due to nitrogen-induced modifications in crystal structure, but may also be related to deposition-dependent properties such as stress, grain structure and defect formation in the films. The fact that substrate bias and temperature strongly influence R-values demonstrates a possible dependence on these microstructural effects.

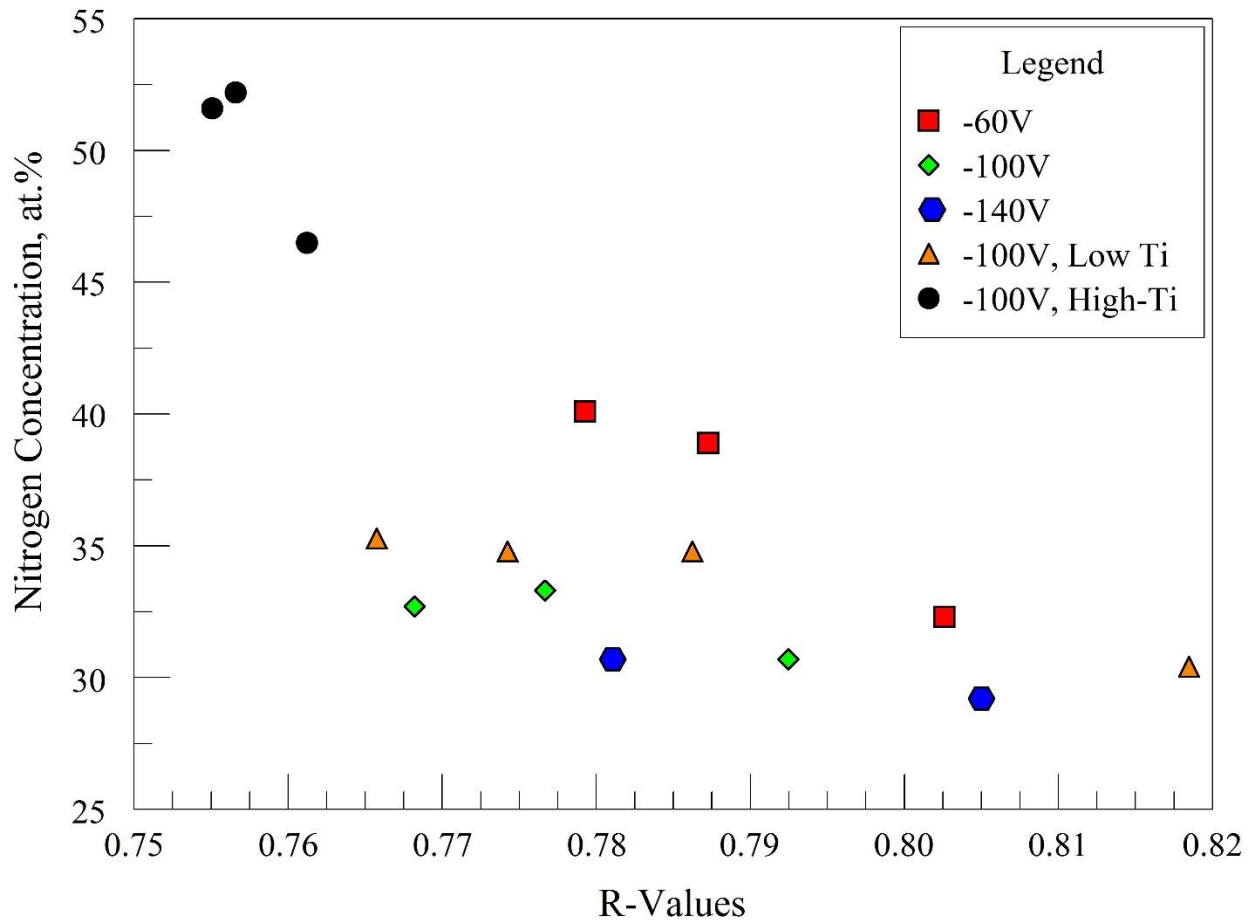


Figure 6.3: Variation in nitrogen content with R-values for all data given in Table 4.1. A systematic trend is observed where decreased N concentrations correspond to higher R-values.

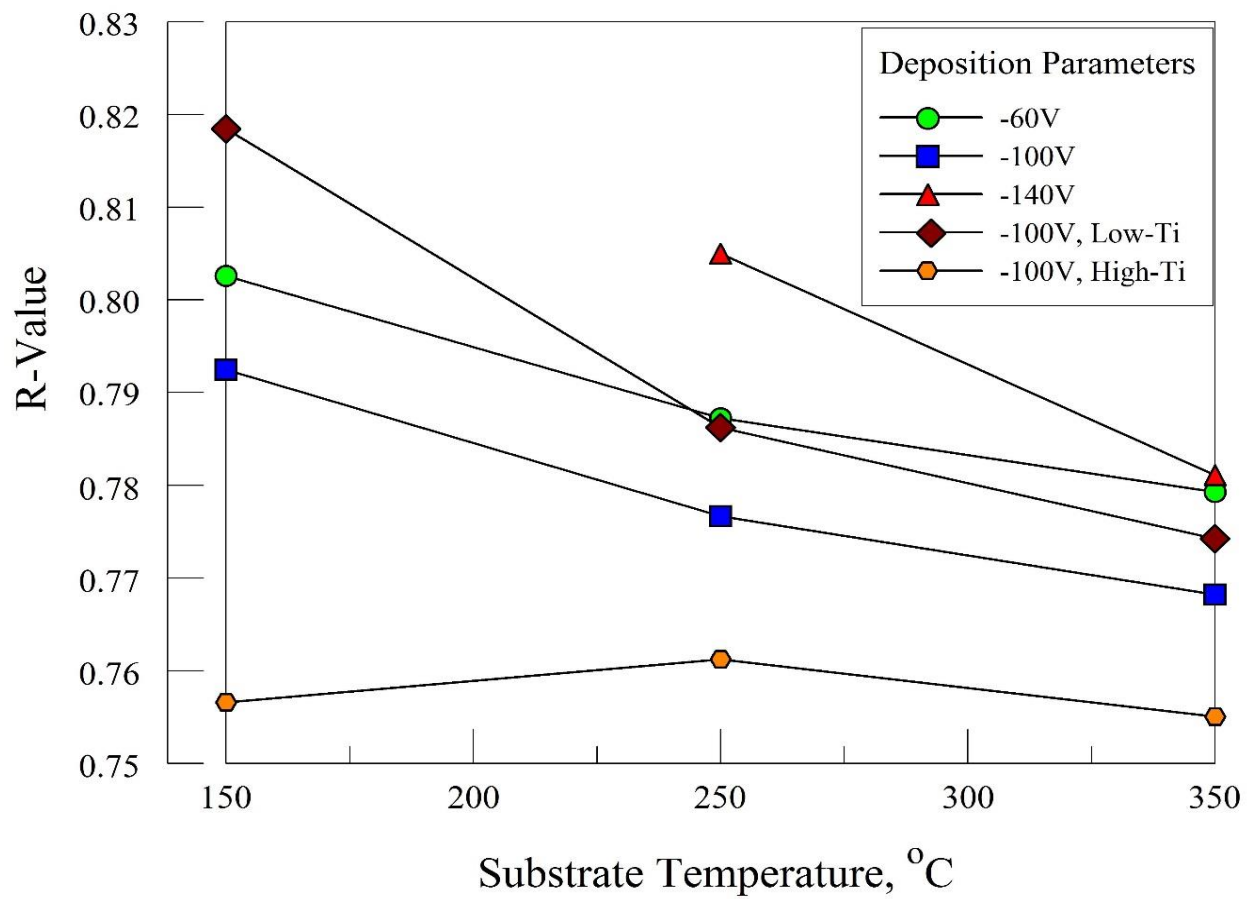


Figure 6.4: R-values vs. substrate temperature for films deposited at different substrate bias levels as well as films co-deposited with Ti. Except for the high-Ti films (which also had stoichiometric nitrogen levels) the R-values declined with increasing temperature.

#### 6.4 Influence of R-values on the Morphology of Low Titanium Films

In order to better understand the microstructural features that may be responsible for the change in R-values with substrate temperature, SEM cross-section images were examined. Fig. 6.5 shows SEM cross-section for the “Low-Ti” samples (designated S-Ti-X-100L where X is the substrate temperature), all deposited at -100V bias. The R-values for these samples are indicated in Table 7.7. The lowest R-value was for sample S-Ti-25-100L (25°C, R = 0.766), shown in Fig. 6.5(a), showing a fibrous-to-columnar structure with small, faceted crystallites present at an angle to the growth direction. The sample shown in Fig. 6.5(b), deposited at 150°C, had the highest R-value (0.818) of all samples, and showed a distinctly columnar structure, but still with faceted boundaries that terminate at the surface with faceted column tips. Significant layering or a feather-like morphology is evident in this image. As the substrate temperature increase further (Figs. 6.5(c) and (d), 250 and 350°C, respectively) the overall structure continued to coarsen. However, a close examination of the images shows continued effects of faceting, a layered morphology within the columns. This type of layered morphology has been viewed previously [101], and it was suggested that this lamellar-type morphology may be related to stacking fault formation, which is one hypothesis for the anomalous (200) peak position shift [60-63]. The films deposited at -140V (S-250-140 and S-350-140) similarly showed faceted, angular crystallites, along with evidence of layered structures.

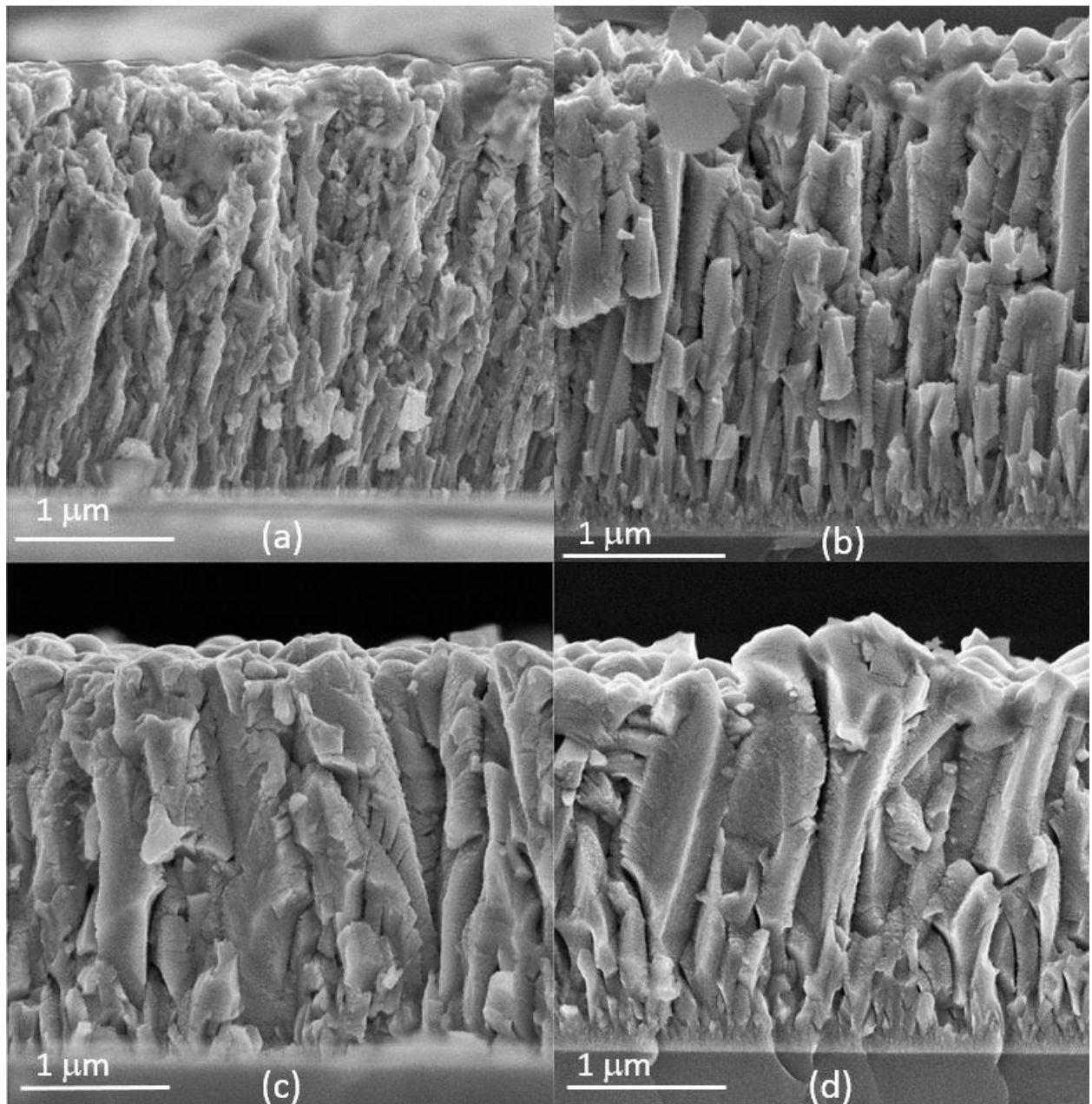


Figure 6.5: SEM cross-section images of films deposited at low-Ti concentrations: (a) S-Ti-25-100L, (b) S-Ti-150-100L, (c) S-Ti-250-100L and (d) S-Ti-350-100L. Images all show evidence of a layered morphology within the columnar structures, and a general coarsening of the structures as the substrate temperature is increased.

In order to examine the structures in more detail, cross-section TEM samples were prepared. Fig. 6.6 (a-c) shows bright-field TEM images obtained for samples deposited at -60V. Fig. 6.6(a) shows the microstructure of the sample deposited at 150°C with a corresponding  $R = 0.802$ . In this case, the structure is open and porous but also shows a “feather-like” morphology exhibiting a structure with a central spine and branches growing at an angle to the surface. In 6.6(b), deposited at 250°C and having  $R=0.787$ , this type of morphology is still present but overall the structure is somewhat denser. At 350°C (Fig. 6.6c,  $R = 0.779$ ) the structure is still more dense with less evidence of a feathered morphology. As noted by Petrov et al. [114] the presence of inter- and intra-columnar voids as well as a characteristic dendritic pattern is due to limited surface diffusion, with films deposited under conditions of lower substrate temperatures or an insufficient ion flux.

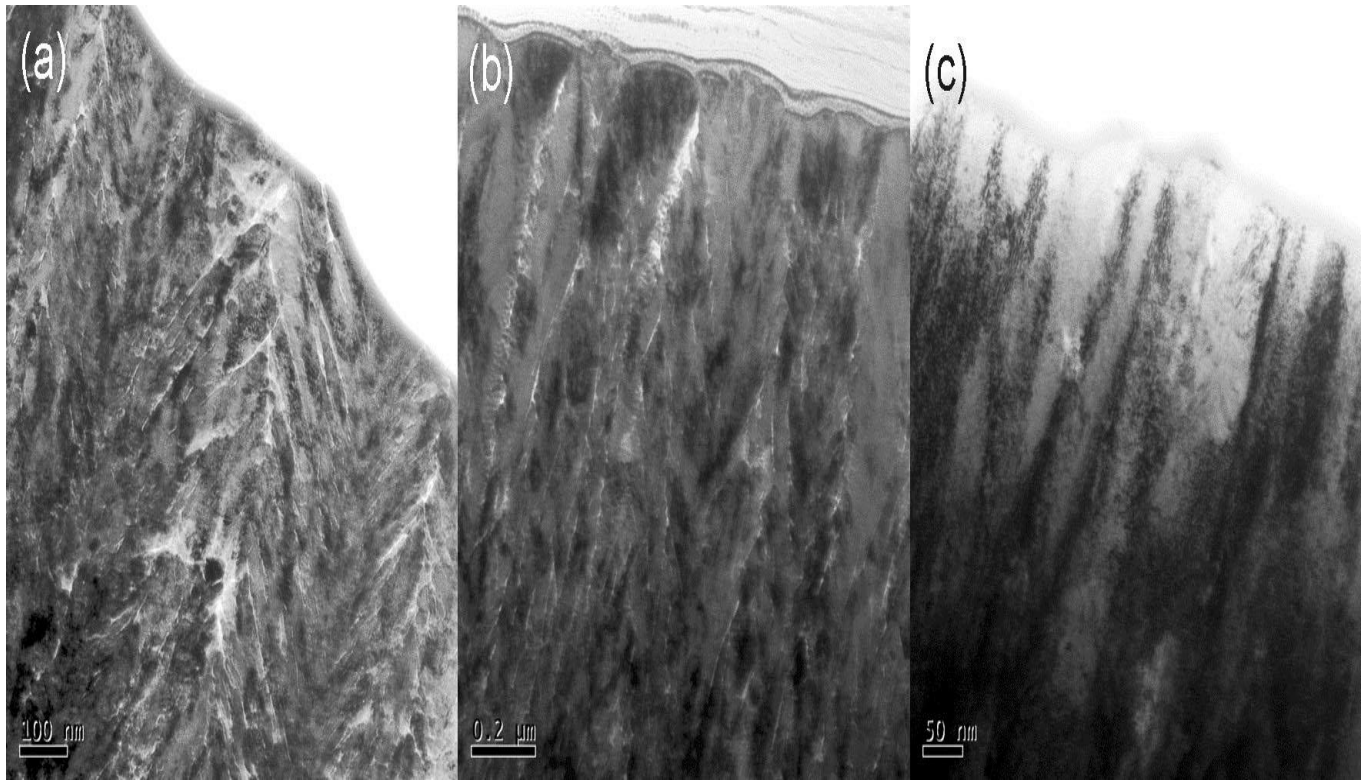


Figure 6.6: TEM image samples deposited at -60V bias: (a) S-150-60, (b) S-250-60, and (c) S-350-60. Examples of a layer-morphology can be found throughout (a) but the films become more dense as the substrate temperature is increased. (The top surface of the film is in the direction of the top of the micrograph).

## 6.5 Determination the Effect of Stacking Faults on The shift in the Peak Positions Using Warren's Model

The layered or branched morphology observed in the SEM/TEM images could be related to stacking fault or twin formation, which as noted above is a current hypothesis for the diffraction anomaly. For the current samples, a preliminary estimate can be made for the value of  $\alpha$ . Based on Figs. 6.5 and 6.6, the layer thickness is estimated to be  $t \sim 30$  nm. Using the experimental (111) interplanar spacing of  $\sim 0.23$  nm, this gives  $1/\alpha = 130$  or  $\alpha = 0.0077$ . Eq. 1 can then be used to calculate the expected peak shift, and gives  $\Delta 2\theta = 0.022^\circ$ ; for the samples listed in Table 7 that do not contain Ti, the average deviation of the (200) peak from its expected value (based on the position of the (111) peak) is  $1.2^\circ$ . Therefore, there is poor agreement in the magnitude of the peak shifts, in fact the values disagree by nearly two orders of magnitude. Alternatively, one can calculate the expected values of  $\alpha$  based on the experimental peak shift, and the results show expected stacking faults every 2-3 atomic planes.

In order to examine the effects of limited surface diffusion and crystallite domain size in a more comprehensive manner, the full-width-half-maximum (FWHM) was determined for the primary (strongest) peak for each diffraction pattern, and the results are tabulated in Table 6.1 Examination of these data showed no correlation between the FWHM and R-values. One might expect low R-values to correlate with larger domain sizes and reduced defect concentrations and therefore smaller FWHM values. Within a given set of samples some correlation is observed, for example for the -100V samples as temperature increases from 150 to 350°C, the FWHM and R-values both decrease. However, the -60V samples show an inconsistent trend and the -140V

samples show a reverse trend where the sample with higher FWHM has a lower R-value. The samples with low-Ti show a decrease in both R-value and the FWHM over the 150-350°C temperature range; the room temperature sample continues this trend, but it was surprising to find both a low FWHM (0.423) and R-value (0.766) in that sample as room temperature depositions for films without Ti are typically amorphous. For the high-Ti films, the FWHM values were comparatively large, while the R-values were very low (close to 0.75). Overall, the absence of a consistent correlation between the measured FWHM values and R-values indicates that fine crystallite domains and high defect concentrations, typically responsible for peak broadening, are not responsible for R-values deviating from the expected value of 0.75.

One additional film was deposited is reported in Table 6.1 as sample “S-250-100-LR”. This is a lower deposition rate version of sample S-250-100. The latter had a deposition rate of 0.33 nm/sec, and for the “-LR” film the power to the sputter gun was reduced in order to reduce the deposition rate by a factor of two. The concept proposed was that reducing the deposition rate would reduce the density of defects as atoms arriving at the film surface would have a longer time to find equilibrium positions in the lattice. Based on this approach, as well as the fact that the nitrogen concentration increased from 33.3 to 43% (see Table 6.1), the -LR film should have a lower value of R. Instead, the value increased from 0.777 to 0.805.

## 6.6 Discussion

In this study the extent of the well-known diffraction anomaly (the (200) peak shift) observed in the S-phase of nitrided stainless steel films has been characterized by calculating “R-values” from x-ray diffraction patterns. R-values from 0.755 to 0.818 were obtained from samples deposited using a variety of deposition conditions. While R-values have typically not been reported in the literature from previous studies, calculation of this parameter can be easily determined from published x-ray diffraction scans or tabulated data. For example, in the study by Abronis et al. [115] for N-implanted 316 had  $R = 0.78$ ; Sun et al. [59] examined plasma-nitrided 316 and obtained  $R = 0.81$ , and Kappaganthu and Sun [38] deposited films by reactive sputtering using a range of nitrogen gas concentrations and obtained R-values ranging from 0.764 to 0.781. They also obtained stoichiometric films which had R-values of 0.75. Therefore, the R-values determined from the literature are similar to those found in this study.

For the samples examined here, the effect of nitrogen concentration in the films was first examined as shown in Figs. 6.2 and 6.3. Fig. 6.3 shows data for the films deposited in this study, and the R-value is observed to generally increase with decreasing nitrogen concentrations, but there is significant scatter in the data. Therefore, additional factors were examined. The results showed a decrease in R-value with increasing substrate temperature (Fig. 6.4), except for films with high titanium which were essentially stoichiometric nitrides with R-values near 0.75. The effect of bias was less consistent: as bias increase from -60 to 100V the R-values decreased, but further increase to -140V bias resulted in substantial increases in the R-values. The lower-

concentration Ti films showed the effects of Ti in those films was to increase R (as shown in Fig. .64).

Examination of the film morphology (Figs. .65 and .66) showed typical features (voids, faceted columns, and feather-like structures) indicative of surface-diffusion-limited film growth. Coarser structures were observed at the higher deposition temperatures, and as shown in Fig. .64, the R-values generally decreased with temperature. However, film S-Ti-25-100L had a fine-scale structure but also a relatively low R-value, and the films deposited with high-Ti had a higher FWHM but also a near theoretical values of R. Our conclusion from these observations is that film morphology has little direct influence on the diffraction anomaly. The presence of twin or stacking fault related domains also does not provide a suitable explanation for the diffraction anomaly. The basis for this statement is that the extent of the shift of the (200) peak, calculated using Eq. (2), suggests very high stacking fault densities, and a high density of twins and stacking faults were generally not observed in TEM samples.

As reviewed in chapter 2, there has been considerable effort to identify a crystal structure that would account for the observed diffraction patterns. Fewell and Priest [49] attempted to fit extended diffraction data to rhombohedral, monoclinic, tetragonal and triclinic lattices but none were completely satisfactory. Calculation of Bragg reflections for these lattices assumes long-range order, with atoms in essentially fixed positions based on a repeated unit cell model. The difficulty in using this approach for the S-phase structure is that there is a high concentration of vacancies on the nitrogen sublattice, and hence while the structure is nominally fcc, slight variations are expected that will cause deviations into slightly tetragonal, monoclinic, etc. unit cells. The concept is illustrated schematically in Fig. .67. In Fig. .67(a) a two-dimensional

representation is shown for the (100) face of the rocksalt structure. In Fig. 6.7(b), the structure is shown with approximately one-half of the nitrogen atoms removed. This creates locally unstable positions for the metal atoms and some distortions of the lattice are expected, as shown schematically in Fig. 6.7(c). In the actual S-phase structure for nitride stainless steels, the metal atoms of Fe, Cr and Ni are expected to be randomly located on the metal lattice. It has been found that nitrogen atoms can be preferentially located near Cr atoms [116], but chromium nitride phases were not observed. Therefore, the proposed structure is one of small domains of slightly distorted fcc unit cells which result in broad peaks in XRD. A verification of this concept will require a full simulation of the structure and calculation of resulting diffraction patterns, which is beyond the scope of the present study.

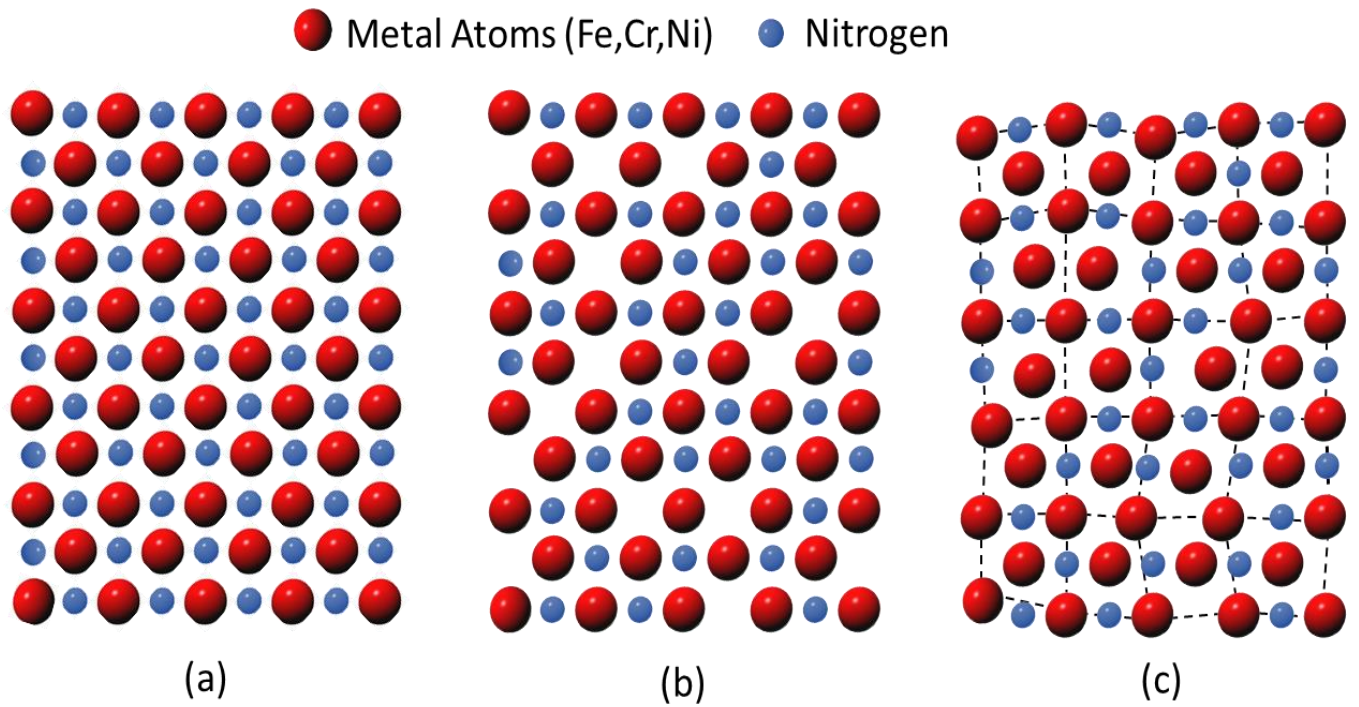


Figure 6.7: Proposed model for the S-phase structure: (a) normal stoichiometric nitride structure; (b) nitride structure with approximately 50% nitrogen interstitials removed; (c) distorted lattice resulting from the relaxation of the metal sublattice due to a high concentration of vacancies on the nitrogen sublattice.

## 6.7 Conclusions

Reactive magnetron sputter deposition was used to deposit films of stainless steel and stainless steel/titanium in a mixed Ar/N<sub>2</sub> gas atmosphere. A variety of deposition parameters were systematically investigated, including substrate temperature and substrate bias. The extent of S-phase formation was monitored by calculating the R-values for each sample, which accounts for the anomalous (200) peak shift. Films with the least deviation from the ideal FCC structure were those with the highest titanium levels (10-14 at.% Ti), which also had nitrogen contents close to the stoichiometric levels (~50 at.% N). Sub-stoichiometric films had higher R-values (>0.75), and there was a weak correlation between decreasing N-content and increasing R-values. The correlation of R-value to the substrate temperature for films deposited for sub-stoichiometric films showed that, for a given metal composition and bias, an increase in the deposition temperature led to a decrease in the R-value. The effect of the bias was less consistent, showing (for a given substrate temperature) a decrease in R-values from -60 to -100V but then increasing at -140V. SEM cross-section analysis showed voided, faceted boundaries with a general coarsening as substrate temperature increased. TEM examination also showed a faceted, dendritic structure, with improved film density at higher substrate temperatures. The scale of the layered morphological structures observed in the SEM/TEM images did not agree with the calculated stacking fault density based on Warren's equation (Eq. 6) for peak shifts. It is concluded that the film morphology is not directly responsible for the extent of the diffraction anomaly. Instead, it is proposed to be caused by the extent of lattice distortions that can be related to the limited degree of surface diffusion.

## CHAPTER 7: The Effects of increasing Cr concentration on the Structural, Mechanical and Tribological Properties of Stainless Steel-Nitride Thin Films

Chromium nitride, like TiN, is a commonly used hard coating that provides excellent wear resistance in severe operating environments. CrN is also a common component in mixed transition metal hard coatings, such as Ti-Cr-N and TiAlCrN. It is also a component of all stainless steel alloys, including the 304 SS used in this research. However, in stainless steels the chromium concentration is limited to about 18% in order to maintain a single-phase structure and avoid embrittlement by intermetallic phases. Therefore, increasing the Cr content in our coatings can only be accomplished by co-sputtering using Cr and SS targets, in a manner similar to that used for the Ti-SS-N films in Chapter 6. In this chapter, the results on experiments for SS-Cr-N films are presented.

### 7.1 Deposition Parameters and Composition Analysis of SS-Cr-N Films

SS-Cr-N films were deposited using a variety of parameters, as tabulated in Table 7.1. The effects of sputter gun power, substrate temperature, gas composition and substrate bias on the composition of the SS-Cr-N coatings were examined. The power ratio of SS to Cr has a significant effect on the composition of films deposited at 250C with a constant SS power (150W) and various Cr power levels as shown in Table 7.1. An increase in power from 50W to 100W (for SS gun) resulted in a similar N content but the Cr content decreased from 54.51% to 45.02%. Also, increasing the Cr power further to 150W while the SS power kept constant (150W), showed more reduction in the Cr content as well as a decreasing in the N/Metal from 0.68 to 0.55. In contrast, making films with powers of 50W for Cr and 150W for SS could reduce the N/M further to 0.51. These results show that increasing the Cr content above the nominal

concentration found in stainless steels (which would be approximately 9% as an absolute amount in a stoichiometric nitride) increases the nitrogen content in the films only slightly. Therefore, Cr is not as effective a nitrogen-getter as Ti was found to be in Chapter 5.

The effect of varying substrate bias on films deposited at 250C and SS:50W/Cr:150W was tested using bias level of -100V, -120V, -140V and -160V. In general, they showed a nearly similar level of N/M (0.67-0.68) except for -120V which indicated a slightly higher nitrogen/metal ratio of 0.74.

The effect of the substrate temperature on films deposited from 25-350C at SS:50W/Cr:150W and bias of -140V is also studied here. Table 7.1 shows that increasing the temperate from 150 to 250C, does not show a significant increase in the N/M ratio. However, increasing the temperature to 350C indicated a slight reduced in the N/M to 0.64. Overall, the temperature and bias had little effect on the film composition.

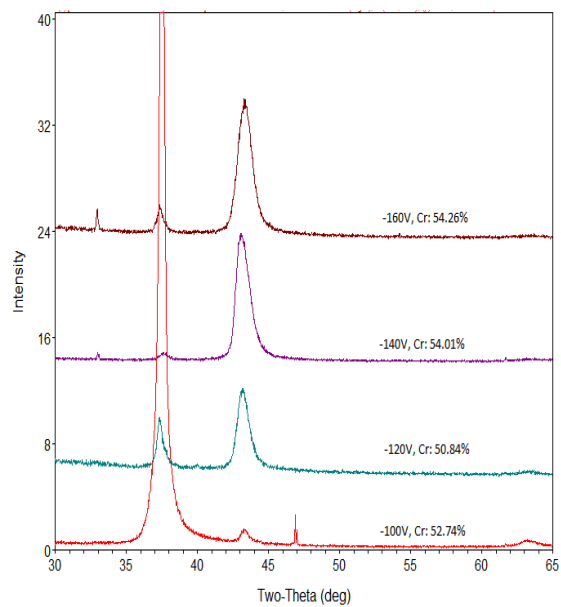
The attempt to incorporate more nitrogen in the film by increasing its concentration in the mixed gas was also studied as indicated in Table 7.1.

	Temperature C°	SS:Cr Power Ratio (Watt)	Depositi on Time	Ar N	Bias (V)	% Fe	% Cr	% Ni	% N	N/ Metal
<b>Effect of Power</b>	250	50:150	3	20 5	140	5	54.01	0.48	40.51	0.68
	250	100:150	3	20 5	140	13.10	45.02	1.44	40.44	0.68
	250	150:150	3	20 5	140	20.77	41.39	2.12	35.71	0.55
	250	150:50	3	20 5	140	35.92	26.87	3.42	33.79	0.51
<b>Effect of Temper ature</b>	150	50:150	3	20 5	140	5.06	54.31	0.48	40.15	0.67
	250	50:150	3	20 5	140	5	54.01	0.48	40.51	0.68
	350	50:150	3	20 5	140	6.23	53.86	0.69	39.22	0.64
<b>Effect of Bias</b>	250	50:150	3	20 5	100	6.25	52.74	0.66	40.36	0.67
	250	50:150	3	20 5	120	6	50.84	0.62	42.54	0.74
	250	50:150	3	20 5	140	5	54.01	0.48	40.51	0.68
	250	50:150	3	20 5	160	4.95	54.26	0.50	40.29	0.67

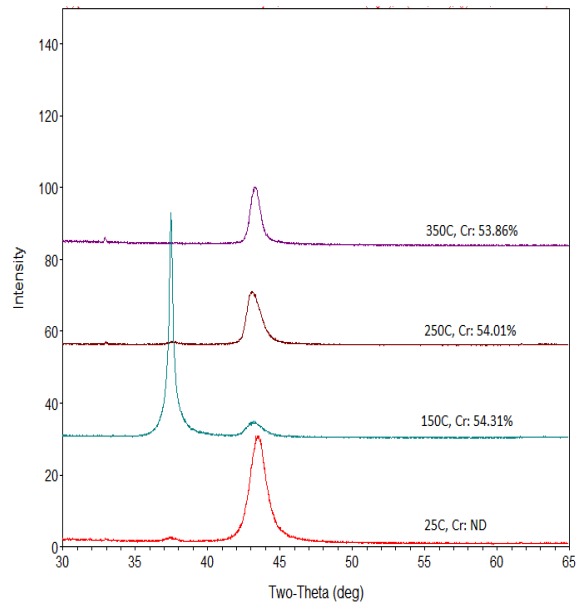
Table. 7.1 The effect of power, substrate temperature and substrate bias on the composition of SS-Cr-N films

## 7.2 XRD Analysis

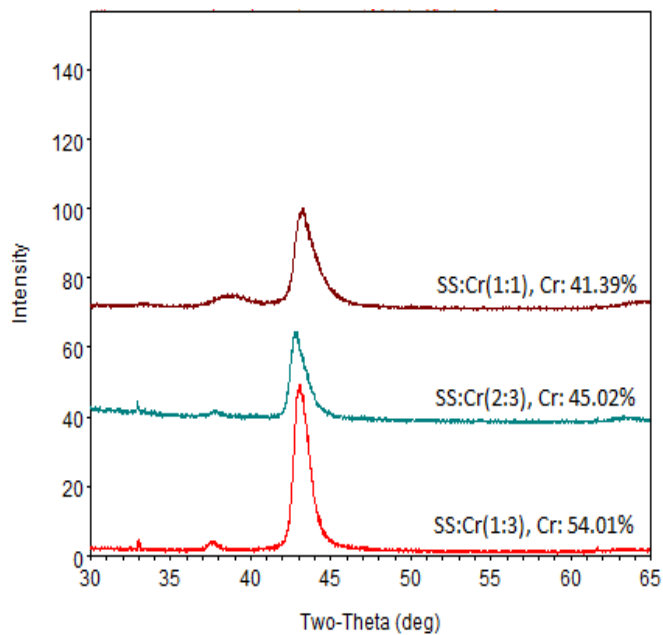
Figures 7.1 a-c show x-ray diffraction patterns of films deposited at different sputter guns power, bias and substrate temperature on SS-Cr-N films. Further analysis of the XRD is shown in Table 7.2. Fig. 7.1(a) shows the influence of applying varied levels of bias between -100 and -160V. Generally, increasing the bias from 100-160V did not significantly effect the R-values. However, the texture of the films was significantly altered; at -100V, the film had a strong [111] texture whereas at higher bias levels the texture switched to [200]. Figure 7.1b shows increasing the substrate bias from room temperature 250C to 250C at a constant power ratio of 50W/150W and bias levels of -140V showed an increase in the R-value from nearly 0.75 to 0.77. In these films the Cr content is still almost constant (54% Cr). The film texture was varied with one film showing a strong [111] texture (at 150C) and the remaining films having a [200] texture. The effect of applying different power ratios is shown in fig. 7.1(c) for films deposited at a constant substrate temperature (250C) and bias (-140V). The S-phase has been observed in these films using X-ray diffraction. Films with lower nitrogen concentration have displaced (200) peaks to higher  $2\theta$  angles while films with higher nitrogen contents shifted the (200) peaks to lower  $2\theta$  angles, indicating a larger lattice constant. In addition, films with higher Cr contents (54.01%) indicated lower R-value. However, increasing the ratio of stainless steel power to the Cr power led to a decreasing Cr content, from 54 to 41.39%, and an increase in R-value from 0.77 to 0.81.



(a)



(b)



(c)

7.1: X-ray diffraction patterns showing the effect of (a) bias, (b) temperature and (c) gun power ratio on the structure and texture of the deposited films.

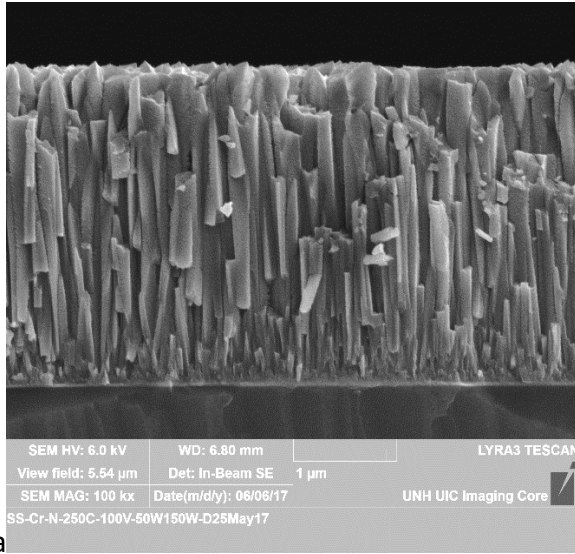
	Temp C°	SS Power	Cr Power	Bias	2θ d <sub>111</sub> , nm	2θ d <sub>200</sub> , nm	% N <sub>2</sub>	% Cr	a <sub>111</sub> , nm	a <sub>200</sub> , nm	R
Effect of Power	RT	150	150	140	37.317 d=0.24077	43.48 d=0.20797	ND	ND	0.417	0.416	0.7460
	250	50	150	140	37.563 d=0.23925	43.067 d=0.20986	40.51	54.01	0.414	4.20	0.769
	250	100	150	140	37.86 d=0.23744	42.771 d=0.21125	40.44	45.02	0.411	0.423	0.792
	250	150	150	140	38.835 d=0.2317	43.294 d=0.20882	35.71	41.39	0.401	0.418	0.812
	250	150	50	140	39.019 d=0.23065	43.596 d=0.20744	33.79	26.87	0.403	0.415	0.801
Effect of Tempera ture	RT	50	150	140	37.428 d=0.24009	43.591 d=0.20746	ND	ND	0.416	0.415	0.7466
	150	50	150	140	37.490 d=0.23970	43.184 d=0.20932	40.15	54.31	0.415	0.419	0.7489
	250	50	150	140	37.563 d=0.23925	43.067 d=0.20986	40.51	54.01	0.414	4.20	0.769
	350	50	150	140	ND	43.283 d=0.20887	39.22	53.86	ND	ND	ND
Effect of Bias	250	50	150	100	37.542 d=0.23938	43.374 d=0.20845	40.36	52.74	0.415	0.417	0.758
	250	50	150	120	37.348 d=0.24058	43.111 d=0.20966	42.54	50.84	0.417	4.19	0.759
	250	50	150	140	37.563 d=0.23925	43.067 d=0.20986	40.51	54.01	0.414	4.20	0.769
	250	50	150	160	37.371 d=0.24044	43.377 d=0.20844	40.29	54.26	0.416	4.17	0.7515

Table 7.2: The interplanar spacing lattice constant values

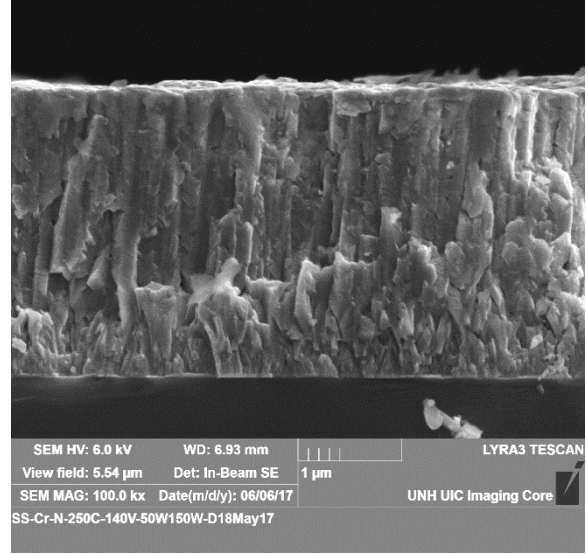
ND= not detected

### 7.3 Microstructural Characterization

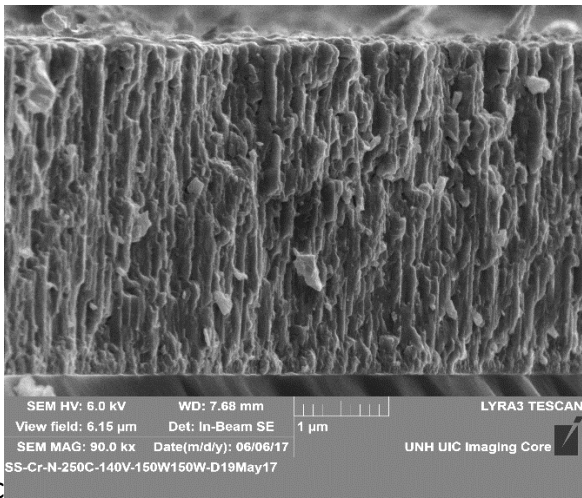
SEM cross-section of SS-Cr-N films were examined as shown in Figures 7.2 a-d. Fig. 7.2 (a), shows a film deposited at 250C-100V and SS:Cr ratio of 1:3. This film shows a columnar structure, whereas increasing the bias as indicated in fig. 7.2 (b) further to -140V led to a denser structure. Fig. 7.2 (c), shows film deposited at equal SS and Cr sputter power guns (at 150W) and 250C/-140V. In this image the structure is somewhat fibrous. It should be noted that the thickness of this film is about 3900nm which the highest thickness observed while other films have thickness between 2700-3000nm. Figure 7.2 (d) indicates that increasing the substrate temperature to 350C with the same deposition conditions of fig. 7.2 (c) shows columnar and faceted structure.



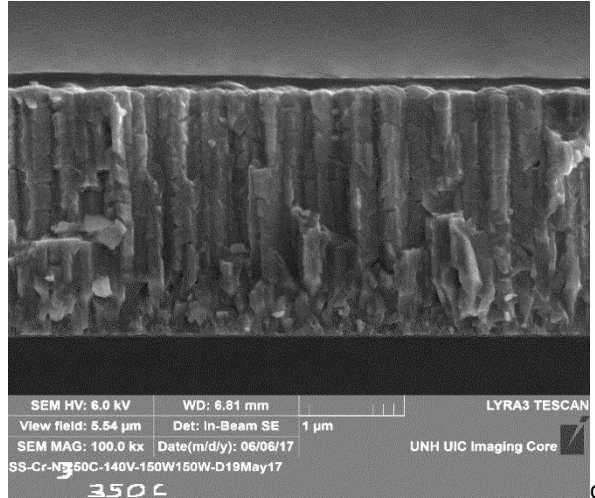
a



b



c



d

Figure 7.2 SEM cross-section images for films: (a) 250C, -100V, (SS:1/Cr:3) (b) 250C, -140V, (SS:1/Cr:3) (c) 250C, -140V, (SS:1/Cr:1) and (d) 350C, -100V, (SS:1/Cr:1).

#### 7.4 Mechanical and Tribological properties of SS-Cr-N

Knoop hardness test using micro-indenter was used to measure the hardness of the coated films applying a 10-gram load. The effect of films deposited at different power ratios on the SS-Cr-N films are shown in Figure 7.3. The effect of substrate temperature is shown in Fig. 7.3(a) for a constant bias of -140V and power ratio of 50SS/150Cr. The film with substrate temperature of 250°C had the highest hardness with a value of nearly 4639 kg/mm<sup>2</sup>. The effect of depositing films at bias varied between -100V and -160V at a constant substrate temperature of 250C and 50/150W power ratio is shown in Fig. 7.3(b) and shows a peak hardness (of 4639 kg/mm<sup>2</sup>) was obtained at -140V, and then declined at -160V to a value of 2566.42 Kg/mm<sup>2</sup>. Fig. 7.3(c) shows the effects of power ratio. The data point at a power ratio of zero represents a CrN films, which had a hardness of 2566 kg/mm<sup>2</sup>. A small increase in the SS content had a dramatic increase in hardness, and then further increases in SS reduced hardness. The last value shown at a power ratio of 3.0 had a hardness similar to the SS-N films examined in Chapter 4.

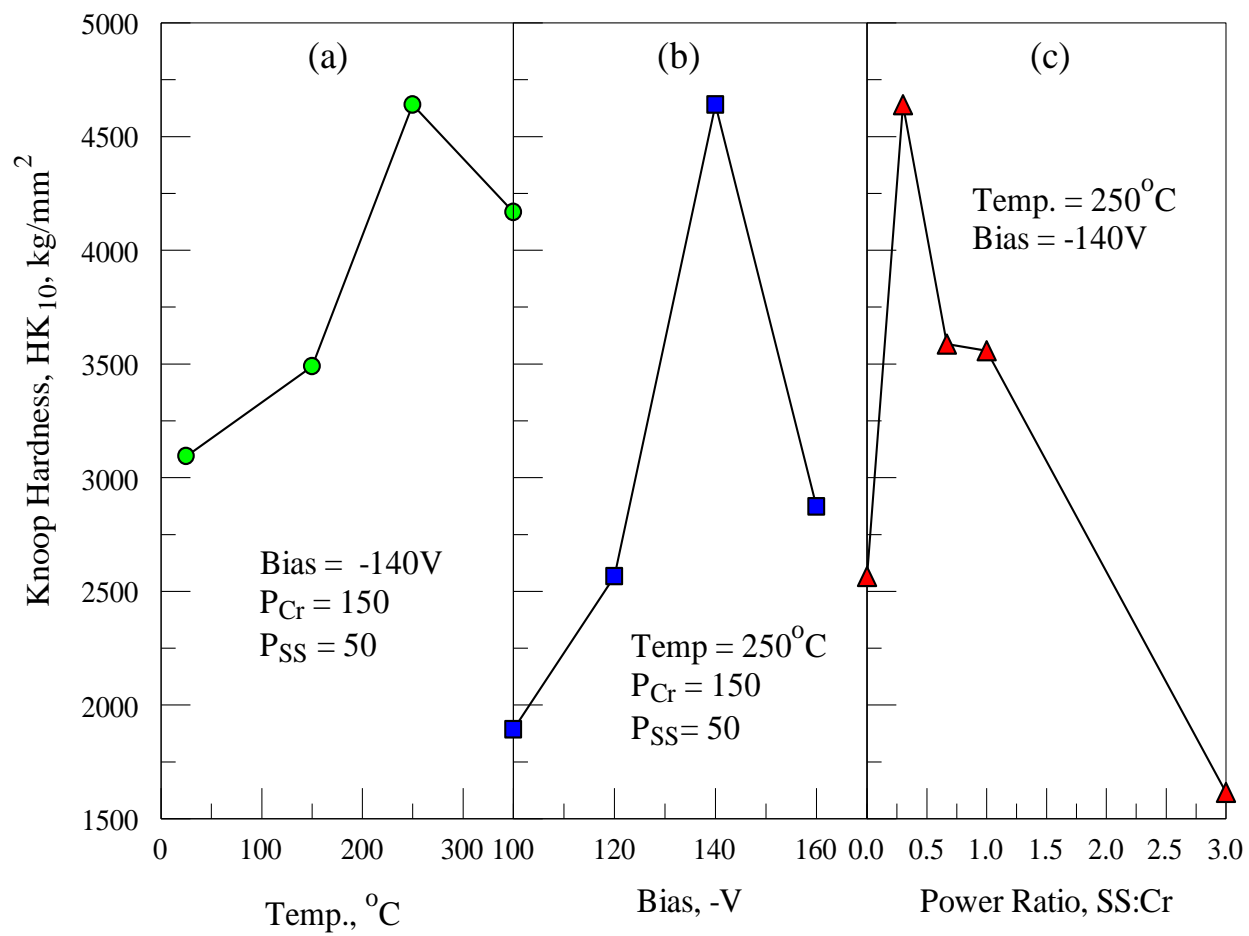


Fig. 7.3: The hardness of SS-Cr-N films deposited at different effects (a) effect of substrate temperature; (b) effect of varied bias; (c) effect of applying different power ratio.

The tribological behavior of SS-Cr-N films was examined by pin-on-disk testing at room temperature. An alumina ball (6.25 mm diameter) was utilized as the counterface. A 100g (1N) load was applied, and the sliding track was rotated at 200 rpm and the coated disks were run to reach nearly 4500 cycles. Fig. 7.4 shows that the tribological properties of the SS-Cr-N films deposited at a constant power ratios of 50W/150W and different temperature and bias levels. The results are also tabulated in Table 7.3, showing the average, maximum, minimum and standard deviation in friction values. The film which was grown at 150C and -140V displayed the lowest average of the friction coefficient obtained in this study (0.35). Increase the deposition temperature to 250C at the same bias showed a higher friction. It is interesting to note that the friction coefficient higher in the latter film even though it had a higher hardness in comparison to the 150C film. Moreover, reducing the bias to -100V showed an even a worse result and this might be because this coating has a much lower hardness compared to the other films. Increase the substrate temperature further to 350C showed an improved friction coefficient with an average of 0.36.

The wear track was observed after the pin-on-disk tests as shown in Fig. 7.5 (a-d) which shows optical microscopy images of the wear tracks of films deposited from 150-350C at -100V and -140V. Figures 7.5a and 7.5d which indicated the improved friction coefficient, showed uniform wear tracks. In these two images, there are spots on the coatings which are related to film defects. These spots also shown in the wear tracks as well, indicating the coating is still present in the wear tracks. The wear track in Fig. 7.5(b) show the film has worn off and this is consistent with the high friction coefficient (0.53) as shown in Table 7.3.

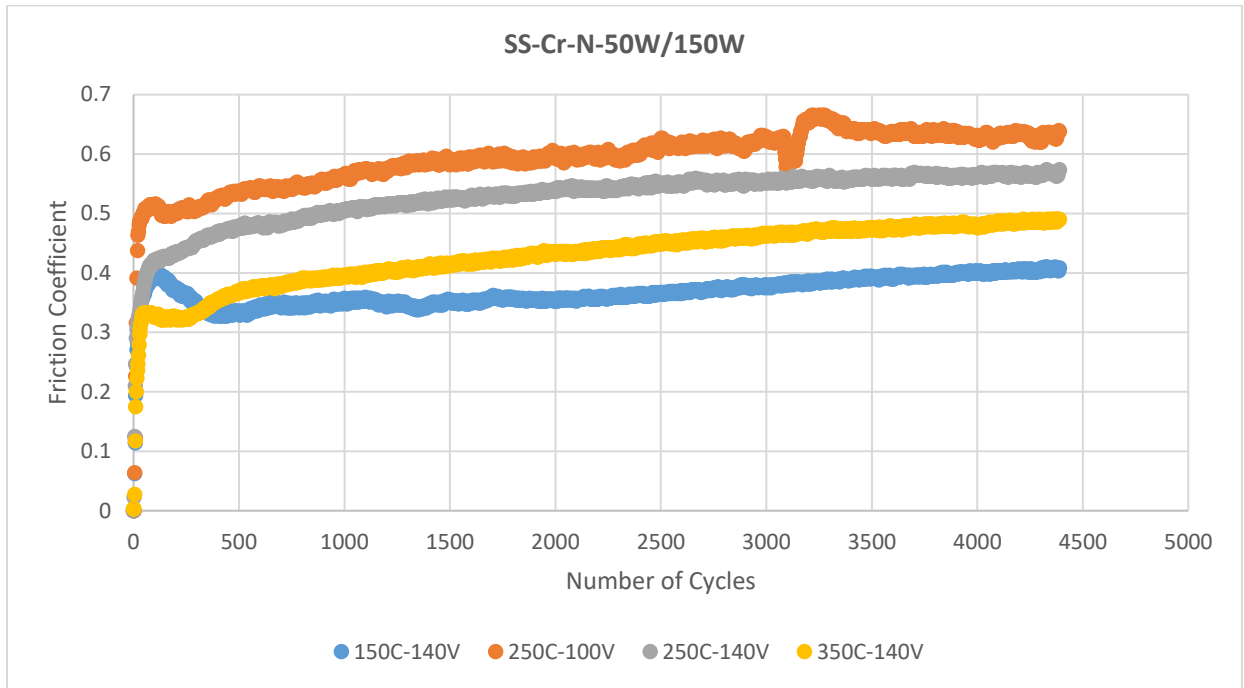


Figure 7.4: The friction coefficient of the SS-Cr-N films deposited at 150C-350C with bias varied between -100-140V and a constant SS/Cr sputter guns power of 50W/150W

Sample	$\mu$ (average)	$\mu$ (max)	$\mu$ (min)	Std. dev
150C-140V	0.35	0.339	0.327	0.018
250C-100V	0.53	0.56	0.495	0.019
250C-140V	0.47	0.51	0.38	0.028
350C-140V	0.36	0.395	0.32	0.026

Table 7.3: Pin-on-disk friction test results of SS-Cr-N selected films



Figure 7.5a SS-Cr-N-150C-140V-50W150W

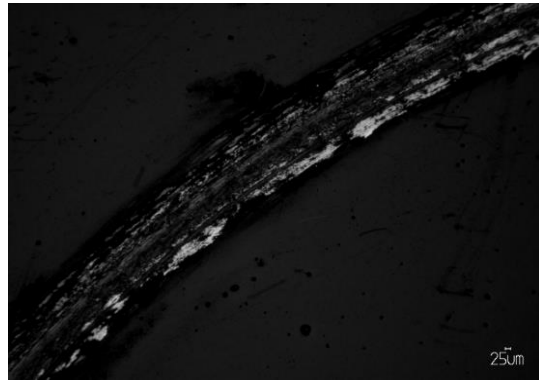


Figure 7.5b SS-Cr-N-250C-100V-50W-150W

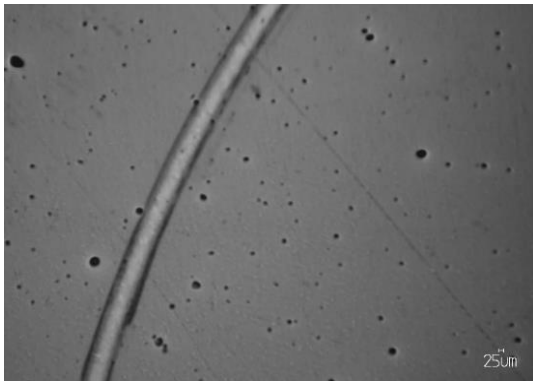


Figure 7.5c SS-Cr-N-250C-140V-50W150W

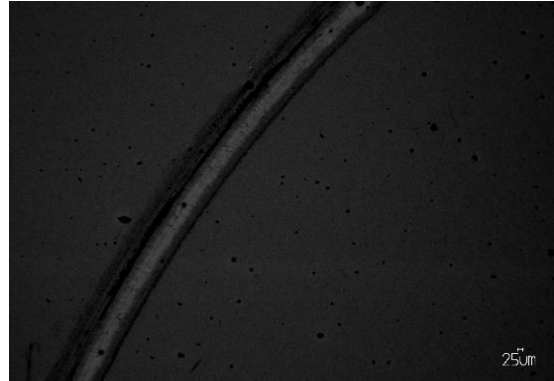


Figure 7.5d SS-Cr-N-350C-140V-50W150W

Fig. 7 (a-d) SEM cross-section

## 7.6 Summary and Conclusions

Nitrogen containing 304 austenitic stainless steel and chromium targets were used to co-deposit SS-Cr-N films onto silicon substrates by reactive magnetron sputtering. The effect of power, substrate temperature, and substrate bias on SS-Cr-N coatings were evaluated in order to enhance the mechanical and tribological properties of the stainless steel. X-ray diffraction presented that SS-Cr-N structure is nominally FCC but the (200) peak shifted to higher  $2\theta$  angles in samples where the N content is below about 40%. Chromium concentrations up to 54% were

observed and showed a very high hardness for several SS-Cr-N films a with hardness maximum of ~ 4639.8 Kg/mm<sup>2</sup> at 250C/-140V. These films contain nitrogen concentrations of about 40%. The friction coefficient of the coated films were examined and showed an improved friction coefficient (0.35) for a film deposited at 150C/-140V.

## CHAPTER 8: Expanded Austenite in Stainless Steel Carbide

### 8.1 Film Composition Analysis of SSC

Stainless steels-carbon (SSC) films were deposited by a variety of conditions as shown in Tables 8.1 and 8.2. These films are tabulated into 3 groups according to common sputter gun power levels. Within each group the substrate temperature is varied but the bias used for all films was constant at -140V. These films were deposited at a targets-to-substrate distance of 9cm and a deposition time of 3h. The carbon contents of the deposited films were determined by XPS, and the C/M (M: metal) is calculated as shown in the tables. Note that the metal concentrations are not specifically listed, but the metal fraction can be divided into the nominal alloy proportions for 304 stainless (0.74 Fe, 0.18 Cr and 0.08 Ni).

The first group of films was deposited from room temperature to 450C and gun power levels of 150W and 50W for the stainless steel and carbon sputter guns, respectively (C/SS power ratio of 0.33). Table 8.1 shows that increasing the substrate temperature first led to an increase in the carbon content up to 350C which has the highest C/M level in this group (0.33), after which there is a sharp decline at 450C. Group 2 shows films deposited at SS: 75W and C: 150W (C/SS power ratio = 2) and at different substrate temperature. Overall, the carbon concentration was higher in these films, and increasing the deposition temperature from 25-250C led to a slight increase in the carbon concentration in the films, which peaked at 250C and declined slightly at 350C (although these differences are close to the accuracy expected in XPS analysis).

The effect of increasing the power from 25-150W at a constant substrate temperature 250C is shown in the third group as shown in table 2. This set shows an increase in the power of the carbon target to the stainless steel target from 25-50W led to an increase in the Carbon content from 16.58 to 19.23%. After that when the carbon power was more increased to 100W, the carbon content started to be decreased while increasing the power to 150W made the carbon content to increase again to reach 37.08 at%. C.

<b>Temp., °C</b>	<b>At.% C</b>	<b>C/Metal</b>
<b>Group 1: -140V Bias, SS:150W, C:50W</b>		
<b>25</b>	13.03	0.15
<b>250</b>	19.23	0.24
<b>350</b>	24.89	0.33
<b>450</b>	18.35	0.22
<b>Group 2: -140V Bias, SS:75W, C:150W</b>		
<b>25</b>	44.37	0.79
<b>150</b>	46.06	0.85
<b>250</b>	52.45	1.10
<b>350</b>	50.63	1.06

Table 8.1: Deposition Parameters and Carbon Content for SS-Carbon Films for states 1 and 2

<b>Power, W</b>	<b>At.% C</b>	<b>C/Metal</b>
<b>Group 3: -140V Bias, SS:150W, 250C</b>		
<b>25</b>	16.58	0.19
<b>50</b>	19.23	0.24
<b>100</b>	10.44	0.12
<b>150</b>	37.08	0.59

Table 8.2: Deposition Parameters and Carbon Content for SS-Carbon Films; state 3

## 8.2 XRD Results

Fig. 8.1 shows the XRD results for SS-carbon films deposited from room temperature to 450C at -140V and constant SS and C power levels of 150W and 50W, respectively. For films deposited from 150C-350C, the structure is consistent with an fcc-based phase. As the temperature increases, the lattice constant decreases, but the structure is maintained up to 350°C. In general increasing the substrate temperature leads to an increase in the  $2\theta$  angle of the (111) and (200) peaks. Also, the peak position of the (111) peak is near 44-45°  $2\theta$ , which corresponds to a lattice parameter of 0.349-0.356 nm, considerably lower than that found for SS/nitrogen films which were near 0.4 nm. In fact, the lattice constant for these SS-C films is close to that found for austenitic stainless steels without carbon. At 450°C, the formation of iron carbide and possibly nickel are observed.

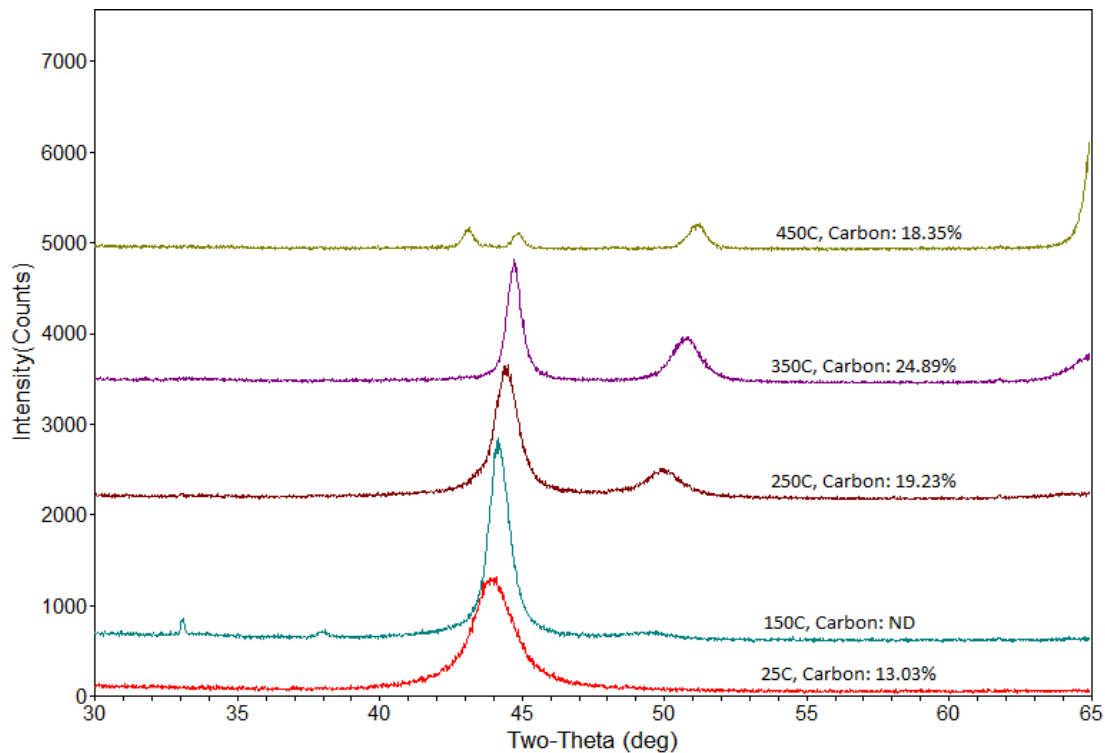


Figure 8.1: XRD diffraction patterns for SS-carbon films deposited at -140V bias and temperature ranging from 25-450C (state 1).

Figure 8.2 indicates XRD scans for SSC films (state 2) deposited to reach high carbon near stoichiometric where C/Metal is nearly 1. Possible matches include iron carbides (FeC), chromium carbide (CrC) and nickel (Ni) are found in this state. As shown in the graph as the temperature increases, the films showed more phases including FeC, CrC, and Ni.

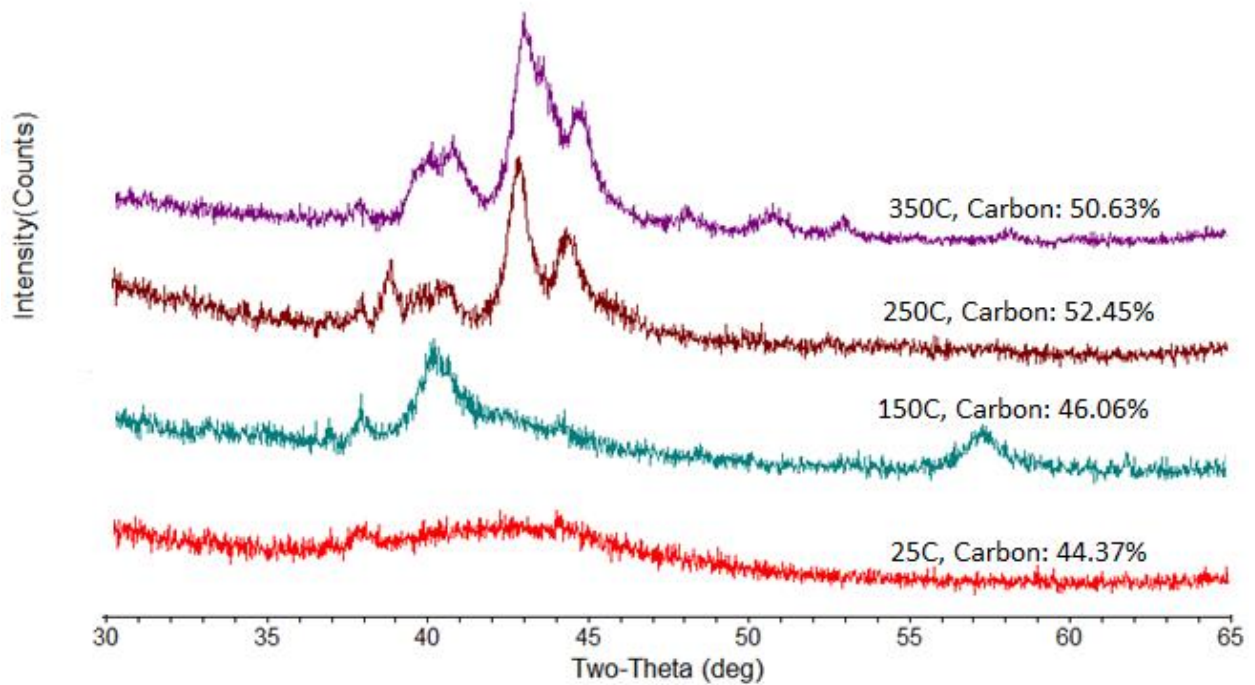


Figure 8.2: XRD diffraction patterns for SS-carbon films deposited at -140V bias. As the temperature increases, the films showed more phases including FeC, CrC and Ni.

Furthermore, the crystal structure of the SSC was also studied for the third state as shown in graph 8.3 where films deposited at a constant substrate temperature 250C and varied carbon gun power from 25W-150W. S-phase was determined at films fabricated at 25W, 50W and 100W. Also, (111) and (200) reflection peaks were not shifted when the power was increased. In fact, the film deposited at a carbon power of 150W, the film doesn't show S-phase, and this is might be as a result of the high carbon content that this coating had.

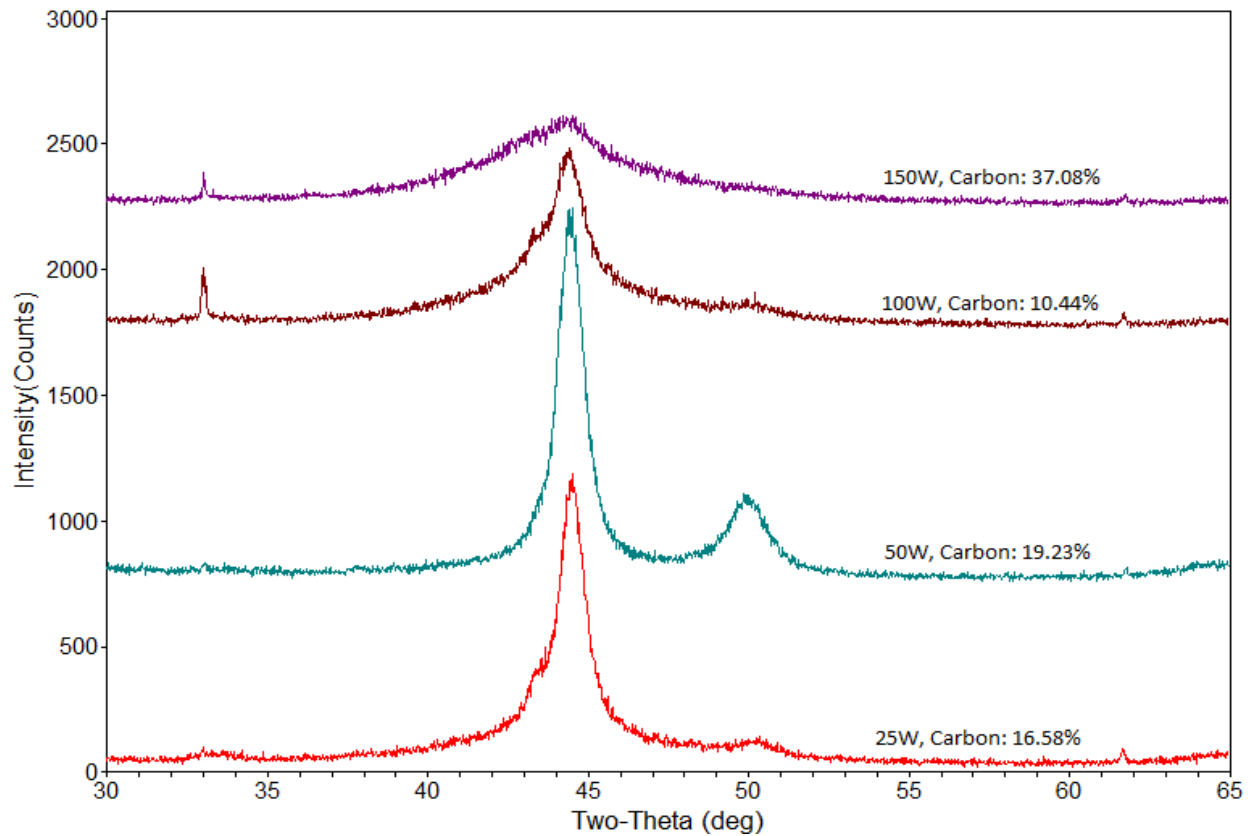


Figure. 8.3: SSC films deposited at a 250C and varied carbon power ranging 25W-150W with keeping the stainless steel sputter gun power at 150W.

### 8.3 Mechanical Properties

Fig. 8.4 shows the Knoop hardness of stainless steels-carbide (SSC) films deposited at states 1 and 2. For state 1, the hardness remains constant from room temperature to 250C, and then increases at 350C to reach a value of 1700 Kgf/mm<sup>2</sup>. It should be noted that 350C has the highest carbon content (24 at. %) in this series. At 450C there is a sharp decreasing in the hardness, possible due to the formation of iron carbide. Additional films were deposited at a power ratio of SS: 75/C: 150W, and are shown in Fig. 8.4 as state 2. The hardness increases when the substrate temperature increases until reaches a hardness of 2256 Kg/mm<sup>2</sup> at 250°C thereafter decreases slightly. A previous study of stainless steel/C samples reported hardness level of about 1400 Kgf/mm<sup>2</sup>, but in this study, the hardness for the SS-C films has been strongly increased in comparison.

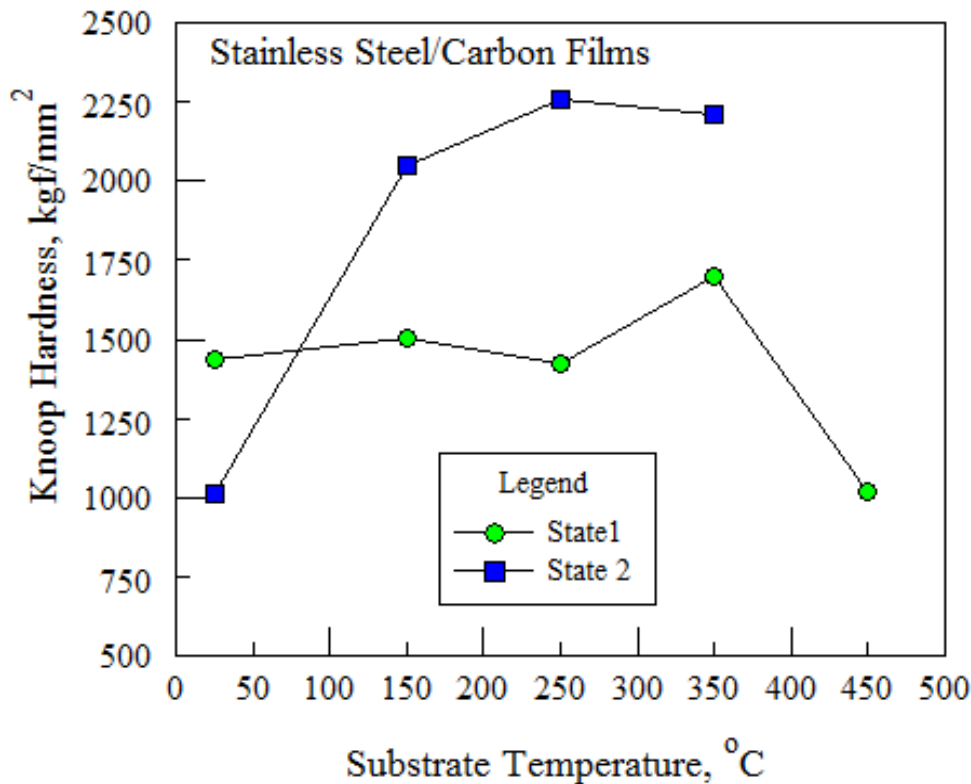


Figure 8.4: Hardness data for SS-carbon films. The higher hardness levels observed in state 2 films were due to higher (near 50 at. %) concentrations of carbon in the films.

Fig. 8.5 shows the Knoop hardness of SCC for films deposited at different powers ranging from 25W to 150W at a constant substrate temperature 250C. The hardness increases with increasing the power from 25W-100W. However, the film with equal stainless steel and carbon powers (150W for each sputter gun) shows a sharp decreasing in the hardness with a value of 1277.13 Kg/mm<sup>2</sup>. This film has the highest carbon content in state 2 with 37.08 at. %.

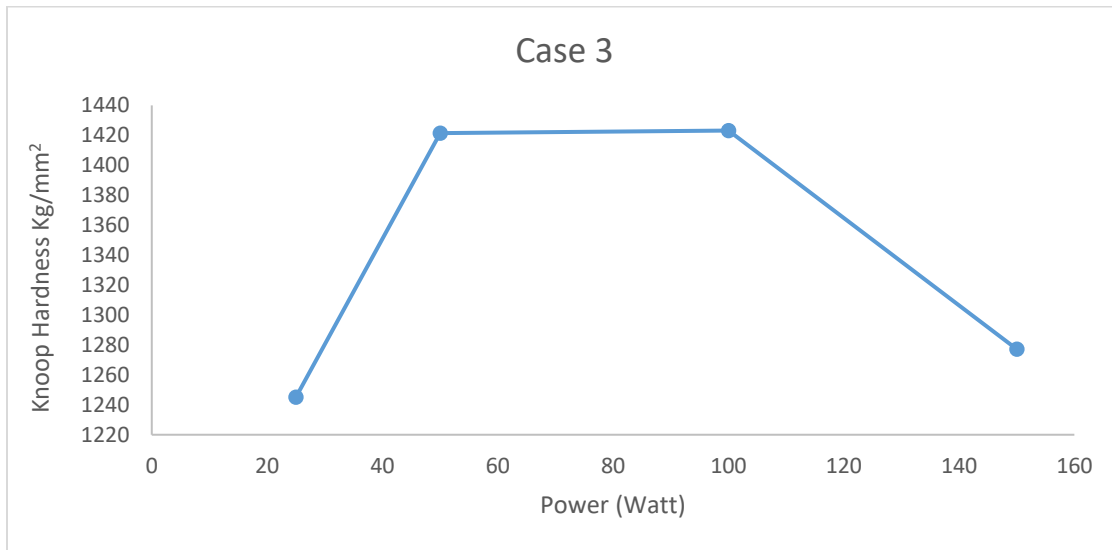


Figure 8.5.: The Knoop hardness of SCC for films deposited at state 2 where films deposited at powers varied between 25W and 150W as a function of the Knoop hardness.

#### 4 Discussion

Films of stainless/steel carbon have been deposited by co-sputtering. Three states were examined in order to study the composition, structure and enhance the hardness of these films. X-ray diffraction showed the structure maintained S-phase when these films have carbon contents between 10-19% as seen in most deposited films in states 1 and 2. In state 1 which is seen in graph 8.1, increasing the substrate temperature for films deposited from room

temperature to 350C showed an increasing in the  $2\theta$  angle of the (111) and (200) reflection peaks. Furthermore, increasing the temperature further to 450C multiple phases were obtained where the film contains FeC, CrC and Ni. State 2 has carbon contents near stoichiometric where these films don't include S-phase. In fact, these films show multiple phases. The effect of applying different power at a constant substrate temperature 250C and stainless steel power of 150W was studied as shown in graph 8.3 (state 3). These films maintain S-phase at films deposited from 25W-100W. At C: 150W the film contains multiple phases (FeC, CrC and Ni) and this is because this film has a high carbon content (37.08 at. %).

The hardness of the SSC films also examined. State 1 showed that increasing the substrate temperature led to an increase in the hardness up to 350C where this film has the highest hardness in this state nearly 1700 Kg/mm<sup>2</sup>. Increasing the temperature further to 450C made the hardness to start sharply decreasing which has a hardness of 1015.58 Kg/mm<sup>2</sup>. The higher hardness levels are observed in state 2 where these films have carbon concentration of nearly 50 at. %. State 3 showed almost a stable hardness level with increasing the power from 25-150W where the observed hardness is between 1200-1400 Kg/mm<sup>2</sup>.

## 8.5 Conclusions

Stainless steel co-sputtered with carbon (SSC) films were studied at varied substrate temperature, bias, and power. These films maintained S-phase structure when deposited below 450°C as well as having carbon contents <25% but the lattice constant is close to that of the austenite stainless steel that deposited without carbon. In these films, It was found that increasing the substrate temperature led to an increasing in the (111) and (200) peaks. Higher concentrations of carbon near 50% were obtained in several cases results in Fe/Cr carbide formation. These films tended to have the highest hardness amongst the three SSC states and reached a maximum of over 2200 kgf/mm<sup>2</sup>. The best film observed in this study is the film that deposited at SS: 75W and C: 150W where the obtained hardness was 2256.05 Kg/mm<sup>2</sup>. Films that contain S-phase structure has a hardness level of about 1700 Kgf/mm<sup>2</sup>.

## Chapter 9: Summary and Conclusion

Reactive magnetron sputtering was used to deposit coatings from a 304 stainless steel target (nominal composition 18%Cr, 8% Ni, balance Fe). Deposition was carried out in a mixed argon/nitrogen atmosphere. Co-sputtered of SS-Ti-N, SS-Cr-N and SS-C were also deposited with the same method. Results of the work are summarized shown below:

1- SSN films were deposited in a mixed argon/nitrogen atmosphere with Ar:N<sub>2</sub> ratios of 4, 1.5 and 1, and a total gas flow of 25 sccm for all cases. Substrate temperatures ranged from 150 to 600°C, along with substrate bias levels from -100V to -140V.

XPS determined that the nitrogen content increases with increasing the nitrogen in the gas composition. Also, XPS found that increasing the substrate temperature reduced the nitrogen content. However, increasing the bias only slightly decreased the nitrogen content. XRD analyses showed the structure of the coatings were strongly temperature dependent: above 450°C, the films were a mixture of CrN, bcc-Fe and Ni; below 450°C the S-phase (a N-supersaturated fcc structure) was observed and show the typical FCC pattern with a slightly displaced (200) peak. The shift of the (200) peak is decreased with increasing tilt of the surface plane.

SEM cross-sections for samples deposited below 450°C, where the S-phase was found, had discontinuous, angular crystallites, whereas at higher substrate temperatures the structure had the appearance of a loose particle aggregate. At higher nitrogen has concentrations (Ar:N<sub>2</sub> of 1:1) a more typical columnar structure was found. TEM cross-sections showed a mosaic structure in coarse columns which is an uncommon observation for the film morphology. In addition, Hardness testing of the film deposited at 25°C and -140V bias gave a value of 2100 kg/mm<sup>2</sup>.

2- SS-Ti-N coatings were studied for the purpose of examining the mechanical and tribological properties of stainless steel films deposited to incorporate large concentrations of nitrogen along with varying amounts of titanium. Deposition was carried out using magnetron co-sputtering of stainless steel and titanium from separate targets in a mixed Ar/N<sub>2</sub> gas. Titanium levels of up to ~14 at. % was obtained with near 46 at. %. X-ray diffraction showed that the films all had a nominally f.c.c. structure with no additional phases, but sub-stoichiometric films had an S-phase structure whereas stoichiometric films had TiN-type rocksalt structure. The stoichiometric films also had a superior hardness 18-24 GPa (1800-2447 Kg/mm<sup>2</sup>) compared to the sub-stoichiometric films. A tribological analysis of the films was conducted using a pin-on-disk test with an alumina ball, and the best results were obtained on a stainless-steel/Ti/N film deposited at 150°C and -140V bias, where the average friction coefficient was 0.39.

3- Thin films of AISI 304 stainless steel nitrides selected from chapter 4 and nitrogen-containing stainless steels co-sputtered with titanium selected from chapter 5 were deposited onto silicon substrates by magnetron sputtering in a mixed argon/nitrogen gas atmosphere. The effects of nitrogen and titanium concentrations, substrate temperature and substrate bias were examined. The structural nature of the films was assessed using a term  $R = [\sin^2(\theta_{111})/\sin^2(\theta_{200})]$ , which nominally has a value of 0.75 for fcc-structured films; however, films in the present study had S-phase structures with R-values of up to 0.818. The higher R-values generally correlated with the degree of sub-stoichiometric nitrogen concentrations in the films, but for substrate bias levels of 60-140V, the R-values decreased with increasing substrate temperature. The addition of titanium to the films by co-sputtering showed that with

a sufficient amount (~10-14 at.% Ti), stoichiometric levels of nitrogen were obtained and giving  $R = 0.75$ . However, films which had Sub-stoichiometric levels of nitrogen concentrations showed higher R-values ( $>0.75$ ). In addition, the relationship between increasing R-values and decreasing nitrogen content was weak. The correlation of R-value to the substrate temperature for films deposited without or with lower titanium contents was obtained and showed that increasing the deposition temperature led to a decrease in the R-value. In contrast, R-values for films with higher Ti content were independent of the substrate temperature. The effect of the bias was investigated and showed that the nitrogen concentration in the coated films decreased with increasing bias, and the R-value decreased when deposited films from -60 to -100V then followed by an increase in R-value when deposited at -140V. The effect of the morphology on R-value was examined but could not consistently explain the R deviations. Instead, a structure is proposed involving lattice distortions due to the high concentrations of vacancies on the interstitial sublattice was proposed. SEM cross-section studies of films deposited at low Ti concentrations (3-5.24 at.% Ti) showed a coarsening structure with increasing the substrate temperature as well as voided, faceted columnar structure. TEM images revealed that a faceted, dendritic structure was observed for films fabricated at 150C and 250 °C with less branches at 350C. Additionally, increasing the substrate temperature from 150-350 °C which led to a decrease in the R-value, gave the structure of the films higher densities. The effect of the stacking fault density of the layered morphology, which were observed in the SEM and TEM images, was examined. According to Warren, the presence of stacking faults will shift Bragg peaks from their expected values. The determined number ( $\Delta 2\theta = 0.022^\circ$ ) did not agree with the value of  $\Delta 2\theta$  that measured from our XRD ( $\Delta 2\theta=1.4^\circ$ ) results. Based on the XRD

results, high stacking faults should be seen in the TEM images. Instead, TEM images showed dendritic pattern structures which is due to the limited amount of surface diffusion as reported in the literature.

4- Nitrogen infused- co-sputtered of 304 austenite stainless steel and chromium (SS-Cr-N) were deposited under a multiplicity of deposition conditions and substrate temperatures. Effect of applying different power, substrate temperature, gas composition and substrate bias on of the SS-Cr-N coatings were evaluated in order to improve the mechanical properties and the wear resistance of the films. X-ray diffraction showed that SS-Cr-N structure is basically FCC but the (200) peak diffracted at higher angles. Chromium concentration up to 54% was observed and showed a very high hardness at several SSS-Cr-N films with a maximum hardness observed of  $\sim 4639.8 \text{ Kg/mm}^2$  at 250C and -140V bias. These films tend to have a nitrogen concentration of  $\sim 40\%$ . The friction coefficient of the SS-Cr-N coated films was examined and showed an improved friction coefficient (0.35) for a film deposited at 150C/-140V.

5- Co-deposition of Stainless steel/Carbon films (SS-C) using carbon target in Argon (Ar) atmosphere were studied at a variety of parameters. In general, increasing the deposition temperature led to an increase in the carbon concentration in the films and a maximum percentage of 52% were obtained for a film deposited at 250C/-140V. XRD results showed S-phase could be produced when films have carbon concentrations between 10-19%, whereas films near stoichiometric showed multiple phases include FeC, CrC and Ni. The Knoop hardness showed SSC films that maintained S-phase structure had a hardness level of  $1700 \text{ Kg/mm}^2$

while films near 50 at. % concentration showed a very high level hardness of nearly 2256 Kgf/mm<sup>2</sup>.

## References

- [1] E.C. Bain, W.E. Griffiths, An introduction to the iron-chromium-nickel alloys, Trans. AIME 75(166), 166-211, (1927)
- [2] J.R. Davis, ed., Stainless steels, ASM international, (1994)
- [3] C.H.M. Jenkins, et al., Some alloys for use at high temperatures. Part IV: The constitution of the alloys of nickel, chromium and iron, J. Iron Steel Inst. 136, 187-220, (1937)
- [4] H.H. Uhlig, The corrosion handbook, J. Wiley, (1948)
- [5] F.B. Pickering, Physical metallurgy and the design of steels, Applied Science Publishers, (1978)
- [6] B. Laffler. Stainless-Steel and their Properties, *Stainless Steel and their Properties*" (1999).
- [7] [https://books.google.com.sa/books?id=TBtQGBvEXawC&pg=PT13&lpg=PT13&dq=P.+Monnartz+percentage+of+chromium&source=bl&ots=yhc5Agcl8L&sig=EitYSAXTIDX2hZlelUqP3Hzm\\_9c&hl=ar&sa=X&ved=0ahUKEwj5loawsrrQAhUK0WMKHV73B94Q6AEIGzAA#v=onepage&q=P.%20Monnartz%20percentage%20of%20chromium&f=false](https://books.google.com.sa/books?id=TBtQGBvEXawC&pg=PT13&lpg=PT13&dq=P.+Monnartz+percentage+of+chromium&source=bl&ots=yhc5Agcl8L&sig=EitYSAXTIDX2hZlelUqP3Hzm_9c&hl=ar&sa=X&ved=0ahUKEwj5loawsrrQAhUK0WMKHV73B94Q6AEIGzAA#v=onepage&q=P.%20Monnartz%20percentage%20of%20chromium&f=false)
- [8] P. Monnartz, Iron-chromium alloys with special consideration of resistance to acids, Metallurgie 8, 161-176, (1911)
- [9] F. Cardarelli. Materials handbook: A concise desktop reference, Springer Science & Business Media, (2008)

- [10] <http://www.pennstainless.com/stainless-grades/precipitation-hardening/>
- [11] <http://www.imoa.info/molybdenum-uses/molybdenum-grade-stainless-steels/duplex-stainless-steel.php>
- [12] P. Marshall, Austenitic stainless steels, Microstructure and mechanical properties, Springer Science & Business Media, (1984)
- [13] [http://www.msdspring.com/Technical/reference/17-7ph\\_techsummary.pdf](http://www.msdspring.com/Technical/reference/17-7ph_techsummary.pdf)
- [14] <http://www.pennstainless.com/stainless-grades/precipitation-hardening/>
- [15] E. Menthe, K.-T. Rie, J.W. Schultze, S. Simson, Structure and properties of plasma-nitrided stainless steel, Surf. Coat. Technol., 412, 74-75, (1995)
- [16] H. Dong, et al., Improving the erosion–corrosion resistance of AISI 316 austenitic stainless steel by low-temperature plasma surface alloying with N and C, Materials Science and Engineering A 431.1, 137-145, (2006)
- [17] <http://www.bssa.org.uk/topics.php?article=183>
- [18] <http://www.outokumpu.com/en/products-properties/more-stainless/the-effects-of-alloying-elements%E2%80%8B/pages/default.aspx>
- [19] [http://www.ssina.com/overview/alloyelements\\_intro.html](http://www.ssina.com/overview/alloyelements_intro.html)
- [20] <http://www.worldstainless.org/Files/issf/non-image-files/PDF/TheStainlessSteelFamily.pdf>
- [21] N. Yasumaru, Low-temperature ion nitriding of austenitic stainless steels, Materials Transactions, JIM 39(10), 1046-1052, (1998)

- [22] Z. Cheng, et al., Low temperature plasma nitrocarburising of AISI 316 austenitic stainless steel, *Surface and Coatings Technology* 191(2), 195-200, (2005)
- [23] S.R. Meka, A. Chauhan, T. Steiner, E. Bischoff, P.K. Ghosh, E.J. Mittemeijer, Generating duplex microstructures by nitriding: Nitriding of iron based Fe–Mn alloy, *Materials Science and Technology* 1743284715Y.000, (2015)
- [24] W. Liang, et al., Characteristics of low pressure plasma arc source ion nitrided layer on austenitic stainless steel at low temperature, *Thin Solid Films* 391(1), 11-16, (2001)
- [25] O. Ozturk, D.L. Williamson, Phase and composition depth distribution analyses of low energy, high flux N implanted stainless steel, *J. Appl. Phys.* 77, 3839, (1995)
- [26] E. Menthe, K.-T. Rie, J.W. Schultze, S. Simson, Structure and properties of plasma-nitrided stainless steel, *Surf. Coat. Technol.* 412, 74-75, (1995)
- [27] S. Mändl, R. Günzel, E. Richter, W. Möller, Nitriding of austenitic stainless steels using plasma immersion ion implantation, *Surf. Coat. Technol.* 372, 100-101, (1998)
- [28] S. Mändl, R. Günzel, E. Richter, W. Möller, B. Rauschenbach, Annealing behavior of nitrogen implanted stainless steel, *Surf. Coat. Technol.* 423, 128-129, (2000)
- [29] T. Bacci, F. Borgioli, E. Galvanetto, G. Pradelli, Glow-discharge nitriding of sintered stainless steels, *Surf. Coat. Technol.* 139, 251, (2001)
- [30] V. Singh, K. Marchev, C.V. Cooper, E.I. Meletis, Intensified plasma-assisted nitriding of AISI 316L stainless steel, *Surf. Coat. Technol.* 160, 249, (2002)

- [31] S. Grigull, S. Parascandola, Ion-nitriding induced plastic deformation in austenitic stainless steel, *J. Appl. Phys.* 88, 6925, (2000)
- [32] E. Richter, R. Günzel, S. Parascandola, T. Telbizova, O. Kruse, W. Möller, Nitriding of stainless steel and aluminum alloys by plasma immersion ion implantation, *Surf. Coat. Technol.* 128, 21, (2000)
- [33] G.A. Collins, R. Hutchings, J. Tendys, Plasma immersion ion implantation of steels, *Materials Science and Engineering: A* 139, 171-178, (1991)
- [34] M. Samandi, et al., Microstructure, corrosion and tribological behaviour of plasma immersion ion-implanted austenitic stainless steel, *Surface and Coatings Technology* 59(1), 261-266, (1993)
- [35] G. Wagner, et al., Phase analysis of a nitrogen implanted CrNi 18.9 steel: A cems-study, *Hyperfine Interactions* 46(1-4), 501-508, (1989)
- [36] D.L. Williamson, J.A. Davis, P.J. Wilbur, Effect of austenitic stainless steel composition on low-energy, high-flux, nitrogen ion beam processing, *Surface and Coatings Technology* 103, 178-184, (1998)
- [37] C.R. Brooks, *Principles of the surface treatment of steels*, Technomic Publishing Company, Inc. Pennsylvania, USA, (1992)
- [38] S.R. Kappaganthu, Y. Sun, Formation of an MN-type cubic nitride phase in reactively sputtered stainless steel-nitrogen films, *J. Cryst. Growth* 267, 385, (2004)
- [39] Z.L. Zhang, T. Bell, Structure and corrosion resistance of plasma nitrided stainless steel, *Surface Engineering* 1(2), 131-136, (1985)

- [40] K. Ichii, K. Fujimura and T. Takase: Technology Reports of Kansai University, 1986, vol. 27, pp. 135-144.
- [41] A. Billard, et al., Corrosion-resistant and hard 310 stainless steel-carbon coatings prepared by reactive dc magnetron sputtering, *Surface and Coatings Technology* 43, 521-532, (1990)
- [42] A. Saker, C.H Leroy, H. Michel, C. Frantz, Properties of sputtered stainless-steel coatings and structural analogy with low temperature plasma nitride layers of austenitic steels, *Mat. Sci. Eng. A140*, 702, (1991)
- [43] S.R. Kappaganthu, Y. Sun, Influence of sputter deposition conditions on phase evolution in nitrogen-doped stainless steel films, *Surf. Coat. Tech.* 198, 59, (2005)
- [44] J. Baranowska, S. Fryska, T. Suszko, The influence of temperature and nitrogen pressure on S-phase coatings deposited by reactive magnetron sputtering, *Vacuum* 90, 160, (2013)
- [45] S. Cusenza, D. Jürgens, M. Uhrmacher, P. Schaaf, Nitrided amorphous stainless steel coatings deposited by reactive magnetron sputtering from an austenitic stainless steel target, *Adv. Eng. Materials* 11, 17, (2009)
- [46] S.R. Kappaganthu, Y. Sun, Influence of sputter deposition conditions on phase evolution in nitrogen-doped stainless steel films, *Surf. Coat. Technol.* 198 (2005) 59.
- [47] Y. Sun, T. Bell, G. Wood, Wear behavior of plasma-nitrided martensitic stainless steel, *Wear* 178(1), 131-138, (1994)
- [48] M.K. Lei, Z.L. Zhang, X. M. Zhu, Effects of nitrogen-induced hcp martensite formation on corrosion resistance of plasma source ion nitrided austenitic stainless steel, *Journal of Materials Science Letters* 18(18), 1537-1538, (1999)

- [49] M.P. Fewell and J.M. Priest, "Higher-order diffractometry of expanded austenite using synchrotron radiation," *Surf. Coat. Tech.* 202, 1802, 2008.
- [50] K. Marchev, R. Hidalgo, M. Landis, R. Vallerio, C.V. Cooper, B.C. Giessen, The metastable m phase layer on ion-nitrided austenitic stainless steels, Part 2: crystal structure and observation of its two-directional orientation anisotropy, *Surf. Coat. Technol.* 112, 67, (1999)
- [51] T.S. Hummelshøj, T.L. Christiansen, M.A.J. Somers, Lattice expansion of carbon-stabilized expanded austenite, *Scripta Materialia* 63(7), 761-763, (2010)
- [52] K. Marchev, M. Landis, R. Vallerio, C.V. Cooper, B.C. Giessen, The m phase layer on ion-nitrided austenitic stainless steels III: An epitaxial relationship between the m phase and the  $\gamma$  parent phase and a review of structural identification of this phase, *Surf. Coat. Technol.* 184, 116-119, (1999)
- [53] T. Christiansen, M.A.J. Somers, Characterization of low temperature surface hardened stainless steel, *E-structure* 9, 1-17, (2006)
- [54] B.A. Shedden, F.N. Kaul, M. Samandi and B. Window, The role of energetic neutrals in reactive magnetron sputtering of nitrogen-doped austenitic stainless steel coatings, *Surface and Coatings Technology* 97(1), 102-108, (1997)
- [55] T.L. Christiansen, M.A.J. Somers. Low-temperature gaseous surface hardening of stainless steel: The current status, *International Journal of Materials Research* 100(10), 1361-1377, (2009)

- [56] C.N.J. Wagner, J.P. Boisseau, E.N. Aqua, X-ray diffraction study of plastically deformed copper, Transactions of the Metallurgical Society of AIME 233(7), 1280, (1965)
- [57] M.S. Paterson, X-ray diffraction by face-centered cubic crystals with deformation faults, Journal of Applied Physics 23(8), 805-811, (1952)
- [58] B.E. Warren, X-ray studies of deformed metals, Progress in Metal Physics 8, 147-202, (1959)
- [59] Y. Sun, X.Y. Li, T. Bell, X-ray diffraction characterization of low temperature plasma nitrided austenitic stainless steels, Journal of Materials Science 34(19), 4793-4802, (1999)
- [60] C. Blawert, H. Kalvelage, B.L. Mordike, G.A. Collings, K.T. Short, Y. Jirásková, O. Schneeweiss, Nitrogen and carbon expanded austenite produced by PI 3, Surf. Coat. Technol. 136, 181-187, (2001).
- [61] T. Christiansen and M.A.J. Somers, On the crystallographic structure of S-phase, Scripta Met. 50, pp. 35-37, (2004).
- [62] X.L. Xu, L.Wang, Z.W. Yu and Z.K. Hei, Microstructural characterization of plasma nitrided austenitic stainless steel, Surf. Coat. Technol. 132, pp. 270-274, (2000).
- [63] D. Stroz, M. Psoda, TEM studies of plasma-nitrided stainless steel, J. Microscopy 237, 227, (2010)
- [64] D.L. Williamson, et al., Metastable phase formation and enhanced diffusion in fcc alloys under high dose, high flux nitrogen implantation at high and low ion energies, Surface and Coatings Technology 65(1-3), 15-23, (1994)

- [65] S. Sienz, S. Mändl, B. Rauschenbach, In situ stress measurements during low-energy nitriding of stainless steel, *Surface and Coatings Technology* 156(1), 185-189, (2002)
- [66] S. Parascandola, W. Möller, D.L. Williamson, The nitrogen transport in austenitic stainless steel at moderate temperatures, *Applied Physics Letters* 76(16), 2194-2196, (2000)
- [67] W. Möller, et al., Surface processes and diffusion mechanisms of ion nitriding of stainless steel and aluminium, *Surface and Coatings Technology* 136(1), 73-79, (2001)
- [68] X.Y. Li, et al., Thermal stability of carbon S phase in 316 stainless steel, *Surface Engineering* 18(6), 448-451, (2002)
- [69] L. Wang, Y. Li, Y.Z. Wang, Thermal stability of nitrogen expanded austenite formed by plasma nitriding on AISI304 austenitic stainless steels, *Key Engineering Materials* 373, 308-311, (2008)
- [70] L. Nosei, et al., Stability under temperature of expanded austenite developed on stainless steel AISI 316L by ion nitriding, *Thin Solid Films* 468(1), 134-141, (2004)
- [71] G. Stachowiak, A.W. Batchelor, *Engineering tribology*, Butterworth-Heinemann, (2013)
- [72] H.P. Jost, Tribology—origin and future, *Wear* 136(1), 1-17, (1990)
- [73] I.M. Hutchings, P. Shipway, *Tribology: Friction and wear of engineering materials*, 156, (1992)
- [74] M.K. Lei, X.M. Zhu, Plasma-based low-energy ion implantation of austenitic stainless steel for improvement in wear and corrosion resistance, *Surface and Coatings Technology* 193(1), 22-28, (2005)

- [75] Y. Sun, T. Bell, Dry sliding wear resistance of low temperature plasma carburised austenitic stainless steel, *Wear* 253(5), 689-693, (2002)
- [76] K. L. Hsu, T.M. Ahn, D.A. Rigney, Friction, wear and microstructure of unlubricated austenitic stainless steels, *Wear* 60(1), 13-37, (1980)
- [77] A.F. Smith, The friction and sliding wear of unlubricated 316 stainless steel in air at room temperature in the load range 0.5-90N, *Wear* 110, 151-168, (1986)
- [78] A.F. Smith, The friction and sliding wear of unlubricated 316 stainless steel at room temperature in air, *Wear* 96(3), 301-318, (1984)
- [79] T. Bell, Surface engineering: A rapidly developing discipline, *European Journal of Engineering Education* 12(1), 27-32, (1987)
- [80] M. Ohring, *Materials science of thin films*, Academic Press, (2001)
- [82] P.M. Martin, *Handbook of deposition technologies for films and coatings: Science, applications and technology*, William Andrew, (2009)
- [83] B. Window, N. Savvides, Charged particle fluxes from planar magnetron sputtering sources, *Journal of Vacuum Science & Technology A* 4(2), 196-202, (1986)
- [84] D.W. Hoffman, J.A. Thornton, Internal stresses in Cr, Mo, Ta, and Pt films deposited by sputtering from a planar magnetron source, *Journal of Vacuum Science & Technology* 20(3), 355-358, (1982)
- [85] V. Stambouli, et al., Argon incorporation effects on the conductivity of metal layers, *Thin Solid Films* 193, 181-188, (1990)

[86] D.M. Mattox, V.H. Mattox, Vacuum coating technology, William Andrew Publishing, New York, (2003)

[87] A, Kelly, K. Anthony. Crystallography and crystal defects. John Wiley & Sons, (2000).

Kelly, A., & Knowles, K. M. (2012). Crystallography and crystal defects. John Wiley & Sons.

[88] [https://en.wikipedia.org/wiki/Bragg%27s\\_law#/media/File:BraggPlaneDiffraction.svg](https://en.wikipedia.org/wiki/Bragg%27s_law#/media/File:BraggPlaneDiffraction.svg)

[89] R. Resnick, D. Halliday, J. Walker, Fundamentals of physics. Vol. 1. John Wiley, (1988).

[90] D. Briggs, David, M. P. Seah. Practical surface analysis by Auger and X-ray photoelectron spectroscopy, John Wiley & Sons, (1983)

[91] D. Briggs, M. P. Seah, Practical surface analysis. Vol. 1, Auger and X-ray photoelectron spectroscopy, 2. ed. Frankfurt am Main: Wiley, (1990)

[92] J. Goldstain, et al, Scanning electron microscopy and X- ray microanalysis, Springer, (2017).

[93] <http://urus-28.deviantart.com/journal/Electronic-Microscopy-462654632>

[94] D. Williams, B. David, C. Barry, The transmission electron microscope In Transmission electron microscopy, Springer US 3-17. (1996)

[95] D.B. Williams, C.B. Carter, Transmission Electron Microscopy: A Textbook for Materials Science, Plenum Press, New York, (1996).

[96] B. Bhushan. Introduction to tribology. John Wiley & Sons, (2013).

[97] <https://www.slideshare.net/WaqasAbid7/difference-between-rockwell-brinell-vickers-and-knoop-hardness-test>

[98] D. Nix. "Mechanical properties of thin films." Metallurgical and Materials Transactions A 20.11 (1989): 2217-2245, (1989).

- [99] W. Oliver, G. Pharr. "An improved technique for determining hardness and elastic modulus using load and displacement sensing indentation experiments." *Journal of materials research* 7.6 1564-1583, (1992).
- [100] Y. Nakamura, J. Muto, H. Nagahama, I. Shimizu, T. Miura, I. Arakawa "Amorphization of quartz by friction: Implication to silica-gel lubrication of fault surfaces. *Geophysical Research Letters* 39.21 (2012).
- [101] F.I. Alresheedi, and J. E. Krzanowski. "Structure and morphology of stainless steel coatings sputter-deposited in a nitrogen/argon atmosphere." *Surf. Coat. Technol.*, 314 05-112. 2017.
- [102] A. Wang., et al. Structural and elastic properties of cubic and hexagonal TiN and AlN from first-principles calculations. *Computational Materials Science* 48.3 705-709., (2010)
- [103] M.P. Fewell, et al., The nature of expanded austenite, *Surface and Coatings Technology*, 131(1), 300-306, (2000)
- [104] P. Hones, R. Sanjines, F. Levy, Characterization of sputter-deposited chromium nitride thin films for hard coatings, In *Surface and Coatings Technology*. 94–95, 398-402, (1997).
- [105] L. Cunha, M. Andritschky, K. Pischow, Z. Wang, Microstructure of CrN coatings produced by PVD techniques, *Thin Solid Films*, Volumes 355–356, 465-471, (1999).
- [106] W. Ernst, J. Neidhardt, H. Willmann, B. Sartory, P.H. Mayrhofer, C. Mitterer, Thermal decomposition routes of CrN hard coatings synthesized by reactive arc evaporation and magnetron sputtering, In *Thin Solid Films*, Volume 517, Issue 2, Pages 568-574. (2008).
- [107] A. Tayal, M. Gupta, A. Gupta, V. Ganesan, L. Behera, S. Singh, S. Basu, Study of magnetic iron nitride thin films deposited by high power impulse magnetron sputtering, *Surf. Coat. Tech*, 275 264-269, (2015).

- [108] W.H. Zhong, B.K. Tay, S.P. Lau, X.W. Sun, S. Li, C.Q. Sun, Structural and magnetic properties of iron-nitride thin films deposited using a filtered cathodic vacuum arc, *Thin Solid Films*. 478, 61– 66, (2005).
- [109] Mukul Gupta, Ajay Gupta, P. Bhattacharya, P. Misra, L.M. Kukreja, Study of iron nitride thin films deposited by pulsed laser deposition, *Alloys and Compounds*. 326, 265–269, (2001).
- [110] G.J.W.R. Dorman, M. Sikkens, Structure of reactively sputtered nickel nitride films, *Thin Solid Films*. 105, Issue 3, Pages 251-258, (1983).
- [111] N. Popović, Ž. Bogdanov, B. Gončić, S. Štrbac, Z. Rakočević, Reactively sputtered Ni, Ni(N) and Ni<sub>3</sub>N films: Structural, electrical and magnetic properties, *Applied Surface Science*. 255, 7, 4027-4032, (2009).
- [112] J. Hay, Introduction to Instrumented Indentation Testing, *Experimental Techniques*. 33, 66-72, (2009).
- [113] L.E. Toth, *Transition Metal Carbides and Nitrides*. Academic Press, New York. 6-7, (1971).
- [114] I. Petrov, P. B. Barna, L. Hultman, and J. E. Greene, Microstructural evolution during film growth. *J. Vac. Sci. Technol. A* 21(5), pp. S117-S128, (2003).
- [115] G. Abrasonis, J.P. Riviere, C. Templier, A. Declémy, L. Pranevicius and X. Milhet, "Ion beam nitriding of single and polycrystalline austenitic stainless steel, *J. Appl. Phys.* 97, 083531, (2005).
- [116] J. Oddershede, T.L. Christiansen, K. Stahl, and M.A.J. Somers, "Extended X-ray absorption fine structure investigation of nitrogen stabilized expanded austenite, *Scripta. Mater.* 62, pp. 290-293, (2010).